Characterising the Gulf of Mexico Yield Surface at High Stress

MEng in Engineering Science, University of Oxford. 2018

A dissertation submitted by

Liam Eagle

in partial fulfilment of the requirements for the degree of

M.S. in Civil and Environmental Engineering

in

School of Engineering

Tufts University August 2021

Adviser: Professor J. T. Germaine

I. Abstract

Gaining insights into fundamental soil behaviour through testing with state-of-the-art equipment is a vital step before more advanced constitutive soil and geomechanical models can advance further. One key input into constitutive models is a mathematical expression for the materials yield surface; a conceptual surface that separates elastic from plastic behaviour. This experimental study is based on high stress triaxial testing of a resedimented Gulf of Mexico mudrock. This thesis studies the location of the yield surface for this material as well as its stress strain behaviour in both triaxial compression and extension. Multiple studies have investigated the yield surface for sediments from this region at lower stresses and in compression, but there is limited research at higher stresses and in different shear modes, something which is of importance when modelling unconventional geologic phenomena such as accretionary prisms or salt diapirs (Nikolinakou et al. 2014).

Samples were normally consolidated to 40 MPa, along hydrostatic, drained and K_0 stress paths, before being undrained sheared. The undrained stress paths from these tests were used as a proxy for the shape of the material yield surface. Finally, triaxial test data was compared to constitutive soil models that were run on a 2D triaxial specimen model using a finite element programme.

Results showed significant pore pressure generation in triaxial extension, and continued shear induced pore pressure generation when stress paths moved inside the yield surface. Comparisons are also made with tests from previous studies at lower stresses and provide further evidence against the conventional assumption of constant normalised soil properties.

II. Acknowledgements

I would like to express my gratitude towards my supervisor Dr. Germaine for imparting a great deal of knowledge and his unwavering patience over the course of my master’s degree.

Thanks also goes to Dr. Plumb and Prof. Dorfmann for their help and expertise.

Gratitude is also extended to Ward and Burke Construction for generously sponsoring my degree.

III. Contents

IV. List of Tables

V. List of Figures

Key Words

Clay, Anisotropy, Triaxial Test, Undrained Shear, Yield Surface, Constitutive Models

Terminology

ADC	Analogue to Digital Converter
AMS	Aerospace Materials Specifications
CCW	Counter Clockwise
CDAS	Central Data Acquisition System
CRS	Constant Rate of Strain
CW	Clockwise
DOS	Disk Operating System
DSS	Direct Simple Shear
FEA	Finite Element Analysis
GeoFluids	Consortium of universities looking to solve problems in
IDE	Integrated Development Environment
ISA	Industry Standard Architecture
KSC	Kilogram per square centimeter
LL	Liquid Limit
LVDT	Linear Variable Differential Transducer
MCC	Modified Cam Clay
OC	Overconsolidated
OCR	Over Consolidation Ratio
PI	Plasticity Index
PID	Proportional–Integral–Derivative
PL	Plastic Limit
RBBC	Resedimented Boston Blue Clay
RGOM-EI	Resedimented Gulf of Mexico Eugene Island
SHANSEP	Stress History and Normalised Engineering Parameters
TC	Triaxial Compression
TE	Triaxial Extension
UC	Undrained Compression
UE	Undrained Extension
USB	Universal Serial Bus
VCL	Virgin Compression Line

Symbols

A_0	Initial specimen area
K	Lateral stress ratio
K_0	Coefficient of lateral earth pressure at rest
K_{0NC}	Coefficient of lateral earth pressure at rest for a NC soil
e	Void ratio
e_0	Initial void ratio
σ_c	Cell pressure

φ'_{CS}	Critical state friction angle
S_u	Undrained shear strength
E_u	Undrained secant Young's modulus
σ_v, σ'_v	Vertical total stress, vertical effective stress
σ_h, σ'_h	Horizontal total stress, horizontal effective stress
σ'_{vc}	Vertical consolidation effective stress
$\sigma'_{v,max}$	Maximum past vertical consolidation effective stress
$\sigma_1, \sigma_2, \sigma_3$	Principal stresses
σ_{oct}	Octahedral stress, $1/3(\sigma_1 + 2\sigma_3)$
u	Pore pressure
u_b	Backpressure
u_e	Excess pore pressure
u_s	Shear induced pore pressure
u_c	Pore pressure at the centre of sample
m_v	Coefficient of volume compressibility
n	Porosity
ε_a	Axial strain
ε_f	Strain at peak shear stress
ν	Poisson's ratio
ω	Water content $(\frac{W_w}{W_s})$
φ, φ'	Friction angle, effective friction angle
φ_{cs}	Critical state friction angle

1 Introduction

1.1 Problem Statement

The yield surface of a cohesive material is a fundamental input into all soil constitutive soil models. These same models are then applied in finite element programmes and geomechanical models to predict various engineering values of interest such as strain and pore pressure. The behaviour of the material is driven by where the yield surface lies in relation to the current stress state. Hence an accurate picture of the yield surface is an essential part of understanding and predicting soil behaviour.

Interest in the behaviour of fine-grained soils at high effective stresses stems from the petroleum industry and the extraction of hydrocarbons from shallow reservoirs in unlithified or weakly lithified mudrocks. There is very limited triaxial strength data for resedimented materials consolidated to high stresses (> 40 MPa). In addition, there is limited data for modes of shearing other than triaxial compression in materials consolidated to high stresses. This presents a problem as large stress ranges and different modes of shearing are often encountered in geologic phenomena such as salt diapirs or accretionary prisms. Therefore, understanding the behaviour of mudrocks in these settings is important to accurately predicting in situ stresses and pore pressures; something which could ultimately improve wellbore drilling and a general understanding of complex geologic processes.

1.2 Thesis Objectives

Work in this thesis centres around using undrained shearing to explore the shape of the yield surface for normally consolidated Gulf of Mexico mudrock at high consolidation stresses. Samples are consolidated both isotropically and in K_0 conditions. Shearing is then performed both in triaxial compression and extension so that the impacts of different shearing modes on soil behaviour can be assessed. By using undrained shearing, the yield surface can be mapped efficiently with the need for just two triaxial tests. The results of this work should help to improve our understanding of how stress level and consolidation history impacts the shape of the yield surface.

A secondary objective of this thesis is to compare results of experimental work for this thesis with predictions from constitutive soil models to assess their performance, or if different formulations for the yield surface shape would be more appropriate. A simple axisymmetric finite element model of a standard triaxial specimen was produced using Plaxis 2D-2020™ software. Modified Cam Clay (MCC) and MIT-E3 constitutive soil models were then run through this model.

Research efforts within this thesis form part of a larger joint research effort from the UT GeoFluids Consortium ("UT GeoFluids" n.d.). This research group sees Geoscientists from the University of Texas at Austin and Engineers at Tufts University collaborate to "*to study the state and evolution of pressure, stress, deformation and fluid migration through experiments, theoretical analysis, and field study"*. At the time of writing, GeoFluids has entered its second decade of research and continues to be supported by more than 10 major energy companies.

1.3 Organisation of Thesis

This thesis is presented in 8 chapters. Chapter two begins this thesis by detailing a review of the research that has occurred to date which is relevant to the work presented afterwards.

In chapter 3 a detailed explanation of the resedimentation procedure, used within the Tufts laboratory to create test specimens, is given. Further information is then given on specific details about the Resedimented Gulf of Mexico Eugene Island (RGoM-EI) material, which was the sole test material used for this work.

Chapter 4 looks at the state-of-the-art equipment that has been used within this research to perform tests on resedimented soil specimens. Information is also presented regarding the data acquisition system, triaxial control software and sundry other equipment that is essential for successfully performing triaxial tests.

Chapter 5 details the specific testing procedures that were implemented and developed for the triaxial tests.

A presentation of the experimental outputs from this body of work is given in chapter 6. The strength and behaviour of the RGoM-EI material is evaluated in both triaxial compression and extension, and the effects of consolidation history are also assessed.

In chapter 7 experimental results are compared with constitutive soil models that have been tuned to predict the behaviour of this test material. The chapter also provides some background on the mechanics behind these models, especially in relation to their yield surfaces.

The final chapter contains conclusions that are drawn from the results of triaxial testing on RGoM-EI. Additionally, the chapter includes a discussion of suggested future work and improvements to the testing protocols.

2 Background

2.1 Introduction

This chapter begins by reviewing previous studies that have been conducted to look generally at the mechanical behaviour of fine-grained sediments, particularly at stresses below 10 MPa.

A presentation of research that justifies some key assumptions of this work is also given, such as the use of resedimented specimens, choice of pore fluid salinity and the use of undrained shearing to determine the location of the yield surface.

2.2 Previous Studies of Strength Behaviour of Fine-Grained Sediments

B. Casey (2014) undertook an extensive study into the consolidation and shear strength behaviour of fine-grained sediments. Testing was performed on eight different K_0 consolidated resedimented samples over four orders of stress magnitude. Insights from the research included confirmation that many fine-grained materials had stress dependent strength properties, especially when evaluated over large stress ranges. This stress dependence was found to be reliant upon the soil's composition, with high plasticity clays (including the test material used in this research) showing higher levels of stress dependence. Normalised strength properties reduced more quickly with high plasticity soils when compared to low plasticity. His research also found that permeability-porosity relationships could be correlated with liquid limit. This built upon a study by Abdulhadi (2009), who looked solely at K_0 consolidated samples of Resedimented Boston Blue Clay (RBBC) at stress levels of between 0.15 to 10 MPa. He found that both triaxial compression and extension data show reductions in the undrained strength ratio (S_u/σ'_{vc})[1], stiffness ratio (E_u/σ'_{vc}), strain to mobilize peak resistance (ε_f) and critical state friction angle (φ'_{cs}) with increasing stress level.

Petley (1999) studied the undrained shear behaviour of a range of mudrocks originating from the UK. Higher stresses were used in this work with consolidation stresses of between 2-50 MPa. Petley proposed that all mudrocks behave in a brittle manner at low mean effective stresses and in a ductile fashion at high mean effective stresses whilst maintaining peak strength even at large strains. In between these two responses was found to be a ‘transitional regime’, where shear deformation produces an initially ductile response before strain weakening to a residual strength. Further work by Nygård et al. (2006) found that this transitional regime in mudrocks could be correlated to the overconsolidation ratio.

Some more recent research on undrained shear behaviour has included work by Cai et al. (2018), where the effects of anisotropic consolidation stress paths on resedimented Wenzhou clay was investigated.

2.3 Effects of Salinity on Mechanical Behaviour

Fahy (2014) undertook a systematic study into the effect of pore fluid salinity on the mechanical behaviour of six different high plasticity soils, including the GoM-EI material used in this study. Samples with salinities ranging from distilled water to 256 g/L were tested in both triaxial and CRS devices. A key finding of this work was that increasing consolidation stresses of resedimented specimens to 40 MPa decreased the influence of salinity on compressibility to negligible levels. At a consolidation stress of 0.4 MPa, the material did exhibit significant sensitivity to increasing salinity with both shear strength and critical state friction angles also increasing.

---

[1] Strength properties are normalised in this work by the vertical effective stress σ'_{vc} as recommended by Ladd (1964).

2.4 Resedimented Behaviour

Resedimented specimens are used in this work as an analogue for in situ samples for a wide range of reasons that are discussed in detail in chapter 0. Previous work comparing intact vs resedimented behaviour has consistently shown resedimented specimens to be a reasonable substitute for intact samples. Betts (2014) has looked at intact vs resedimented behaviour for Eugene Island Clay, which was the test material used within this body of work. Permeability and compressibility behaviour was compared through the use of CRS (constant rate of strain) tests on resedimented and intact core specimens with results suggesting that resedimentation is able to replicate the fabric seen in natural deposits.

2.5 Yield Surfaces

A yield surface is a conceptual surface that separates elastic from elastoplastic behaviour in a material. Originally proposed for use in modelling metal plasticity, yield surfaces have been adapted for use in modelling the behaviour of cohesive materials. The applicability of yield surfaces in modelling metals is well established and can be explained with micromechanical models; this is something which is far less clear for cohesive materials (Whittle 1987).

The surface itself represents a locus of stress states which if reached, initiate yielding in the material. This locus of stress states can be represented mathematically by a scalar yield function $f(\sigma_{ij})$, where σ_{ij} is the Cauchy stress tensor. The implications of the value of this function are as follows:

1. $f(\sigma_{ij}) < 0$: Elastic behaviour within the material.
2. $f(\sigma_{ij}) = 0$: Elastoplastic behaviour, yielding initiated.
3. $f(\sigma_{ij}) > 0$: Stress state not permissible.

Values of $f(\sigma_{ij}) > 0$ are not permissible, as when yielding is reached in the material, deformations occur at constant stress. A yield surface can then be implemented within a constitutive soil model which allows for a mathematical representation of soil behaviour in response to external loading.

Ultimately, the outputs of research into fundamental soil behaviour feed into tuning and developing constitutive soil models. These soil models are then implemented within large geomechanical models or finite element packages such as Plaxis, a software package that was used within this body of work to simulate triaxial tests. The results of triaxial test simulations can be seen in Chapter 0.

2.6 Undrained Stress Paths as a Proxy for Yield Surfaces

Previous work investigating yield surfaces of natural clays has shown that the upper and lower portions of the yield surface correspond approximately to the undrained compression and extension shear strengths respectively in p-q space (Graham et al. 1983). Work by Hanley (2017) has also shown that undrained testing to define the yield surface of fine-grained sediments can be used as a way of more quickly gaining a first order approximation of the yield surface. In his testing regimen, 19 drained triaxial tests were performed on RGoM-EI material that were first K_0 consolidated to 1 MPa before being unloaded to an OCR of 2. The act of unloading the material from normally consolidated conditions brings the stress state of the specimen to be inside its yield surface. After unloading, the specimen is finally drained sheared along stress paths of varying angles in order to probe the yield surface. These 19 drained tests are shown in Figure 2-1, with an example loading sequence for one of these tests shown in Figure 2-3. A larger amount of volumetric strain is associated with the material after yielding has been reached, therefore the strain energy method can be used to interpret a yield point. The primary advantage of this method, is that it can identify yield in a manner that is independent of the stress path direction. Additionally, the strain energy method employs constructions to define the yield point that occur on arithmetic scales and hence are prone to much smaller errors than may be seen in log space. This technique is shown for one such drained test in Figure 2-4. After interpreting yield points for a sequence of tests conducted along differing stress paths, they can be plotted in p-q stress space and a yield surface drawn through the yield points. This method for experimentally locating the yield surface of a clay has been successfully used in the practice for many decades (Graham et al. 1983; Tavenas 1977). Though effective, this method for determining the location of the yield surface is very labour intensive; the 19 drained tests presented here were completed over the course of two years. In contrast, the result of one undrained compression test is shown in Figure 2-2 alongside the interpreted yield surface. It can be seen that this successfully traces the yield surface that was interpreted from the drained tests. Hence with one test in triaxial compression and one in extension, the effective stress paths can be combined with the Mohr-Coulomb failure envelope to capture the yield surface to a first order in p’-q stress space. As well as being quicker to run, this also represents a significant reduction in the total number of tests required. By testing more quickly, one is able to more easily investigate the impacts of a host of other factors that may impact the shape of the yield surface, such as stress level and consolidation history.

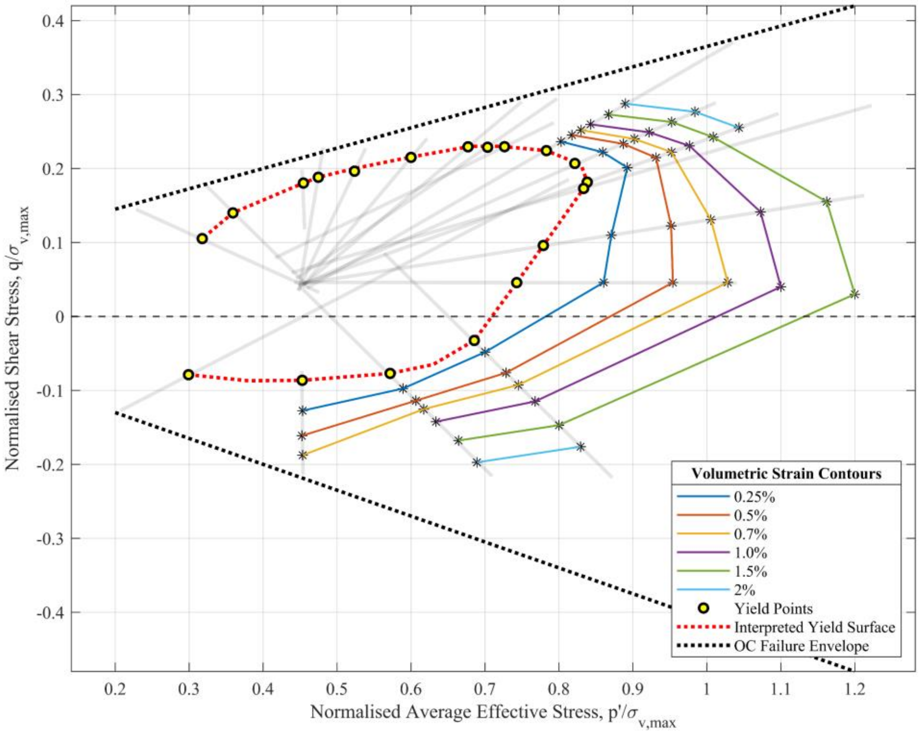

Figure 2-1 - Interpreted yield surface for RGoM-EI material at 1 MPa consolidation stress. Volumetric strain contours are also shown. Figure has been reproduced using data from Hanley (2017).

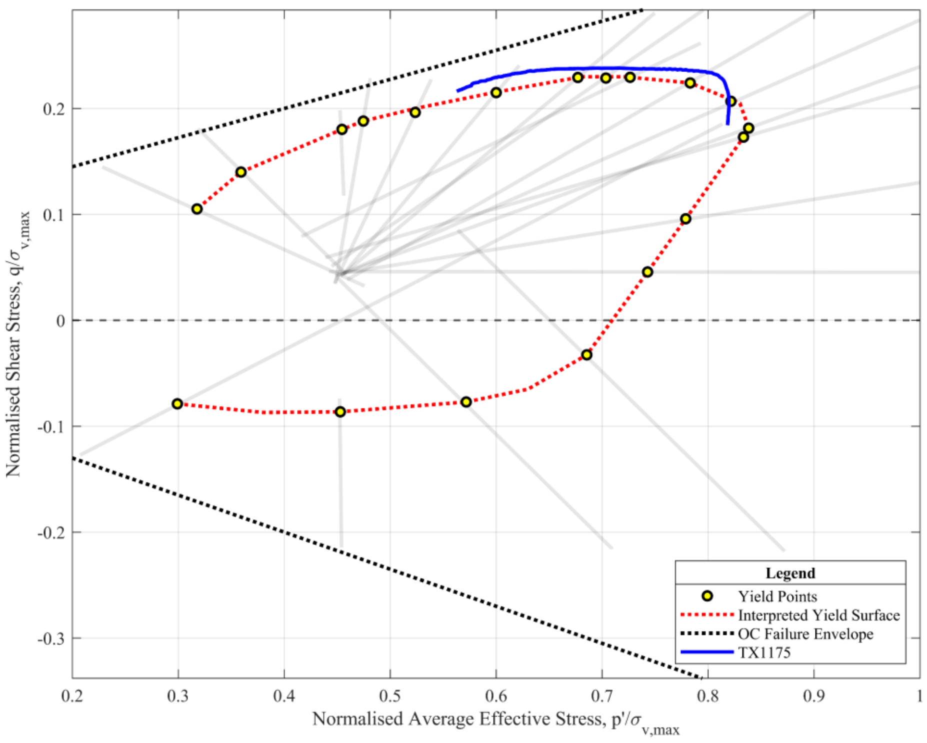

Figure 2-2 - The stress path for a normally consolidated undrained triaxial compression test is shown in relation to the interpreted yield surface. Figure has been reproduced using data from Hanley (2017).

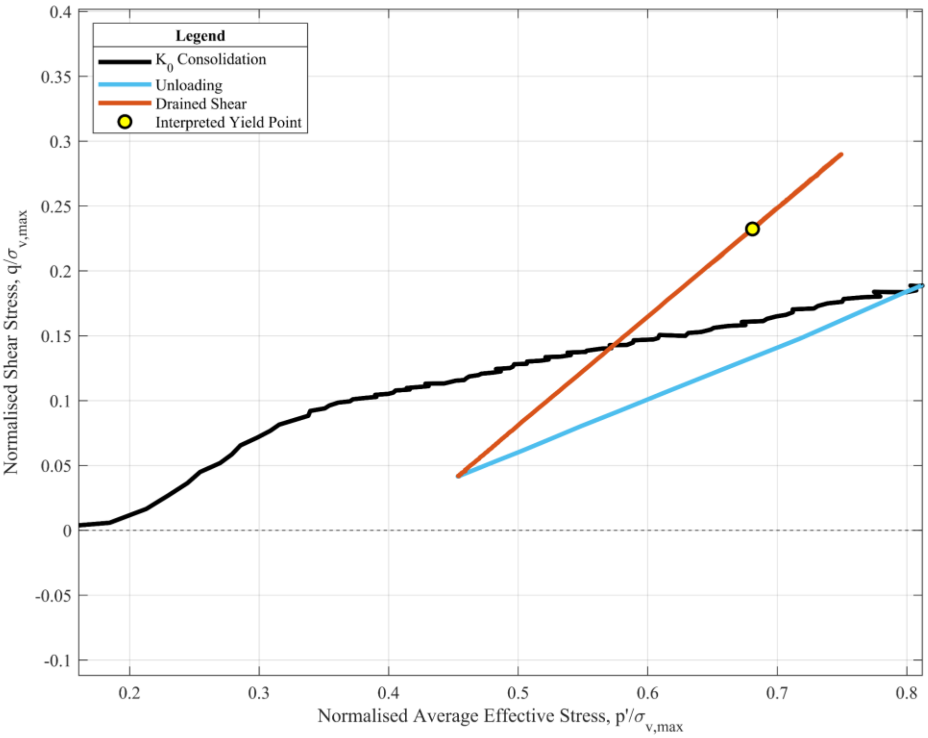

Figure 2-3 - Example stress paths from one of Hanley's tests. Samples are K0 consolidated to 1 MPa, before being unloaded to an OCR of 2. Finally, samples are drained sheared along stress paths of varying angles. Figure has been reproduced using data from Hanley (2017).

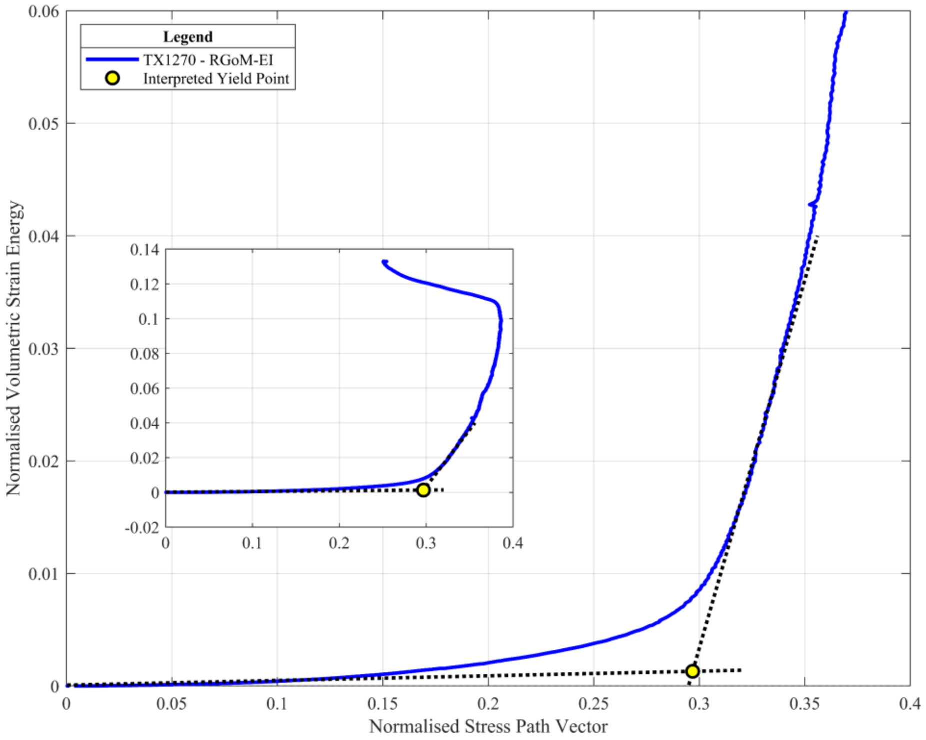

Figure 2-4 - Image showing normalised volumetric strain energy vs the normalised stress path vector far an individual test on RGoM-EI material at 1 MPa. Figure has been reproduced using data from Hanley (2017).

2.7 Strain Rate

Though studying the impacts of strain rate on undrained shear behaviour is outside the scope of this research, previous work has shown that undrained shearing results, particularly in the compression mode, are sensitive to strain rate. Since the undrained shear stress path is to be used as a proxy for the yield surface in this research, careful thought must therefore be given to the selection of strain rate. Work by Sheahan (1991) evaluated the impact of strain rates on undrained strength at 0.05, 0.5 and 50 %/hr. It was found that undrained strength increases with increasing strain rate, by about 8 % per log cycle change in strain rate. This effect becomes less pronounced with increasing OCR. Figure 2-6 is from a different study and plots the undrained shearing resistance vs log strain rate for several different lightly overconsolidated soils. The same trend of increasing shearing resistance with increasing shear rate is shown and occurs regardless of the mode of shearing. It is also noted that at increasing stress level, the larger pore pressures generated cause the effective stress path to deviate further from the total stress path, causing it to become more sensitive to strain rate (Figure 2-5).

Work by Graham et al. (1983) also investigated the impact of strain rate on undrained shearing resistance. Their results also found that lightly overconsolidated clays exhibit significant strain rate dependent stress strain characteristics, regardless of soil type or plasticity. These effects were present in triaxial compression and extension, causing a 10-20 % change in undrained shear strength for a tenfold change in strain rate. For undrained shear in this research, a strain rate of 0.5 %/hr was selected, a value that is standard within the Tufts laboratory.

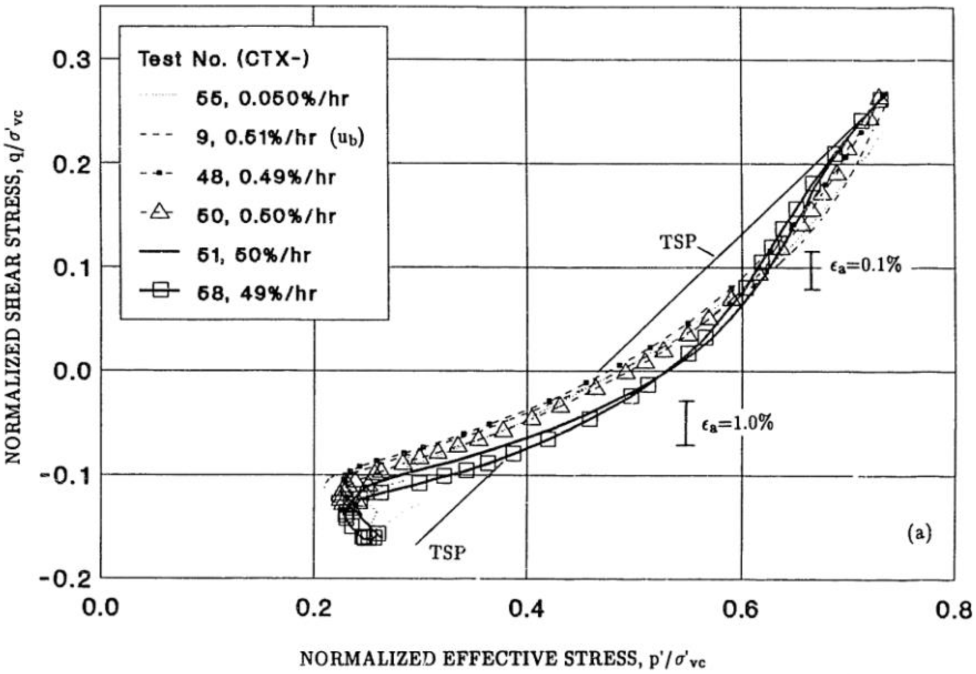

Figure 2-5 - Effect of strain rate on normalised stress paths of NC RBBC in undrained triaxial extension (Sheahan 1991).

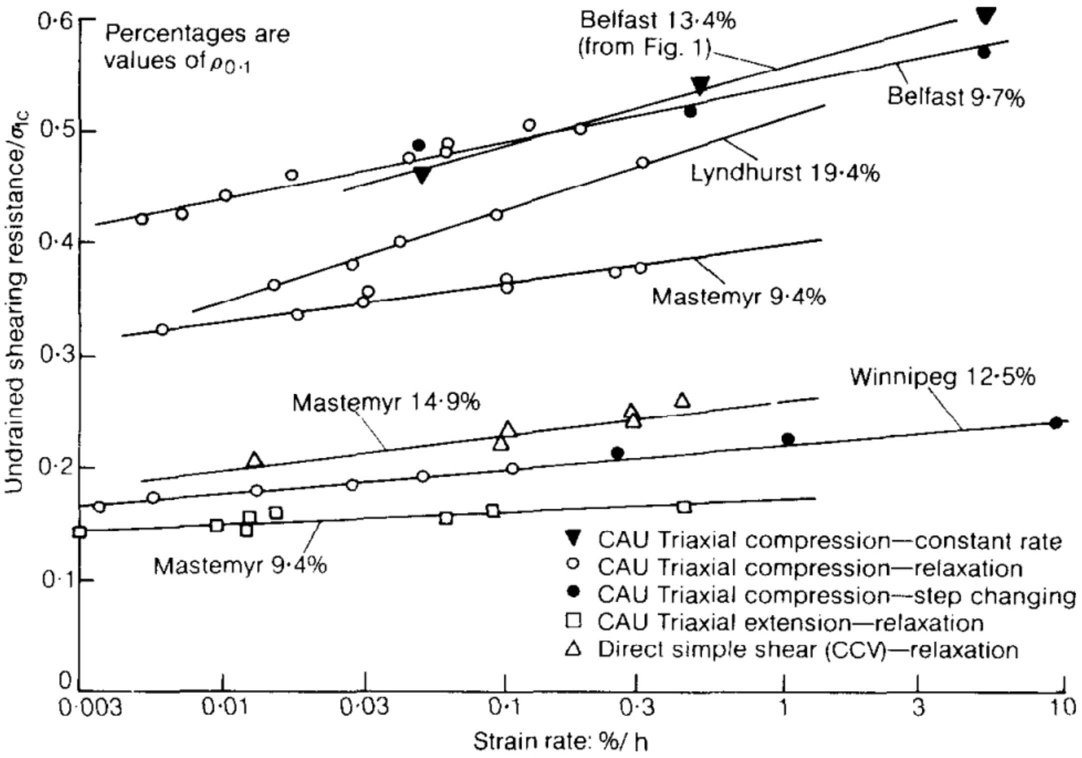

Figure 2-6 - Change in undrained shearing resistance vs log strain rate for different lightly consolidated soils (taken from (Graham et al. 1983).

2.8 Impact of Temperature on Shear Behaviour

Tanaka et al. (1997) investigated the stress-strain behaviour of reconstituted illitic clay at different temperatures over a range of 20 – 100°C. They found large strain behaviour to be independent of temperature, but peak shear strength to increase with increasing temperature due to smaller pore water pressure generation. Other studies include work by Gue et al. (2015) who looked at the behaviour of 15 deep water soft clays comparing in situ with laboratory temperatures. The tested materials had a range in I_p of 12 – 110 % and included both intact and resedimented samples. Results showed that testing at lower in situ temperatures led to on average a 24 % higher undrained shear strength and a 22 % higher preconsolidation pressure. The in situ temperatures in the aforementioned study were all lower than the laboratory temperature however. It is worth noting that the consolidation stresses used in this research would represent sediments that are several kilometres beneath the seabed, and as such the temperatures are likely much higher than at the surface. For testing at different temperatures, it was also noted that the impact of temperature on the stiffness of the membrane used can be significant, as polymeric latex materials exhibit non-linear temperature dependent mechanical properties.

2.9 Conclusion

The behaviour of many soils in TC is well understood, but a distinct lack of data in other modes of shearing makes predicting behaviour and drawing conclusions about trends in material behaviour prone to error. This distinct lack of data in TE for many clays including Gulf of Mexico sediments is something that is often highlighted in research publications. More data in TE will allow for more accurate modelling of complex geologic phenomena, such as accretionary prisms or salt diapirs, where the horizontal stress can become the major principal stress.

3 Resedimented Gulf of Mexico Eugene Island Clay

3.1 Introduction

The Gulf of Mexico, a region abundant in hydrocarbons. has grown to be responsible for 17 % of total U.S. crude oil production (US Energy Information Administration 2018). By 2017, 52 % of US oil production was from ultra-deep wells (Murawski et al. 2020). This push to extracting hydrocarbons from deeper water, necessitates an improved understanding of the material behaviour of the mudrocks surrounding these wells. Fundamental to predicting overpressures inside the wells, is a knowledge of the materials yield surface and how it responds to external factors such as increasing stress level.

The Eugene Island Block 330 is a 3x3 mile oil field located in the outer continental shelf of the Gulf of Mexico, offshore from the state of Lousiana. The geologic setting of this oil field is described in detail in various publications (Alexander and Flemings 1995; Anderson et al. 1991).

Clay material that has been used for creating resedimented samples in this work was originally obtained from two boreholes that were drilled in the 1990s. One borehole was located in Block 330 with another in Block 316 – these can be seen in Figure 3-1. The cores were obtained from depths ranging between 2200 to 2500 m, with sandy intervals removed during processing at the University of Texas. Processing also involved air-drying, mechanically grinding, sieving (material passed a #100 sieve) and blending the two cores of material. Further information pertaining to the geologic origin, processing and consolidation behaviour of RGoM-EI can be found in work by Betts (2014) and Casey (2014).

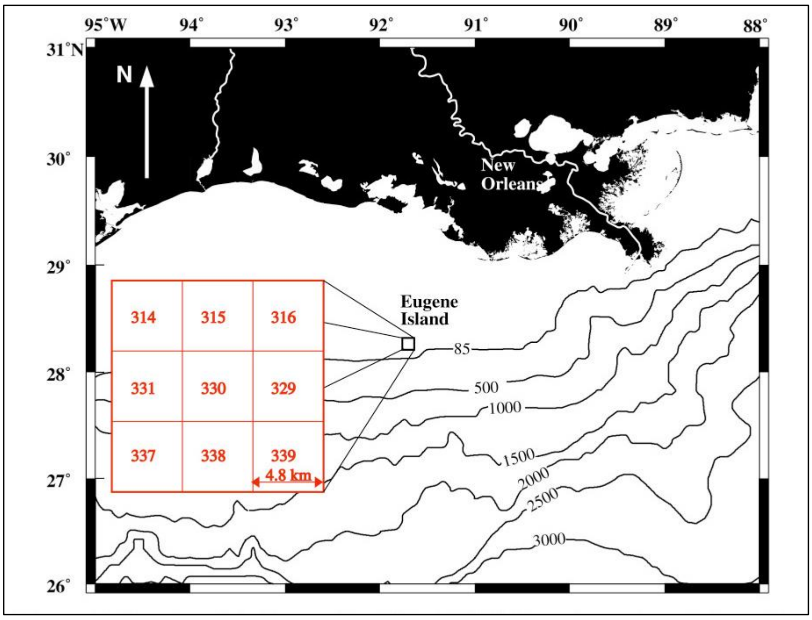

Figure 3-1- Location of the 3-mi.x3-mi. Eugene Island Block 330 field. Image extracted from (Guerin 2000).

3.2 RGoM-EI Material Properties

3.2.1 Atterberg limits

Atterberg limits are commonly used in the geotechnical engineering practice to aid in the classification of fine-grained soils. They define critical water contents, beyond which the state of the soil changes. The liquid limit, (LL), represents the water content where the soil begins to behave as a liquid rather than a plastic material. Conversely the plastic limit, (PL), is the water content where the soil begins to behave as a semi-solid rather than a plastic material (ASTM International 2017). These two limits can then be used to define a quantity known as the Plasticity Index (PI):

$$PI = LL - PL \tag{3-1}$$

The Plasticity Index is a measure of how strongly clay particles interact with water (Germaine and Germaine 2009), and the Atterberg limits can be correlated to various strength and consolidation parameters.

RGoM-EI has a liquid limit and plastic limit of 87 and 24 respectively (Betts 2014). This results in a high Plasticity Index of 63 and yields a material designation of CH or “Fat Clay”. This designation is based on the Unified Soil Classification System developed by A. Casagrande in the 1940s – this system is detailed in ASTM standard D2487 (ASTM International 2006). A Casagrande plasticity chart is shown in Figure 3-2, here Plasticity Index vs Liquid Limit is plotted for RGoM-EI along with other common testing materials for reference.

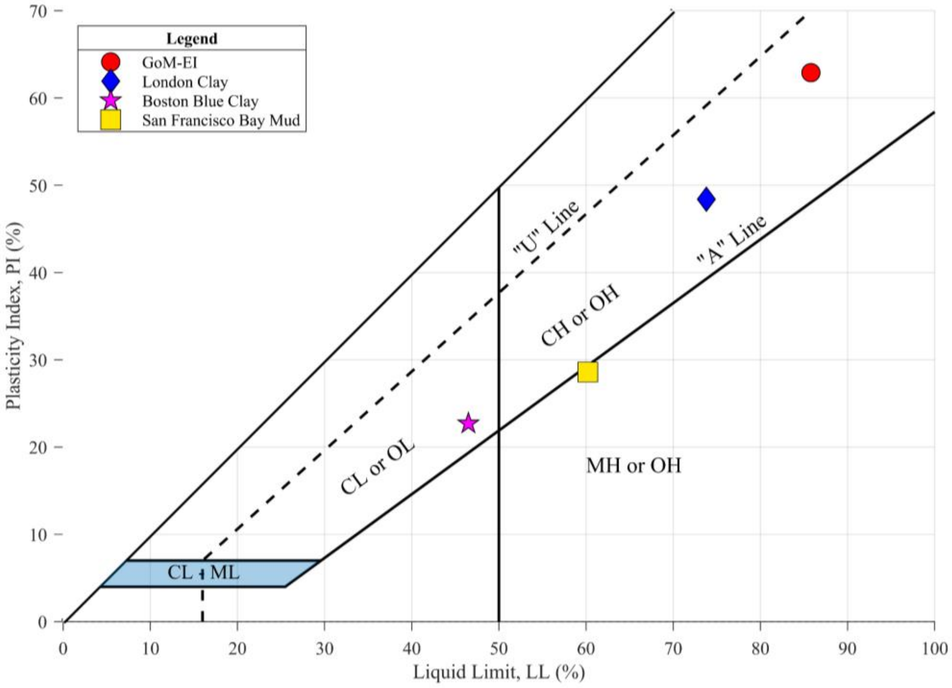

Figure 3-2 -GoM-EI material plotted on a Casagrande plasticity chart. Some other commonly tested clays have also been included for reference.

3.2.2 Permeability

The permeability of clays has been shown to strongly correlate with liquid limit, with higher liquid limits leading to lower permeabilities. Additionally, the mineralogy of the clay has also been shown to play an important role in clay permeability, with smectite rich clays displaying lower permeabilities than illite and kaolinite dominant clays. In Figure 3-3 it can be seen that

RGoM-EI has particularly low permeabilities for a given porosity, approaching two orders of magnitude lower than another common testing material – illite rich RBBC.

The permeability data presented below was used as an input for the Plaxis and Abaqus triaxial simulations (see section

Constitutive Modelling0 and B.4 for more information on computational modelling).

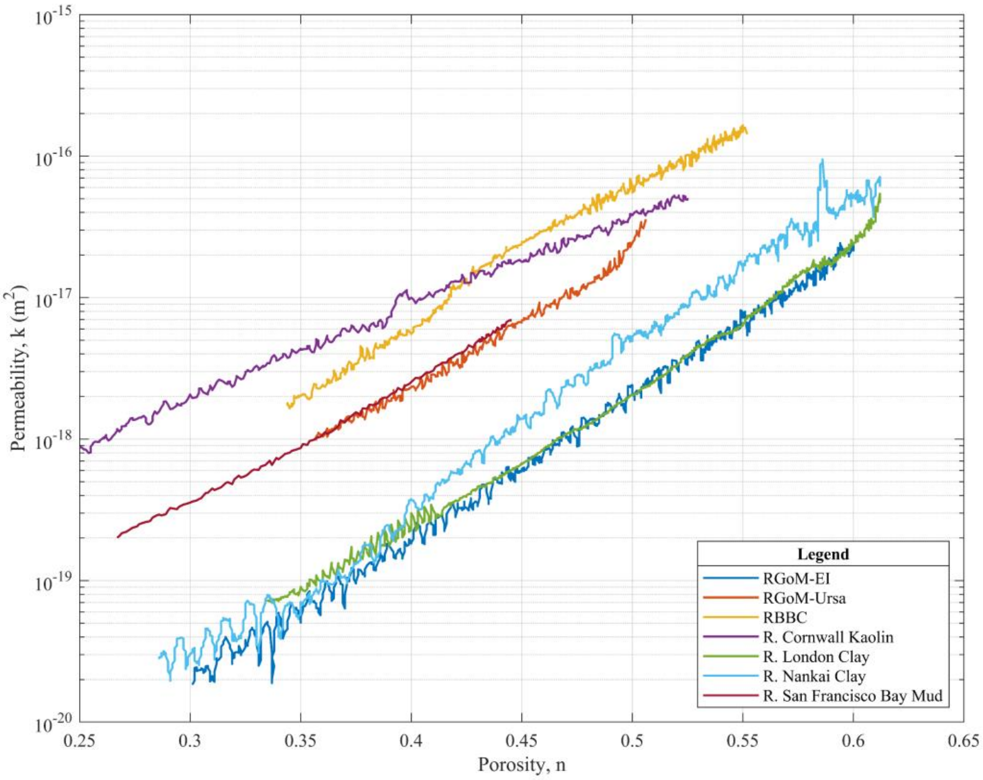

Figure 3-3 - Permeability data for a selection of resedimented clays is presented. Data is taken from Casey et al. (2013) and the UT GeoFluids library.

3.2.3 Mineralogy

As can be seen in Table 3-1, the dominant clay mineral in RGoM-EI is illite + illite-smectite at 44.4 (wt. %). The material has an overall clay fraction of 53.9 (wt. %). A separate analysis that was performed just on the clay-size particle fraction of the blended core shows illite+smectite to be dominant at 87 (wt. %).

Table 3-1 - Mineralogy of RGoM-EI material. Data is from (Betts 2014)*, determined using X-ray powder diffraction with the reference intensity ratio method* (Hillier 2000).

RGoM-EI overall mineralogy (wt. %)		**Clay-size fraction mineralogy (wt. %)**	
Quartz	27.8	Kaolinite	4
Plagioclase	5.3	Illite	8
K-Feldspar	4.0	Illite+Smectite	87
Calcite	1.2	Chlorite	1
Dolomite	0.8	Total	100
Siderite	1.0		
Pyrite	0.7	% Expandability	70-80
Anatase	0.2		
Barite	3.2		
Halite	0.2		
Muscovite	1.9		
Illite + I/S	44.4		
Kaolinite	9.1		
Chlorite	0.4		
Total	100.2		

3.2.4 Specific Gravity

The specific gravity of the GoM-EI material was measured using the water submersion method, and a value of 2.775 obtained (Betts 2014). The water submersion method was carried out in accordance with ASTM standard D854-14 (ASTM International 2014).

3.2.5 Compressibility

RGoM Eugene Island Clay follows the trend of other high plasticity clays, where they exhibit larger void ratios at low effective stresses and show high levels of compressibility with increasing vertical effective stress. This tendency of higher plasticity clays leads to a convergence of all clays with respect to void ratio at high stresses – this can be seen in Figure 3-4. The compression behaviour of RGoM-EI can be described by an n-log(σ'_{v}) type relationship.

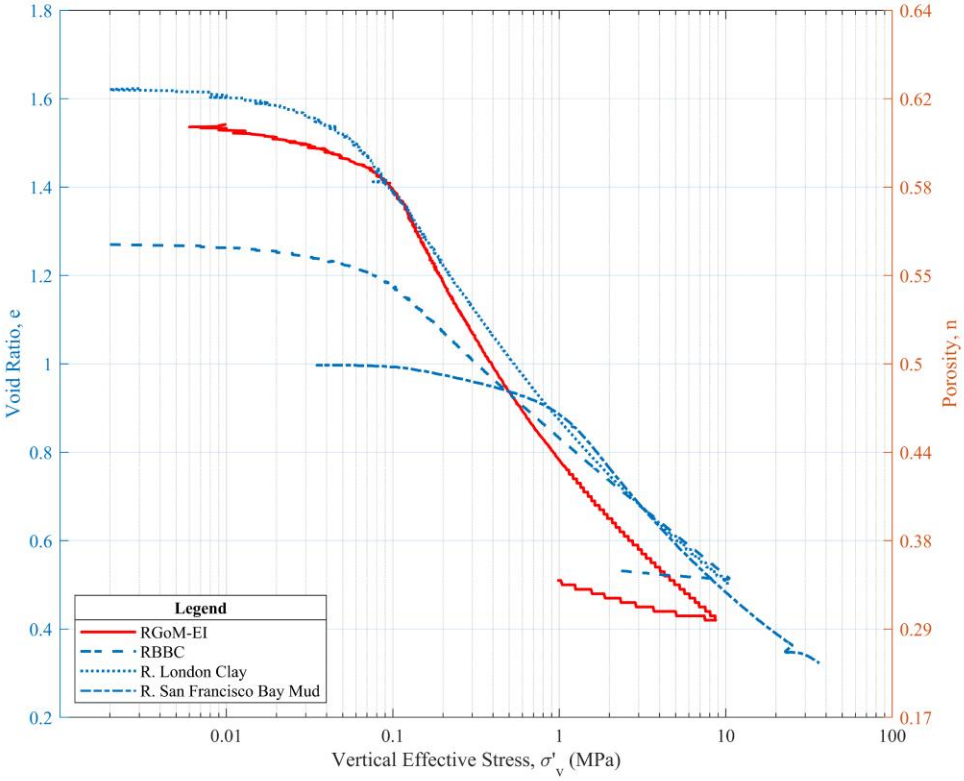

Figure 3-4 - Compression curve for RGoM-EI vs other common resedimented testing clays.

3.3 Resedimentation Procedure

Prior to the development of a resedimentation technique for creating soil specimens, in situ samples had to be extracted and prepared before being tested within a laboratory. This process presents a number of hurdles for extracting meaningful material behaviour from the test data. Firstly, spatial variability in the soil, even over a small area, can vary tremendously. Thus it is difficult to achieve repeatable results from in situ samples. Additionally, when extracting the sample, the existing stress state is altered. A range of other factors, such as water content also begin to change, and the very extraction process imposes stresses on the soil that affect its natural fabric. As such, a technique that can allow reproducible samples to be created within a laboratory environment would be greatly beneficial.

Results from x-ray radiography show that samples from borings can undergo significant disturbance and expansion during sampling and transportation. Large voids can also be caused by gas expansion when extracting samples from significant depths.

The resedimentation procedure employed at the geotechnical laboratory at Tufts has been perfected over the last few decades. It was pioneered at MIT in an attempt to create uniform specimens at any desired stress level. The technique attempts to mimic in situ conditions by applying a zero lateral strain boundary. The technique involves first the production of a clay suspension in salt water, or slurry, deposition of this slurry into a consolidometer and then consolidation of the material. The final process is to extrude the specimen and trim it to match standard dimensions.

It is worth noting that resedimentation is not able to recreate layer induced anisotropy that is seen in intact samples. Layered soils may possess very different mechanical and hydrologic properties to their resedimented counterparts, and therefore resedimentation would not yield such an effective proxy for intact behaviour in this case.

3.3.1 Slurry

The resedimentation process begins with the production of a clay slurry. Clay powder that had been previously processed is mixed mechanically with salt water. For the GoM-EI clay powder, a mixing water content of 110 % was selected. Previous studies into resedimented clay sample preparation had suggested using mixing water contents twice the liquid limit of the clay (Sheeran and Krizek 1971), however this would have left significant amounts of free water on top of the slurry for RGoM-EI. The concentration of salt water added to the clay powder was modified to match the in situ salinity of 80 g/l (Losh and Wood (1995) found the range of in situ pore fluid salinities in the Eugene Island block 330 area varied between 74 to 80 g/l (80 g/l was selected for this research). The processed clay powder itself had been previously found to contain ~14 g/kg (Casey 2014) of salt, and so the salt concentration of the salt water added had to be adjusted prior to mixing with the clay to account for this.

Figure 3-5 - Image showing mixing of a clay powder, taken from (Casey 2014).

Figure 3-6 - Image showing GoM-EI clay powder after mechanical mixing with salt and water.

3.3.2 De-aeration

After mechanical mixing of the clay powder and salt water, the slurry was allowed temper over a 24-hour period. During this time, flocs of clay were broken down and exposed to free water. Prior to dispensing the slurry into the consolidometer, the mixture is de-aired to remove gas entrained within the slurry. The slurry was evacuated under 20 inches Hg pressure for a minimum of 5 minutes until no more bubbles could be seen rising to the surface. This a key step in being able to produce fully saturated samples within the consolidometer.

3.3.3 Deposition

The de-aired mixture was then transferred using a funnel into a manual pump. This pump is then used to fill the consolidometer with the slurry in a controlled manner, with care being taken not to introduce pockets of trapped air in the process. The consolidometer itself consists of a PVC cylinder of 2” internal diameter sitting inside a saline water bath. As load is applied to the slurry, pore water is driven from the mixture and the soil consolidates through a reduction in void ratio. Drainage is achieved within the consolidometer through two porous stones applied at the top and bottom. The porous stones prevent the slurry from escaping the consolidometer, whilst allowing the free movement of water to dissipate out of the specimen. These round stones are also used within the triaxial cell for the same purpose.

It is also worth noting that prior to filling with the clay slurry, silicon oil is applied to the inside of the consolidometers. This reduces side wall interface friction between the clay particles and the consolidometer, something which acts to reduce the actual preconsolidation stress that is applied to the specimens (Casey 2014). In order to further reduce the impacts of side wall friction, a spacer tube is placed at the bottom of the consolidometer allowing the specimen to strain from both ends. This halves the amount of side wall friction present.

In addition to the porous stones, nylon filter paper with a pore size of 0.4 μm was used. This filter paper sits between the slurry and the porous stones, keeping clay particles confined within the consolidometer whilst allowing the free drainage of water.

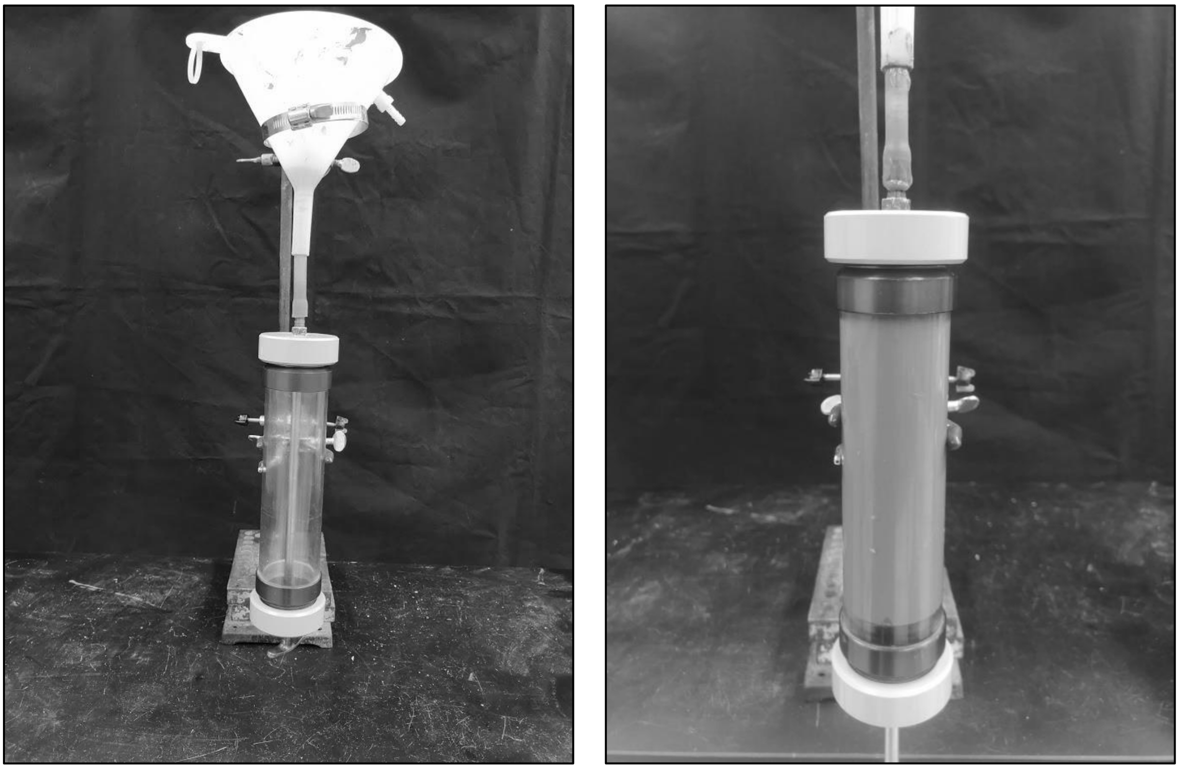

Figure 3-7 - Two images showing clay slurry being inserted into a suction pump. The pump is used to insert the slurry into the consolidometer.

3.3.4 Consolidation

Specimens are consolidated by incrementally increasing the total stress applied to the top of the specimen. After each increase in load, pore pressures inside the specimen are allowed dissipate. This leads to an increase in the vertical effective stress as load is transferred to the soil skeleton and a decrease in the total volume.

A load increment ratio is defined as $\frac{\Delta P}{P}$, where P is the current load applied and ΔP is the load to be added. For the consolidation of samples used within this research, a load increment ratio of 1 was selected. This was deemed a good balance between being able to produce samples in a timely manner, without being so large as to cause extrusion of the sample. The time between loading increments was chosen to be 2.5 days for the GoM-EI material. This was chosen by analysing the strain versus time curve for several load increments. The Square Root of Time method was then used to estimate the time to the end of primary consolidation; an example strain versus time curve can be seen in Figure 3-8, strains were measured using a Linear Variable Differential Transducer (LVDT). At 2.5 days between increments, reaching 10 MPa consolidation stress takes a minimum of 40 days. This length of time highlights some of the issues with testing RGoM-EI; the long consolidation times often caps the number of tests that can be run. It also explains why other materials such as RBBC, which consolidate much faster, are favoured as a research material.

3 different apparatus were used to consolidate from a slurry through to 10 MPa. The slurry was initially consolidated by applying physical weights, attached through a hanger, onto the slurry. After approximately 0.5 MPa consolidation stress, the specimen is transferred to a pneumatically actuated consolidometer. This device can be seen in Figure 3-9 and it enables higher loads to be applied much more conveniently. The pneumatically actuated consolidometer has a maximum load of 4 kN, corresponding to approximately 4 MPa for a standard sample with 9.35 cm^2 area. Finally, the specimen is transferred to a mechanical load frame for the last two load increments until 10 MPa vertical stress is reached. The mechanical load frame has a mechanical advantage of 100:1.

At stresses above 1 MPa, 3 hose clamps were used to restrain the consolidometer radially. This was needed to prevent cracks from propagating in the PVC tube when loads are applied and a corresponding step in pore pressure is seen inside the consolidometer.

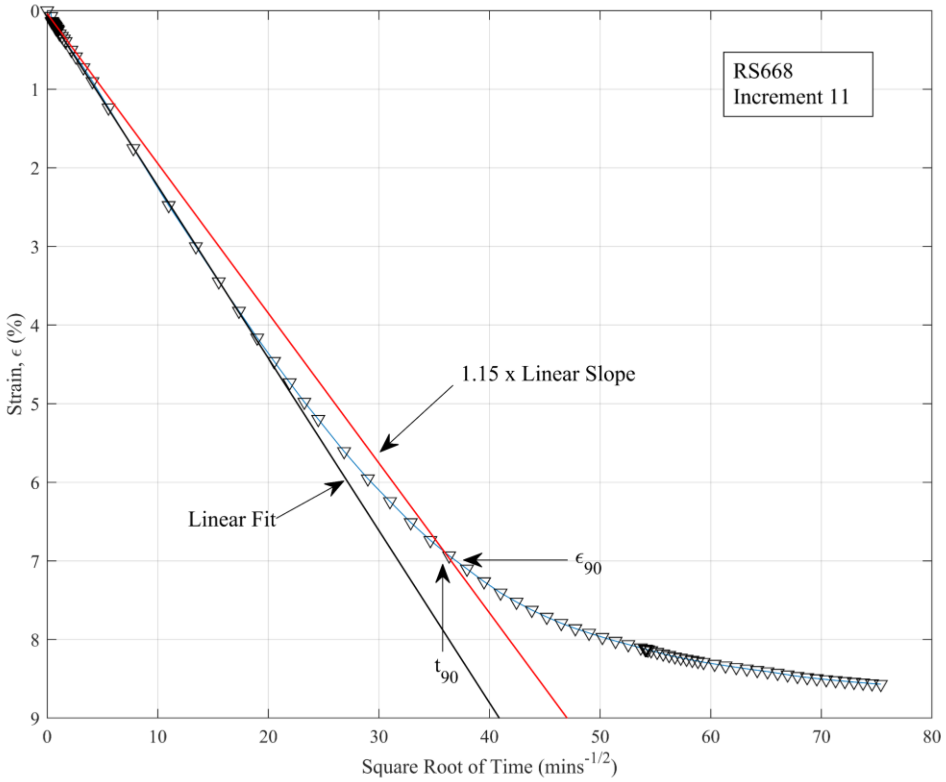

Figure 3-8 - Figure showing the Square Root of Time method used to estimate the time to end of primary consolidation in RGoM-EI material.

Figure 3-9 - Image showing a pneumatic actuator, which permits consolidation from between 0.25 - 5 MPa.

3.3.5 Extrusion and Trimming

Once the sample had reached the desired consolidation stress, samples were left for one cycle of secondary compression before being unloaded to OCR = 4. Research by (Santagata and Germaine 2002) has shown this leads to an approximately isotropic stress state within the sample – something which helps to minimise sample disturbance during extrusion from the consolidometer and subsequent transfer to the triaxial cell.

After the sample had been given adequate time to swell, a hydraulic extruder was used to force the sample from the consolidometer. Silicone oil applied to the inside of the consolidometer reduces the friction and therefore the amount of disturbance experienced by the sample during this step, though does not completely eradicate this effect. The sample is then wrapped in wax paper and transferred into a split-ring aluminium cylinder with a small amount of compression applied to secure the sample. This aluminium cylinder has height equal to the standard specimen size of 8.1 cm. A razor blade is then used to form a smooth, level surface on the top and bottom of the specimen. Larger trimmings from this process have their mass measured and are then dried in order to calculate an initial water content. A minimum of three trimmings are used for this and an average and standard deviation water content are calculated. After the specimen has been prepared, an initial mass, height and diameter are recorded.

4 Equipment

4.1 Introduction

This chapter begins with a high-level explanation of how the high pressure triaxial system that was used in this research operates. Subsequent sections then provide a detailed discussion of the various components that comprise the triaxial cell, as well as the systems responsible data for capture and controlling the PVAs.

4.2 Overview of High Pressure Triaxial System

The high pressure triaxial system used within this research comprises of 3 main parts, which together permit the testing of soils at consolidation stresses up to 100 MPa. The main triaxial cell is connected to a suite of transducers which measure the cell pressure, axial load, axial displacement, and pore pressure. These raw voltages are captured by a high precision auto scaling central data acquisition unit. The same voltages are also fed into a separate computer which runs the triaxial control programme. This programme uses PID algorithms to determine what voltage to send to the three DC motors that in turn control the triaxial device. These analogue control signals pass from the computer into the triaxial control unit, where DC motor controllers convert the signals into analogue power voltages to move the motors.

4.3 Automated Stress Path Triaxial Cell

The high pressure triaxial cell, which forms part of the high pressure triaxial system, was designed and built by researchers at MIT (Casey 2014). The cell has been seldom used since, with only a small number of successful tests run on the equipment to date. It has been designed to be capable of withstanding cell pressures well in excess of 100 MPa and is capable of automated feedback-controlled testing. It is capable of K_0 consolidation as well as both triaxial compression and triaxial extension following any desired stress path. The capability of performing triaxial extension is a key feature in enabling a full picture of a materials yield surface to be captured from testing.

The triaxial cell is comprised of a 1.5” thick stainless steel pressure chamber which fills with silicone oil during testing. Inside an axial piston connects to an internal load cell. This load cell is then screwed into a suction cap. The suction cap, which can be seen in Figure 4-2, contains a connection whereby a vacuum can be applied. This, in conjunction with an O-ring which seals the suction cap from the cell pressure, allows for triaxial extension to be performed. The top cap contains a drainage line which allows for the control of pore pressure at the top of the specimen. This drainage line leaves the top cap and coils around the specimen so that it can behave as a spring and minimise its impact on measurements as the specimen strains. A standard laboratory specimen of height 8.1 cm sits between the top cap and the base pedestal, which itself has a drainage line to allow for pore pressure control.

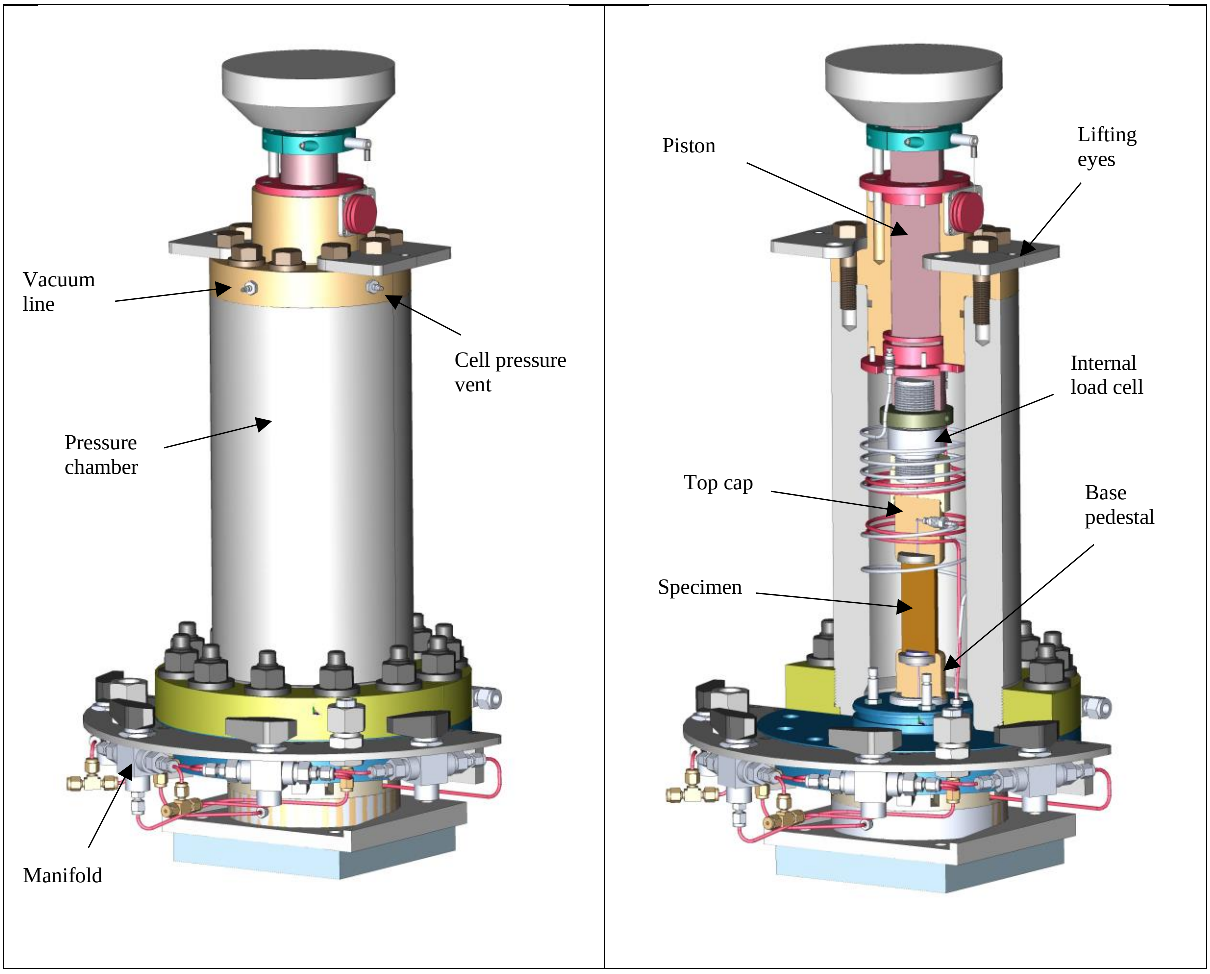

Figure 4-1 - On the left is a CAD image of the high pressure triaxial cell. The image on the right shows a slice through that cell, with the specimen visible.

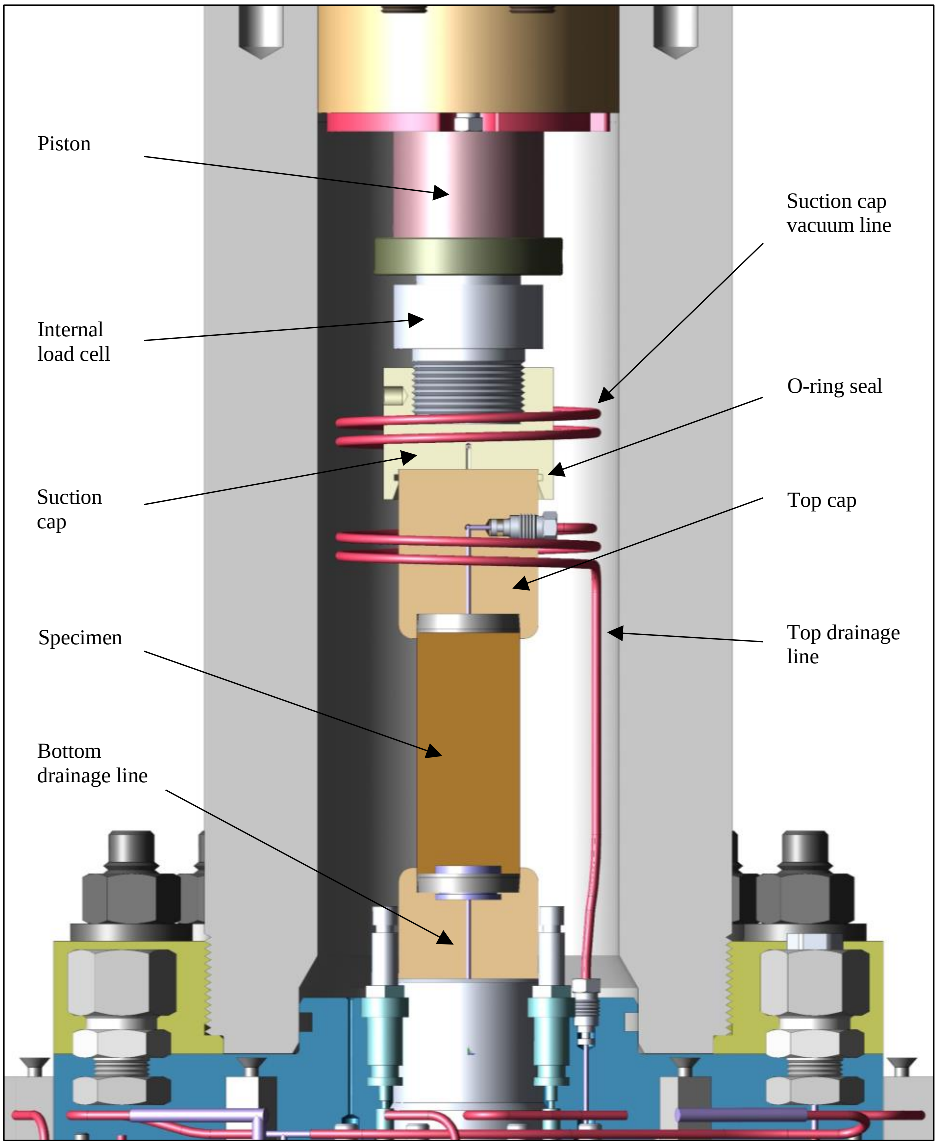

Figure 4-2 - Cross section of the high pressure triaxial cell

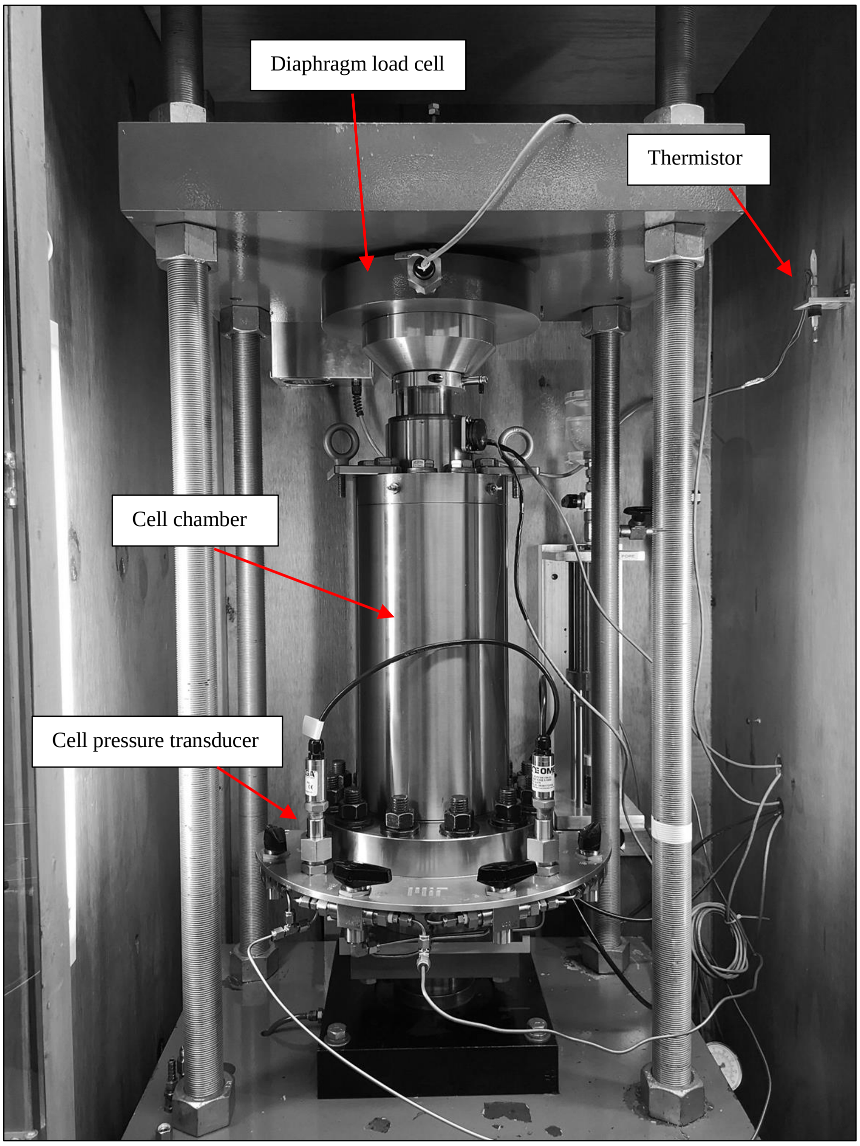

Figure 4-3 - Image of the high pressure triaxial cell contained inside a 24-ton load frame.

4.3.1 Load Frame

A 24-ton capacity load frame is used to contain the high pressure triaxial cell. The load frame contains a pneumatically actuated base that allows the triaxial cell position to be finely lowered and raised.

4.3.2 Silicone Oil

Silicone oil is used within the triaxial cell in order to apply a hydrostatic pressure to the specimen. Though other liquids can be used, silicone oil has been selected for several reasons.

Firstly, the fluid is chemically inert, and acts as a dielectric, allowing electronics to be contained within the cell. Transparency of the fluid also allows for visual observation of the specimen in low stress triaxial cells where the cell is made from an acrylic. In triaxial testing where latex membranes are used, silicone oil has been shown to not permeate through to the specimen.

4.4 Transducers

4.4.1 Displacement Transducers

Axial deformation of the specimen inside the triaxial cell is measured using a string potentiometer. These devices consist of a coiled wire connected to a spring via a spool (Figure 4-4). As the wire moves in and out of the device, a rotational sensor produces a voltage that is linearly proportional to the displacement of the wire. An advantage of a string potentiometer over an LVDT is that it is linear over its whole working range, as well as being simple to install and calibrate.

String potentiometers are also used within the triaxial systems PVAs (see section 4.5). Here they are used to measure the relative movement of the pistons inside the pressure chambers. For the backpressure PVA this is critical, as it is from this measurement that volume changes in the soil specimen are derived.

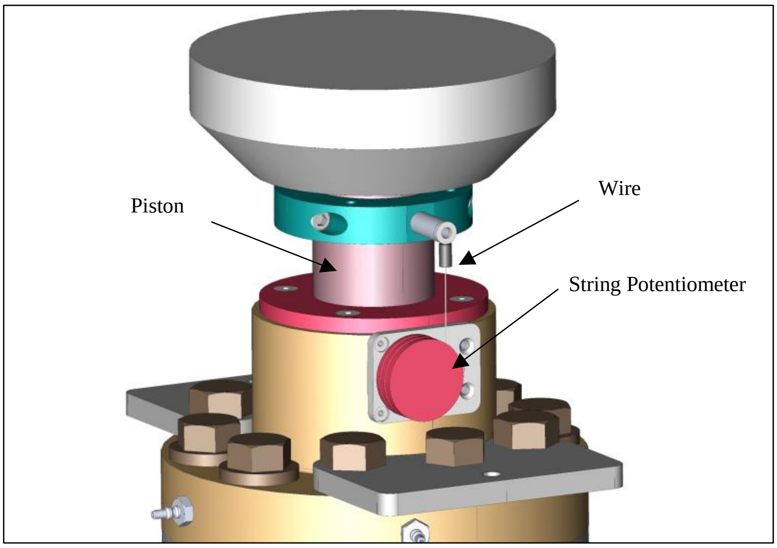

Figure 4-4 - Close up string potentiometer used to measure axial deformations.

4.4.2 Pressure Transducers

Two Omega PX309 stainless steel pressure transducers are used to in order to measure the cell pressure and the specimen pore pressure. A valve on the manifold allows either the backpressure or the sample pressure to be measured during testing.

The pressure transducers were calibrated using an oil deadweight calibration testing device. This process involves hydraulically connecting the transducer to the testing device. Then weights are applied which generates a known reference pressure, and the voltage from the transducer is recorded. The results from one such calibration is shown in Figure 4-6. The device is very linear over the pressure range tested, with no visible hysteresis at that scale.

Figure 4-5 - Image of pore pressure transducer located on the base of the high pressure triaxial cell.

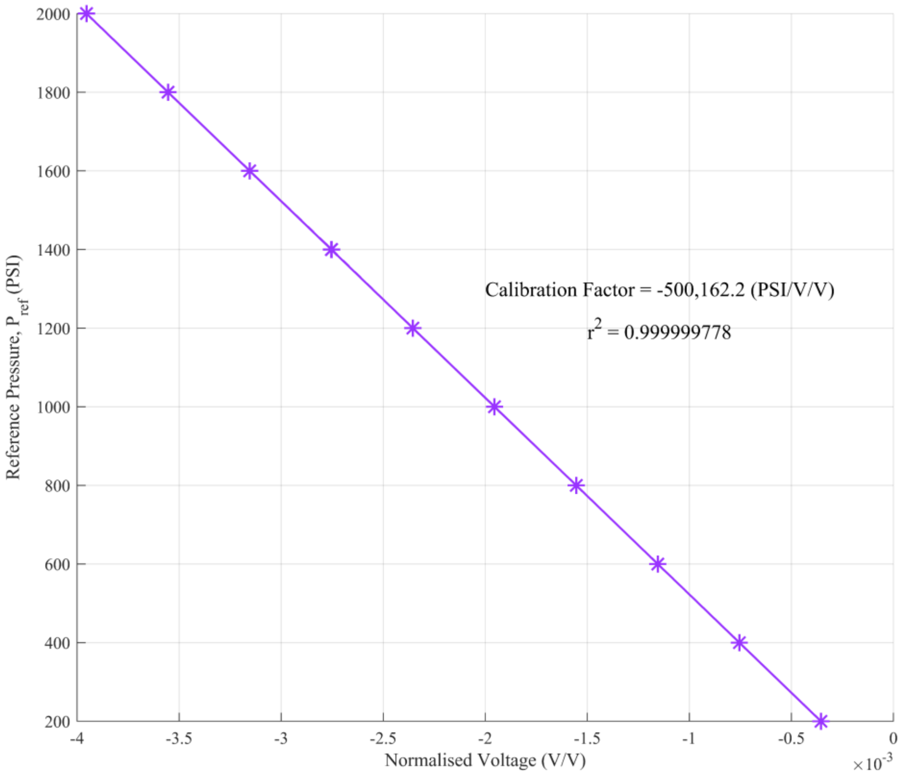

Figure 4-6 - Pressure transducer calibration.

4.4.3 Load Cell

The high-pressure cell has an internal load cell (Futek® LCM550) of 222kN capacity. Since we are interested in the deviator load being applied to the sample, one must correct for the force exerted on the load cell from the cell pressure. The high-pressure cell was run up to 80 MPa and back to atmospheric pressure two times. The data are presented in Figure 4-7 and show that the relationship is repeatable with only a small amount of hysteresis. A third order polynomial was fitted to this force versus pressure data allowing a correction to the load cell reading to be made at any given cell pressure. This relationship was included in both the control programme and the data reduction programme. In Figure 4-7, there is a step change in the axial load measured at around 70 MPa. This change corresponds to a change in load of approximately 7 kg. This step change is repeatable and occurs at the same pressure regardless of whether it is unloading or reloading. The repeatability of this error suggests that it is mechanical in nature, however as it is such a small error in relation to the capacity of the load cell, it can be safely ignored for these experiments.

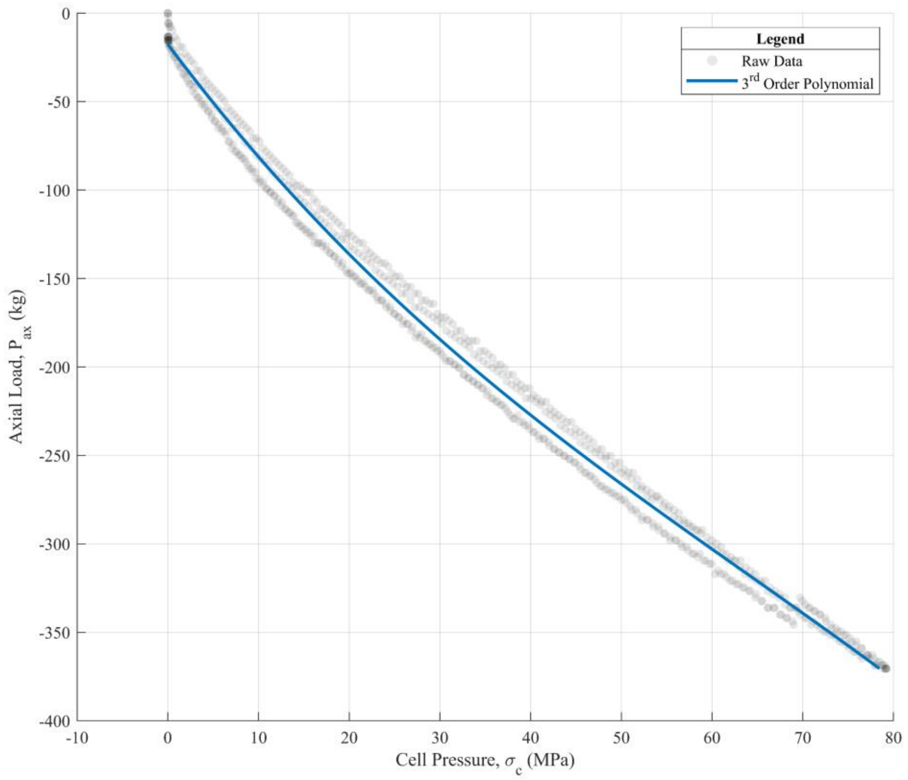

Figure 4-7 - Internal load cell calibration

4.4.4 Resolution

Table 4-1 - Table of transducer specifications, adapted from (Casey 2014).

	Transducer Range	**Precision**		**Resolution**	
		ADC	Central Data acq.	ADC	Central acq.
Axial displacement	7.6 cm	0.00003 mm (0.0024 mV)	0.0014 mm (0.1 mV)	0.00004%	0.00174%
Specimen volume	47 cm^3	0.04 mm3 (0.0024 mV)	1.75 mm^3 (0.1 mV)	0.00006%	0.00233%
Cell pressure	69 MPa	1.45 kPa (0.00024 mV)	6.03 kPa (0.001 mV)	0.0021%	0.0087%
Pore pressure	34 MPa	0.08 kPa (0.00024 mV)	0.31 kPa (0.001 mV)	0.0002%	0.0010%
Load cell	222 kN	0.040 N (0.0000024 mV)	18.6 N (0.001 mV)	0.0001%	0.0317%

4.5 Pressure Volume Actuators

The high-pressure testing system requires three pressure volume actuators (PVAs) to control the stresses and pore pressure applied to the specimen. The PVAs are custom built, consisting of a pressure chamber with a piston that are actuated by a DC motor through a geared mechanism. The fluid inside the PVAs are salt water, hydraulic fluid and silicone oil for the backpressure, axial and cell PVAs respectively. Three types of PVA are used with differing specifications to match their varying requirements. One lower capacity PVA is used for the backpressure and is capable of generating up to 14 MPa of pressure though the use of a 0.5-ton Duff-Norton® inverted screw jack. The axial and cell pressure PVAs are higher capacity, differing only in the cross-sectional area of the piston. The axial PVA piston has a 6.35 cm diameter which yields a maximum pressure of 28 MPa and a volume capacity of 800 cm^3. The cell pressure PVA has a piston diameter of just 3.18 cm resulting in a maximum pressure of 110 MPa and a volume capacity of 200 cm^3. Both the axial and cell pressure PVAs use 10-ton Duff-Norton® inverted screw jacks. The screw jacks themselves are driven by DC motors which are connected via a spiral bevel gear.

Limit switches are used as a mechanical fail-safe mechanism to ensure all three PVAs are not driven beyond their working ranges. In addition, mechanical pressure relief valves are connected to prevent maximum pressures being exceeded and equipment being damaged due to a sensor fault or user error.

Shown in Figure 4-8 is a CAD model of the 28 MPa PVA used in the system. This PVA delivers hydraulic pressure to the piston in the cell, controlling the axial stress placed upon the sample.

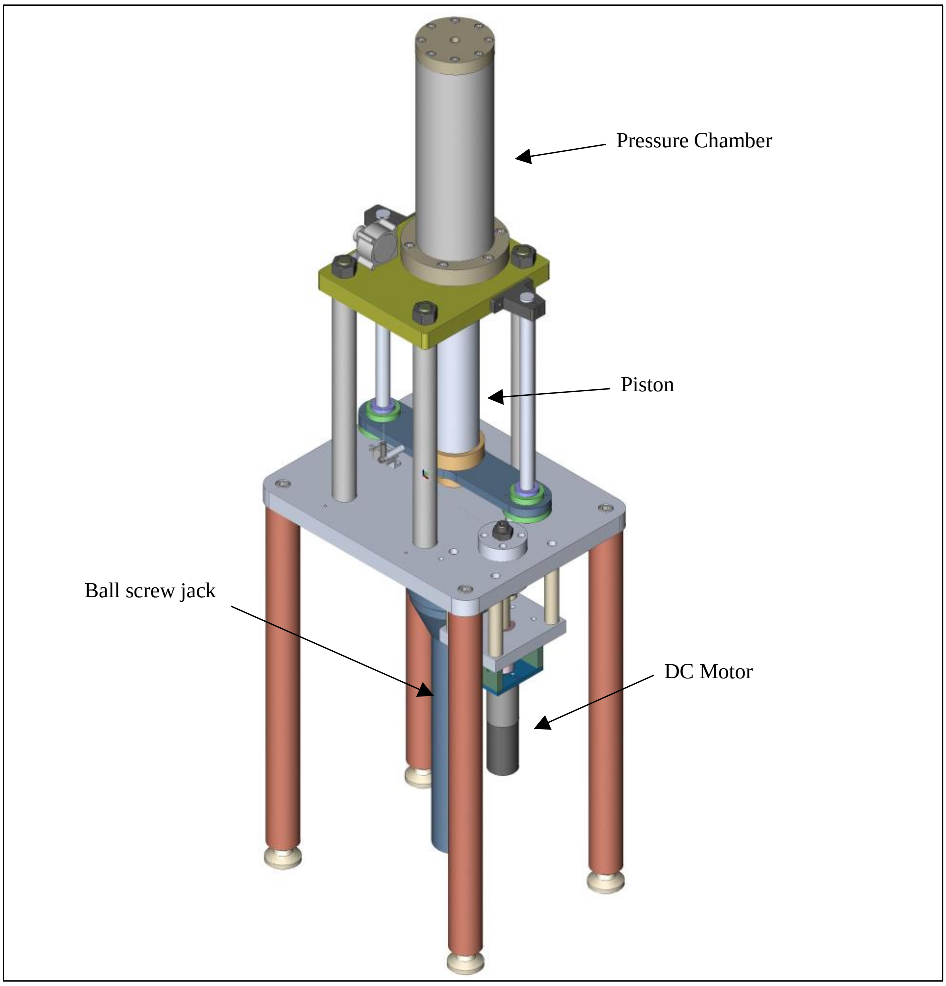

Figure 4-8 – 28 MPa PVA used within the high-pressure system to drive the 24-ton load frame.

4.6 DC Motors

3 Maxon Motors® DC motor were used to actuate the three PVAs of the triaxial system. For generating the backpressure within the system, a motor that provided 80 mNm of torque was used. The cell pressure and hydraulic load frame were both driven by higher capacity motors that provided 184 mNm of torque.

4.7 DC Motor Controllers

Maxon Motors® ESCON 50/5 DC motor controllers were used to control voltage to the axial, cell and pore pressure DC motors. The controllers are programmable via a micro-USB interface, allowing parameters such as maximum RPM, and input voltage range to be set. Our motors required an input of +/- 4V, with the ability to be driven in both the CW and CCW directions. The limit switches were also connected to terminals on the controllers, that would kill the DC motors and provide a manual override when the input was low.

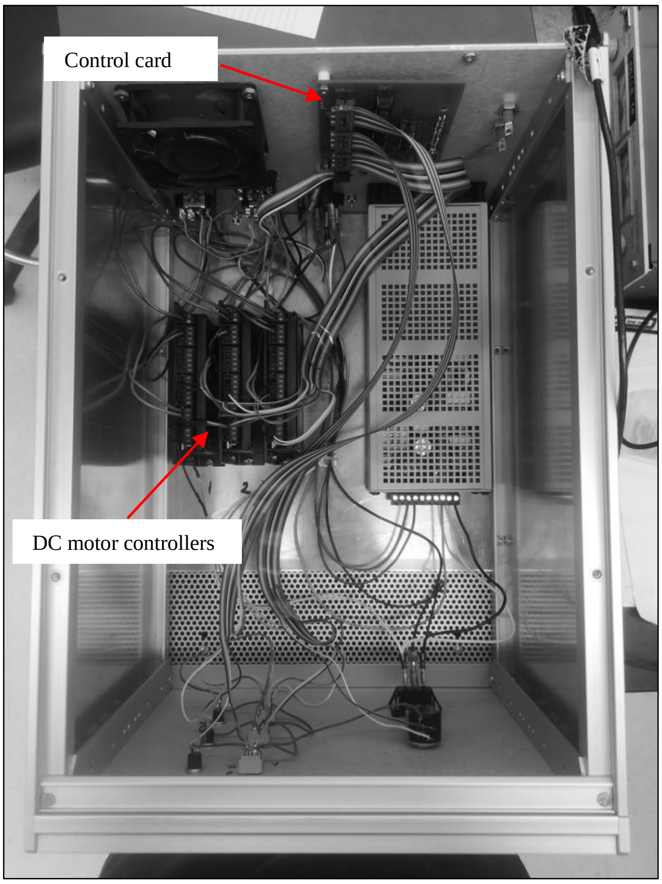

Figure 4-9 - Image of a triaxial cell control box containing three DC motor controllers.

4.8 Temperature Control

In order to reduce the impact from environmental factors on the test data, temperature is controlled during consolidation and shearing within the triaxial housing. Infrared heat lamps attached to a simple temperature-controlled relay circuit maintain the temperature within a range of ± 0.1°C (Casey 2014). A fan located inside the housing also helps to distribute the air evenly.

4.9 Triaxial Control System

The triaxial control system used for the high pressure triaxial cell has been developed and improved by various researchers over the last three decades (Sheahan 1991), (Casey 2014). The triaxial control system runs independently from the data acquisition system (see section 4.10) and utilises closed loop feedback to control three DC motors on the cell, axial and pore PVAs. Raw voltages from transducers on the triaxial cell and PVAs pass into a multichannel analogue to digital converter. Digital signals feed into the computer and subsequently the triaxial control programme. Here target engineering values are calculated and converted into voltages to send to the DC motors. The magnitude of the voltage depends upon the type of the control algorithm being implemented and the magnitudes of the control constants.

4.9.1 Analogue to Digital Converter

A multichannel analogue to digital converter is used within the triaxial control system to convert analogue signals from the transducers into digital values that can be interpreted by the control programme. The analogue to digital converter used within this system is an AD1170 high-resolution (22-bit resolution) programmable integrating A/D converter (ADC). The ADC provides channels with fixed gain values of 10,100 or 1000, a value which is adjusted depending on the output of a particular sensor. The ADC is connected via an ISA interface to a card that ports the digital signals through USB to the computer. Though integrating ADCs are not suited to high-speed applications, they are ideal candidates for settings which are low frequency yet require high resolution (Kester 2004). This is the case for triaxial testing and explains why integrating ADCs have been chosen over other common architectures such as Flash and Delta-Sigma ADCs.

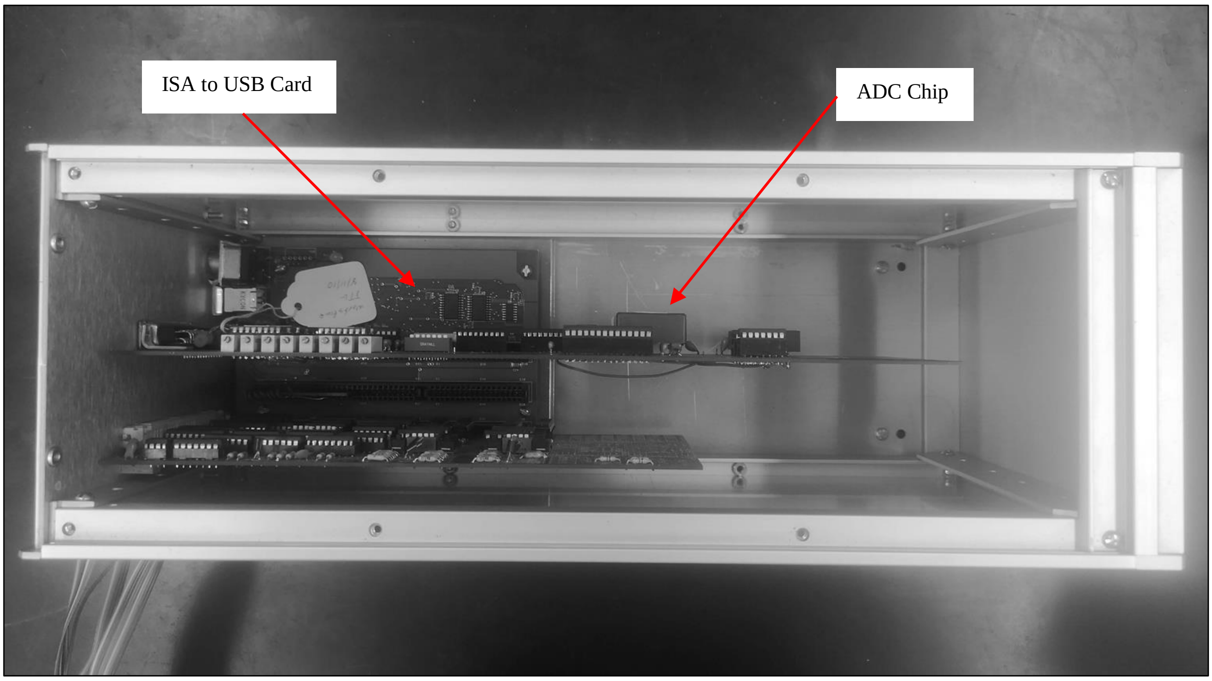

Figure 4-10 - Image of analogue to digital converter unit.

4.9.2 Digital to Analogue Control Card

In Figure 4-9 can be see the digital to analogue control card located inside the triaxial control box. Signals originating from the PVA limit switches, manual control signals, DC motor control signals and digital to analogue converter are passed through this card. Signals from this card then enter the DC motor controllers described in section 4.7. This system ultimately allows for the precise automatic and manual control of the three degrees of freedom in a triaxial cell.

4.9.3 Triaxial Programme

Programmes that control the running of the triaxial tests were written and developed in QuickBASIC, an IDE and compiler that runs on MS-DOS. These programmes were developed at MIT in the 1980s and allow for a range of testing protocols such as K_0 consolidation to be carried out. The programme takes voltages from a suite of sensors as its input, and outputs digital signals to a digital to analogue converter which controls the operation of the DC motors on the PVAs.

4.10 Data Acquisition System

All voltages from transducers on the high pressure triaxial system, along with all other transducers in the laboratory, feed into the Central Data Acquisition System (CDAS). This system runs independently from the Triaxial Control System described in section 4.9. A key strength of using the CDAS is that it can capture resolution in voltage two orders of magnitude greater than traditional voltmeters, such as the voltmeter used to monitor the triaxial system during operation. Custom software running on a computer connected to the HP 3497A Data Acquisition machine (Figure 4-11) allows various data capture parameters to be selected. The programme allows for any of the 200 data channels in the laboratory to be selected and data to be captured at any chosen linear time interval or captured in log time. The system also enables multiple data streams to be captured simultaneously within the laboratory.

Figure 4-11 - HP 3497A data acquisition control unit, used to capture readings from the high pressure cell

4.11 Data Analysis

A programme written in QBasic was used to convert the raw test data voltages into engineering values. Calibration factors, load offsets and apparatus compressibility were combined with voltages recorded by the central data acquisition system to produce values such as strain, vertical effective stress, radial effective stress and pore pressure.

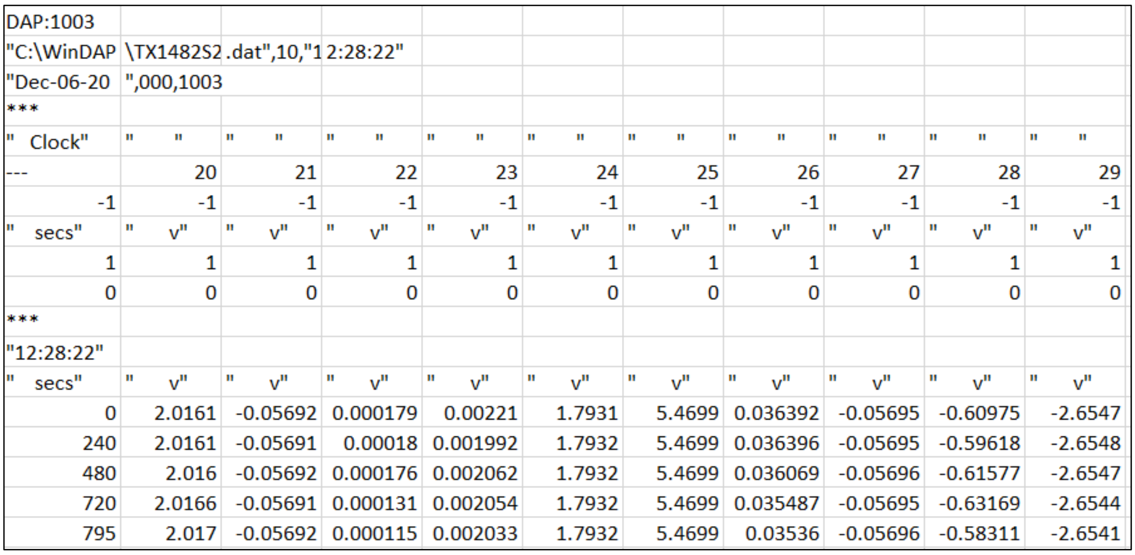

DAP:1003										
"C:\WinDAP	\TX1482S2	.dat",10,"12:28:22"								
"Dec-06-20	",000,1003									
***										
" Clock"	" "	" "	" "	" "	" "	" "	" "	" "	" "	" "
---	20	21	22	23	24	25	26	27	28	29
-1	-1	-1	-1	-1	-1	-1	-1	-1	-1	-1
" secs"	" v"	" v"	" v"	" v"	" v"	" v"	" v"	" v"	" v"	" v"
1	1	1	1	1	1	1	1	1	1	1
0	0	0	0	0	0	0	0	0	0	0
***										
"12:28:22"										
" secs"	" v"	" v"	" v"	" v"	" v"	" v"	" v"	" v"	" v"	" v"
0	2.0161	-0.05692	0.000179	0.00221	1.7931	5.4699	0.036392	-0.05695	-0.60975	-2.6547
240	2.0161	-0.05691	0.00018	0.001992	1.7932	5.4699	0.036396	-0.05695	-0.59618	-2.6548
480	2.016	-0.05692	0.000176	0.002062	1.7932	5.4699	0.036069	-0.05696	-0.61577	-2.6547
720	2.0166	-0.05691	0.000131	0.002054	1.7932	5.4699	0.035487	-0.05695	-0.63169	-2.6544
795	2.017	-0.05692	0.000115	0.002033	1.7932	5.4699	0.03536	-0.05696	-0.58311	-2.6541

Figure 4-12 - Example raw data file showing channel voltages.

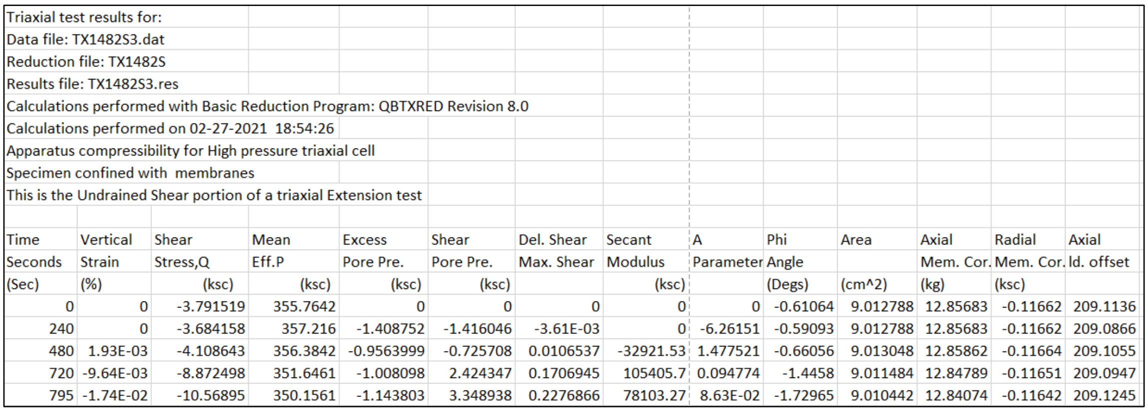

Triaxial test results for:
Data file: TX1482S3.dat
Reduction file: TX1482S
Results file: TX1482S3.res
Calculations performed with Basic Reduction Program: QBTXRED Revision 8.0
Calculations performed on 02-27-2021 18:54:26
Apparatus compressibility for High pressure triaxial cell
Specimen confined with membranes
This is the Undrained Shear portion of a triaxial Extension test

Time Seconds (Sec)	Vertical Strain (%)	Shear Stress,Q (ksc)	Mean Eff.P (ksc)	Excess Pore Pre. (ksc)	Shear Pore Pre. (ksc)	Del. Shear Max. Shear	Secant Modulus (ksc)	A Parameter	Phi Angle (Degs)	Area (cm^2)	Axial Mem. Cor. (kg)	Radial Mem. Cor. (ksc)	Axial ld. offset
0	0	-3.791519	355.7642	0	0	0	0	0	-0.61064	9.012788	12.85683	-0.11662	209.1136
240	0	-3.684158	357.216	-1.408752	-1.416046	-3.61E-03	0	-6.26151	-0.59093	9.012788	12.85683	-0.11662	209.0866
480	1.93E-03	-4.108643	356.3842	-0.9563999	-0.725708	0.0106537	-32921.53	1.477521	-0.66056	9.013048	12.85862	-0.11664	209.1055
720	-9.64E-03	-8.872498	351.6461	-1.008098	2.424347	0.1706945	105405.7	0.094774	-1.4458	9.011484	12.84789	-0.11651	209.0947
795	-1.74E-02	-10.56895	350.1561	-1.143803	3.348938	0.2276866	78103.27	8.63E-02	-1.72965	9.010442	12.84074	-0.11642	209.1245

Figure 4-13 - Data file after reduction, showing engineering values. Revision 8.0 of the data reduction software was used in this work.

5 Testing Procedures

5.1 Introduction

This chapter describes in detail the various procedures employed in the laboratory to perform triaxial tests on resedimented specimens at high stress. All of the procedures have been developed over multiple decades of research, with techniques being fine-tuned with each iteration and for differing applications. For this research, the use of a relatively new high-pressure triaxial cell necessitated the use of techniques that would not be appropriate for specimens consolidated to lower stresses for example.

An explanation of how resedimented specimens are prepared prior to insertion inside the triaxial cell is given first. Then a description of the three main testing phases is also given. These phases are backpressure saturation, consolidation, and undrained shearing.

5.2 Specimen Set Up and Initial Pressure-up

After a specimen has been prepared for testing in the manner described in Chapter 0, it is ready to be inserted into the triaxial cell so that it can be tested.

First porous stones (made from 54 grit vitrified bond stone (Casey 2014)) are placed in the base pedestal and in the top cap. The porous stone allows fluid to drain from the specimen during testing whilst preventing clay particles from blocking the drainage lines. Due to the high initial consolidation stress of 10 MPa and the very low water content of the specimen at this stress ($w \approx 18$ %), no filter paper was required during set up of the specimens, with the stones being directly in contact with the specimen.

With the stones in place, the specimen is placed in between the base pedestal and top cap (see Figure 4-2). Then a membrane is placed over the specimen as quickly as possible to prevent further changes in water content. The choice of membrane material used in a triaxial test must be carefully considered and the choice is a function of the material consistency and the magnitude of stresses that will be encountered during testing (Germaine and Germaine 2009). Traditional rubber membranes were deemed not to be appropriate at the cell pressures that would be encountered within this testing regime. Rubber membranes have been found to become porous above certain pressures, and previous research with this equipment had encountered a high rate of internal leaks using commercial latex membranes.

For this research PVC (meeting AMS/MIL-DTL-23053/2 standard) heat-shrink tubing was selected as the membrane material in the triaxial tests. The heat-shrink tubing allowed an excellent seal to be formed whilst being strong enough to resist the large forces that are exerted on the membrane at stresses reaching 100 MPa. The PVC is also more abrasion and chemically resistant than traditional rubber membranes. The impact of the membrane stiffness on the stresses through the sample was quantified using an analytical membrane equation, the results of these calculations and material testing of the PVC are given in Appendix A.

Once the PVC tubing was inserted over the specimen and caps, a heat gun was used to thermally shrink the membrane onto the sample. This process was done as quickly as possible to avoid excessive heat transfer into the specimen. The initial 2” radius tubing would shrink to a 1” radius with a wall thickness after shrinking of 0.05”. After the membrane had been set, the top and bottom drainage lines were opened and connected to a vacuum. The vacuum line passed through a flask filled with water, allowing for the detection of a leak in the system if air bubbles are detected. After passing the leak check, the drainage lines were closed with the vacuum still applied; this helps to keep the sample assembly rigid during the subsequent stages of specimen set up and the transfer of the triaxial cell into its enclosure.

Next. steel tying wire was used to provide a further seal on the membrane at the top cap and base pedestal; this can be seen in Figure 5-1. Two steel loops were applied to both the base pedestal and top cap.

Figure 5-1 - Image showing steel tying wire (Left) and the tying wire used to create a seal between the PVC membrane and base pedestal (Right)

End cutting nippers pinch the tying wire, and a twisting motion is used to strain the wire and pretension the loop to create a robust seal. This method appeared effective throughout the testing regime, with no internal leaks being recorded. Leak checks were performed at the end of backpressure saturation (section 5.3) and consolidation (section 5.4) by closing the drainage valves for 5 minutes and observing the measured pore pressure over time.

With the specimen fully prepared, the drainage line connected to the top cap, and the piston fully extended, the triaxial cell housing was lowered onto the base. Bolts connecting the cell to the base were then pretensioned to 140 Nm of torque through a torque wrench. Next the axial piston was carefully lowered onto the specimen. If triaxial extension tests were to be performed, an O-ring was included in the suction cap and a vacuum was applied between the suction cap and the top cap. After confirming correct seating of the piston by measuring its height relative to the cell, the zero reading for the axial displacement transducer is recorded. The zero for the internal load cell is recorded prior to lowering onto the sample.

After securing the base to the pressure chamber, the 109 kg triaxial cell was lifted into its temperature-controlled housing with the use of a hand winch operated forklift. After this, the load frame pedestal was then raised using fine adjustment of pneumatic regulators that allowed the pressure in the hydraulic fluid to be controlled. The triaxial cell was raised so that it just contacted the top of the load frame. This could be monitored by looking at the voltmeter reading on a diaphragm load cell that is embedded within the load frame (the location of the diaphragm load cell can be seen in Figure 4-3). When that point was reached, a valve to the pneumatic regulators was closed, fixing the triaxial cell in position. The cell was then filled with silicone oil until it could be seen flowing from a venting valve at the top of the cell. Throughout initial pressure up and backpressure saturation, a small deviator load of 100 KPa is applied to the sample, this is consistent with previous experimental work on this cell (Casey 2014). Without this, there is a risk the top cap becomes unseated, leading to hydrostatic conditions and inaccurate axial deformation measurements.

After filling the cell, the cell pressure was raised to 1.5 MPa to prevent swelling of the sample when pore fluid is brought into the system. This value was also used in previous research for RGoM-EI specimens consolidated to 10 MPa (Casey 2014).

This whole set up process was carried out in dry conditions. Exposing the sample to water before any confining stress was on the sample would have led to swelling. The final step in the specimen set up is to reapply the vacuum to the drainage lines, before releasing the vacuum and allowing 80 g/l salt water to be drawn into the system. Readings are then taken, and the specimen was allowed to equilibrate over 24 hours before beginning the next phase of the test.

5.3 Backpressure Saturation

After the initial pressure up stage, the sample underwent a process known as backpressure saturation. This involves increasing the pore pressure in the system so as to ensure the drainage lines that connect the pore pressure PVA to the specimen are fully saturated. Fully saturated conditions are essential for being able to interpret meaningful behaviour from the undrained test data. A key assumption of Terzaghi's principle of effective stress is that the soil must be fully saturated. Additionally, a fully saturated sample is essential for the K_0 consolidation algorithm to work. The control algorithm assumes that all volume changes measured are solely from pore fluid entering or leaving the specimen.

When setting up a triaxial test, despite care being taken, small amounts of air are inevitably entrained in the tubing and valves when setting up the specimen. As determined by Henry's law, increasing the partial pressure of a gas, increases its solubility in a given liquid. Hence by increasing the pore pressure above atmospheric pressure, the trapped air can be dissolved into the pore fluid and allow saturated conditions to be reached. Due to the presence of this air trapped in the system, a small amount of pore fluid is expected to enter the sample during backpressure saturation. This results in a small negative volumetric strain being recorded at this stage. Larger volumetric strains indicate that there is a leak which needs to be rectified before consolidation can begin.

Figure 5-2 is an example of data from the backpressure saturation portion of a triaxial test that was undertaken. During this process, a backpressure of approximately 100 kPa was applied to saturate the specimen. This is performed at constant effective stress, so the axial load and cell pressure are adjusted as the pore pressure is increased to 100 kPa. The early portion of the figure shows volume going into the triaxial system after the 100 kPa step increase in pressure. The rate of volume injection initially appears to be reducing, indicating that air in the lines is dissolving into the water and that the system is saturating. However, after approximately 4 hours, there is a marked increase in the rate of volumetric strain, and this rate then continues to hold steady with time. This is a clear indication of an external leak in the system, which was identified and sealed prior to consolidation.

In addition to evaluation of the volumetric strain vs time data, a B-value check can be performed to assess saturation, this is described in the next section.

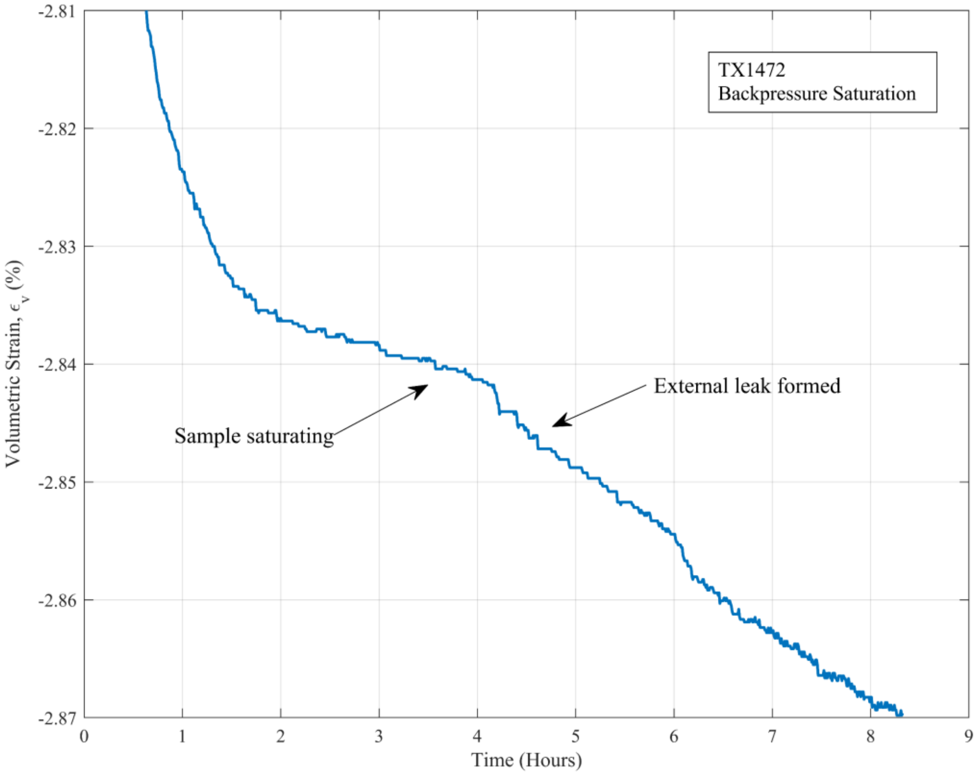

Figure 5-2 - Volumetric strain data during backpressure saturation for triaxial test TX1472.

5.3.1 B-Value and Apparatus Compressibility

After backpressure saturation, and prior to K_0 consolidation, the sample undergoes a B-value check. This term was first coined by Skempton (1954) when he derived an equation relating changes in pore pressure to changes in total stresses. This check is used to assess the saturation of the sample. The top and bottom drainage lines are closed and a step change in the cell pressure is applied rapidly by the control programme, whilst simultaneously maintaining zero change in shear stress on the specimen. The resulting change in pore pressure is then measured, with the B-value being the ratio of pore pressure delta to octahedral stress delta. This is also known as the undrained pore-pressure ratio.

$$B = \frac{\Delta u}{\Delta \sigma_{oct}} \tag{5-1}$$

Theoretically, for a fully saturated soil specimen ($S = 100\ \%$) with no soil, pore fluid or system compressibility, the B-value is equal to 1. Real soil skeletons and pore fluids do contain finite compressibility however, something which was accounted for in a derivation of $\frac{\Delta u}{\Delta \sigma_{oct}}$ by Bishop (1973). The derivation contained several key assumptions: that the soil skeleton behaves as an elastic, isotropic material, that all pores are hydraulically connected and that the pore fluid is linearly compressible. This work resulted in the following expression for the undrained pore-pressure ratio:

$$\frac{\Delta u}{\Delta \sigma_{oct}} = \frac{1}{1 + n(C_w - C_s)/(C - C_s)} \tag{5-2}$$

Here C_w and C_s represent the compressibility of the pore fluid and soil grains, respectively. C is defined as the bulk compressibility of the soil skeleton, equal to the inverse of its bulk modulus. It can be defined through two elastic parameters with the following formula:

$$C = \frac{3(1 - 2\nu)}{E} \tag{5-3}$$

As the bulk compressibility reduces in equation 5-2 , the ratio C_w/C, something which is negligibly small at lower stresses in most soils, increases and begins to reduce the maximum theoretical B-value that can be obtained. This is of significance for this work, as specimens are consolidated to high stresses. The compressibility of water was taken as 48.9 x 10^{-5} MPa^{-1}, and the clay grains as 2 x 10^{-5} MPa^{-1}.

So that pore pressure can be measured in a triaxial device, the specimen must be connected hydraulically to a pore pressure transducer. By introducing drainage lines, valves, and transducers into one hydraulically linked system, one also introduces an amount of compressibility into the system. The compressibility of all these components, including the pore fluid contained within them, is collectively referred to as the apparatus compressibility. The higher this value is, the greater the error will be between measured pore pressure and the real response of the material. Minimising apparatus compressibility is especially important during undrained shear when large excess pore pressures can be generated. Further work by Bishop (1973) presented a more complete derivation of the undrained pore-pressure ratio to include terms for the apparatus compressibility.

B-values measured for RGoM-EI specimens consolidated to 40 MPa were typically in the range of 0.5 - 0.6. It is known that the resedimentation procedure in the laboratory does produce fully saturated samples (Abdulhadi 2009), and so low values may also be attributed partly to the PVC membranes that have been used, which are thicker and have a higher stiffness than traditional latex membranes – though this effect is and to what degree it contributes to a lower B-value is difficult to quantify. Bishop also noted that convincing B-values for low compressibility porous materials are difficult to achieve. This means that this traditional measure of the specimen saturation becomes less meaningful at higher consolidation stresses (Casey and Germaine 2014).

5.4 Triaxial Consolidation

After having been normally consolidated to a vertical effective stress of 10 MPa in a consolidometer (see section 3.3.4) and unloaded to an OCR of 4, specimens were further consolidated inside the triaxial cell. It is imperative that samples are consolidated to at least twice the vertical effective stress reached during resedimentation in order to ameliorate the impacts of sample disturbance during extrusion. It is known that the effects of sample disturbance can be erased by imposing strain on a specimen (Schmertmann 1955). Additionally, further consolidation ensures that the specimen is in the normally consolidated region prior to shearing. This is of utmost importance for this research, as the stress state for a normally consolidated specimen must necessarily lie on the yield surface of the material prior to shearing.

Three different consolidation approaches were used in this research: hydrostatic consolidation, drained stress path consolidation, and K_0 consolidation.

Hydrostatic consolidation is the simplest of the three to undertake experimentally, as it only requires control of the cell pressure. During this process, all three principal stresses acting on the specimen are equal. In early tests, poor seating of the axial piston meant that hydrostatic conditions were reached inadvertently during a planned K_0 test.

In drained stress path consolidation, a desired stress state to be reached at the end of consolidation was entered into the control programme. The programme then brought the sample to that point monotonically while the drainage lines were left open to allow for drainage to occur. The target stress state was determined from the target vertical effective stress and an expected value of $K_{0.}$ The expected K_0 value was taken from databases of previous tests performed on RGoM-EI (Casey 2014; Fahy 2014). For both hydrostatic and drained stress path consolidation, as the sample height reduces, its area must necessarily change. Since the algorithms control the stresses applied, the area must be continually updated during consolidation. For consolidation, a right cylinder correction is applied to the original specimen area, A_0:

$$A_{cyl} = \frac{A_0(1-\varepsilon_v)}{(1-\varepsilon_a)} \tag{5-4}$$

The ability to implement K_0 conditions during consolidation is extremely important as this best replicates in situ conditions where there can be no lateral strain. By preventing lateral strain, the specimen is able to develop anisotropy as the platy shaped clay particles progressively orient perpendicular to the loading direction. A K_0 condition is achieved in this work through the use of volume feedback control. Axial deformations are measured directly with a string potentiometer, and radial deformations are then measured indirectly from measuring volume leaving the sample. The K_0 algorithm applied a constant axial deformation rate whilst the cell pressure is continuously adjusted to keep the radial strain close to zero. The advantage of this approach is that a continuous measurement of the K_0 value is captured, allowing observations into how this value changes during consolidation.

Other methods of implementing K_0 control involve the use of direct measurements of the specimen's lateral strain as opposed to volume control. Some examples include the use of laser displacement sensors to directly measure lateral deformation of the specimen (Ono 2002) or radial LVDT sensors which are in direct contact with the specimen surface.

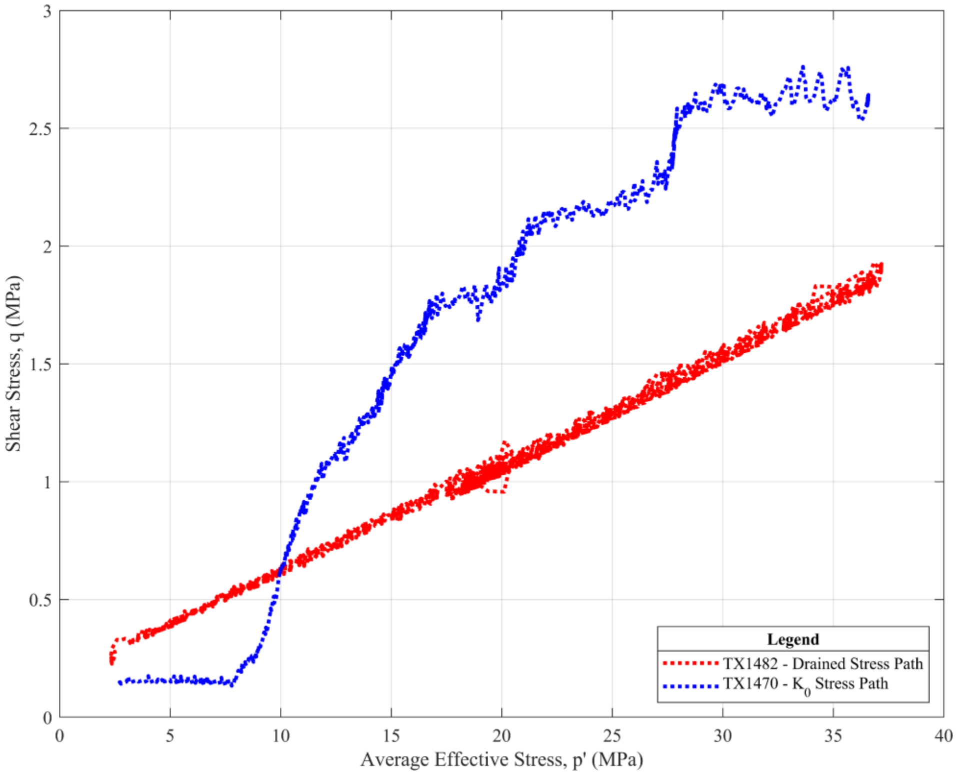

Figure 5-3 - Comparison of drained vs K_0 consolidation stress paths.

5.4.1 Evaluation of Consolidation Strain Rate

Due to the extremely low permeability of the test material and the high stresses employed in this research, a special focus was placed on the axial strain rate applied during consolidation. Initially a strain rate of 0.1 %/hr was proposed to be used within this research, in line with previous tests conducted on this material. Evaluation of excess pore pressures at the centre of the specimen using the linear theory developed by (Wissa et al. 1971) for CRS applications, found that this would lead to large errors in vertical effective stress at 40 MPa and higher. In contrast to RGoM-EI, higher permeability materials such as RBBC are able to be consolidated at 0.15 %/hr without the development of significant excess pore pressures (Casey 2014). In order to achieve a balance between test duration and the development of large excess pore pressure, an initial strain rate of 0.08 %/hr was selected for consolidation to approximately 20 MPa, with further consolidation being run at 0.02 %/hr. This fourfold reduction in strain rate would theoretically have an equal impact on the excess pore pressure at the centre of the sample. In Table 5-1 it can be seen that for a consolidation rate of 0.02 %/hr, the error in vertical effective stress is kept below 10 %.

The method described in (ASTM International 2020) D4186 standard was used to calculate the excess pore pressure developed in the middle of the sample during consolidation. This standard is developed for use with CRS devices but is still applicable here, and uses the aforementioned theories originally developed by Wissa et al. (1971). The excess pore pressure for CRS would be at the base of the device but is instead for a triaxial test at the specimen centre due to the presence of top and bottom drainage. Excess pore pressures at the centre of the specimen are calculated using the following equation:

$$\Delta u_c = \frac{r H_0 H \gamma_w}{2k} \tag{5-5}$$

Where:

H = Specimen height

H_0 = Original specimen height

k = Hydraulic conductivity

γ_w = Unit weight of water at 20°C

r = Strain rate

Assumptions made in this theory include:

1. Fully saturated soil samples
2. Incompressible soil particles and pore fluid
3. One dimensional drainage

4. One dimensional variation in stress
5. Flow through porous media obeys Darcy's law
6. Constant coefficient of volume compressibility (m_v)

These excess pore pressures represent initial transient conditions due to the motion of the piston. Once the excess pore pressure at the centre of the sample is calculated, one can calculate an average effective stress through the sample using the following formula:

$$\sigma'_{a,v} = \left(\sigma_v - \frac{2}{3} \cdot \Delta u_c\right) \tag{5-6}$$

Where:

$\sigma'_{a,v}$ = The effective average axial stress

The difference between this average axial effective stress and the theoretical consolidation effective stress yields an error, which can be used to evaluate whether the choice of strain rate is appropriate. If the error becomes too large, there would be a large difference between the amount of consolidation that has occurred at the ends compared to the middle of the sample. This would make the interpretation of meaningful results from the undrained shear data problematic. In Table 5-1 it can be seen theoretical values of this error for a consolidation strain rate of 0.02 %/hr. At this low strain rate, the error is kept to below 10 % even at 100 MPa consolidation stress. Figure 5-4 shows how by increasing the strain rate, you can dramatically increase this error.

The compression model used in the following analysis has the form:

$$\log \sigma'_{vc} = an + b \tag{5-7}$$

Where n = porosity and a & b are fitting parameters equal to -7.4 and 3.45 respectively (taken from the UT Geofluids database ("UT GeoFluids" n.d.)).

Table 5-1 - Average stress and error at the centre of a specimen that is consolidated at 0.02 %/hr.

Stress (MPa)	Strain (%)	Porosity, n	Specimen Height, H (m)	Hydraulic Conductivity (m/s)	Centre Pore Pressure, u (MPa)	Average Stress (MPa)	Error (%)
10	0.00%	0.331	8.10E-02	7.118E-13	0.63	9.58	-4.17
15	3.44%	0.307	7.82E-02	3.982E-13	1.08	14.28	-4.80
20	5.73%	0.290	7.64E-02	2.637E-13	1.59	18.94	-5.30
25	7.44%	0.277	7.50E-02	1.916E-13	2.15	23.57	-5.7
30	8.79%	0.267	7.39E-02	1.475E-13	2.75	28.17	-6.11
35	9.90%	0.258	7.30E-02	1.183E-13	3.39	32.74	-6.46
40	10.84%	0.250	7.22E-02	9.772E-14	4.06	37.29	-6.77
45	11.66%	0.243	7.16E-02	8.255E-14	4.76	41.82	-7.06
50	12.37%	0.237	7.10E-02	7.098E-14	5.50	46.34	-7.33
55	13.01%	0.231	7.05E-02	6.192E-14	6.25	50.83	-7.58
60	13.58%	0.226	7.00E-02	5.467E-14	7.04	55.31	-7.82
65	14.11%	0.221	6.96E-02	4.875E-14	7.84	59.77	-8.04
70	14.58%	0.217	6.92E-02	4.384E-14	8.67	64.22	-8.26
75	15.02%	0.213	6.88E-02	3.971E-14	9.53	68.65	-8.47
80	15.43%	0.209	6.85E-02	3.620E-14	10.40	73.07	-8.67
85	15.81%	0.205	6.82E-02	3.319E-14	11.29	77.47	-8.86
90	16.16%	0.202	6.79E-02	3.058E-14	12.20	81.86	-9.04
95	16.49%	0.199	6.76E-02	2.830E-14	13.13	86.24	-9.22
100	16.81%	0.196	6.74E-02	2.630E-14	14.08	90.61	-9.39

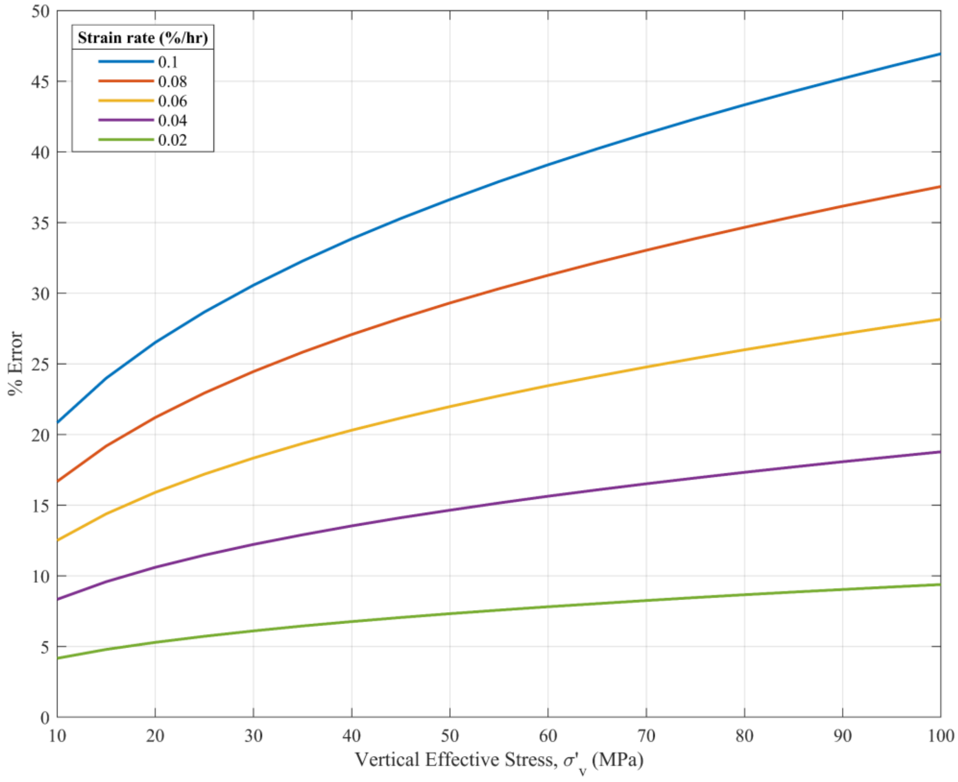

Figure 5-4 - Impact of strain rate on the error between theoretical axial effective stress and actual axial effective stress at the centre of the specimen.

5.5 Secondary Compression

Once the clay specimen had reached its target stress state, the triaxial control programme entered the Hold Stress algorithm in order to maintain this stress state. The end of consolidation stress state was held for a minimum duration equal to one log cycle of secondary compression (usually around 24 hours).

The effect of secondary compression (strain under constant vertical effective stress) is to continue densifying the clay. This in turn expands the yield surface envelope. Hence, as the yield surface of the material is expanding but the stress state is remaining constant, the material is becoming overconsolidated due to the effects of secondary compression. This process meant that it was important to be consistent between tests in how much time was allowed for secondary compression, as this was affecting the location of the material yield surface.

5.6 Undrained Shear

Deposits of saturated clay are frequently loaded or unloaded very quickly relative to the rate at which excess pore pressures can dissipate from the material. In these conditions, the clay is said to be in an ‘undrained’ state where its volume and water content remain constant. Geotechnical engineers commonly employ undrained shear tests to calculate strength properties whilst in the undrained condition. These strength properties, such as undrained shear strength, can then be used in $\varphi = 0$ total stress analyses. In this research undrained shear tests are used as the effective stress path traces the shape of the yield surface, as explained in detail in section 2.6.

The final step before commencing undrained shearing was to perform a leak check. This involved closing both drainage valves and monitoring the pore pressure response – in the case of no leaks the pore pressure should remain constant within the sample. External leaks could be fixed prior to shearing whilst internal leaks would lead to an aborted test. In real tests, some amount of leakage is inevitable. Therefore, a criterion for the acceptable amount of leakage must be created which is a function of the soil type, test type and duration of test (Leroueil et al. 1988). In this work an increase in the pore pressure of more than 0.1 ksc with the valves closed would have led to an aborted test due to an internal leak. External leaks would have been fixed in the backpressure saturation stage using methods described in section 5.3.

Once it had been confirmed that there were no leaks in the system, undrained shearing could commence. For undrained shear an axial strain rate of 0.5 %/hr was selected, consistent with other studies using RGoM-EI (Casey 2014; Hanley 2017). Shearing was run until critical state conditions were reached in the specimen.

In contrast to the right cylindrical area correction applied during consolidation, a parabolic area correction was applied by the triaxial control algorithm during undrained shearing in compression. The exact form of the equation is (Germaine and Ladd 1988):

$$A_{par} = A_0 \left\{ -0.25 + \frac{\sqrt{25 - 20\varepsilon_a - 5\varepsilon_a^2}}{4(1 - \varepsilon_a)} \right\}^2 \qquad (5\text{-}8)$$

For undrained shearing in extension, a right cylinder area correction was applied instead.

Mechanically there are two classes of undrained stress changes that lead to failure in a specimen (Bishop and Wesley 1975). There can be tests where the cell pressure is held constant and the axial stress is either increased or decreased until failure, or there are tests where the axial stress is held constant, and it is the cell pressure that is varied.

In both scenarios, the effective stress paths are almost identical despite having very different total stress paths (Figure 5-5). For tests in this research, it was the axial stress that was varied on the specimens whilst the cell pressure was kept constant.

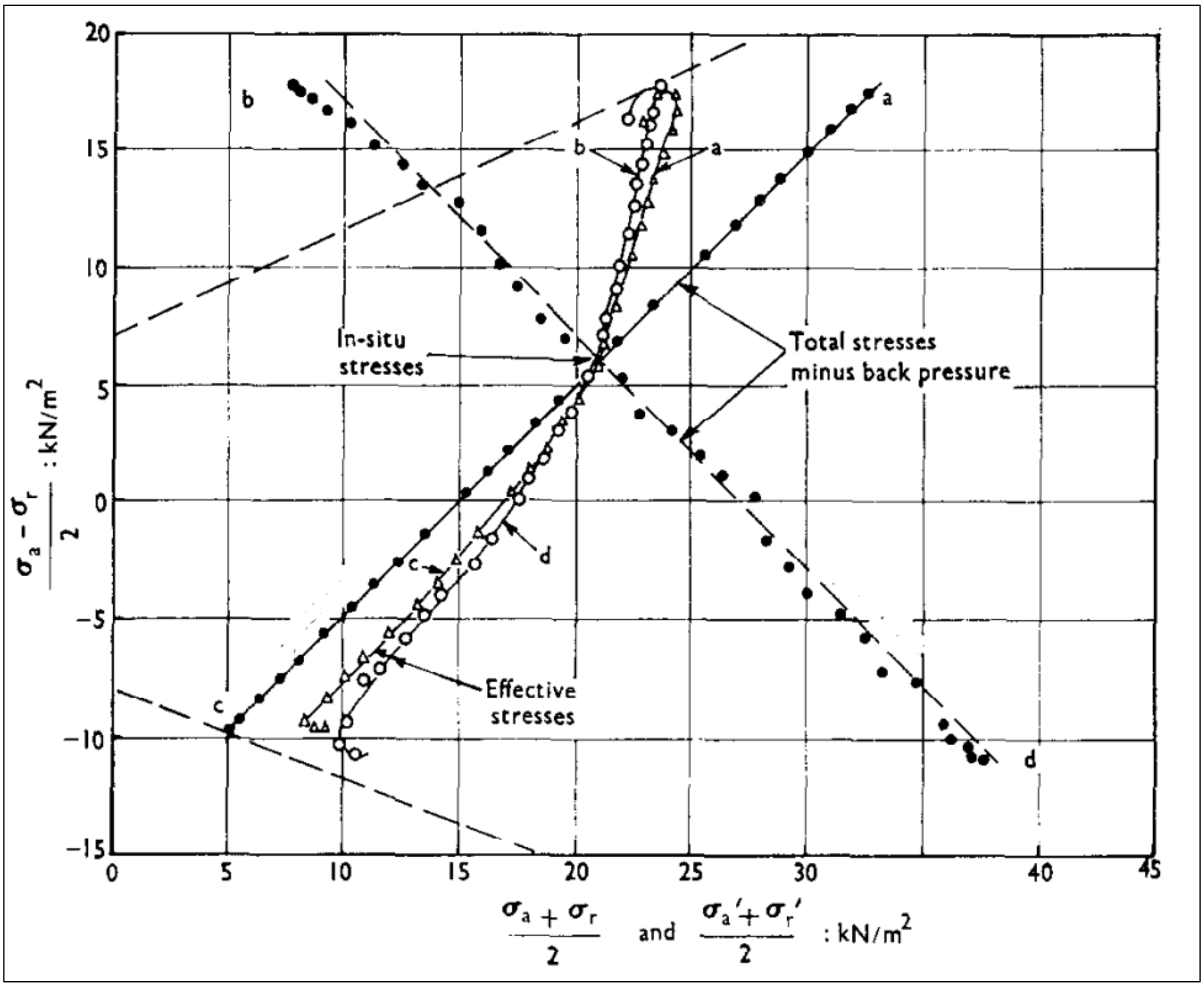

Figure 5-5 - Figure from (Bishop and Wesley 1975). *Almost identical effective stress paths are shown despite radically different total stress paths applied to the specimens in compression and extension.*

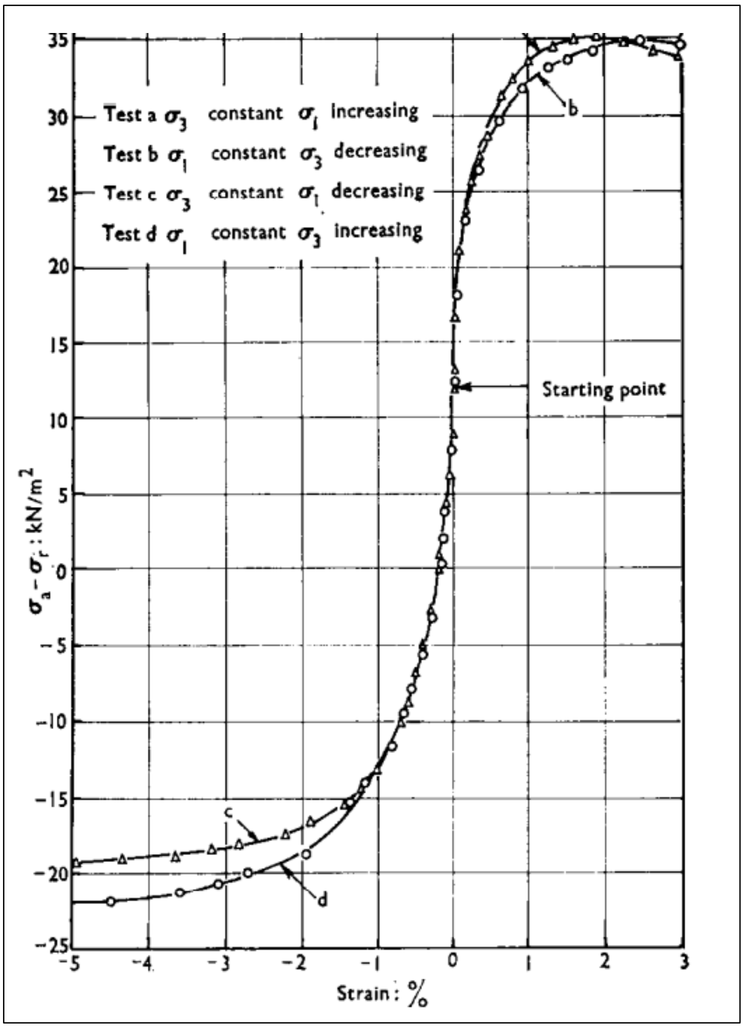

Figure 5-6 – Figure from (Bishop and Wesley 1975). Similar stress strain paths are shown for two different types of undrained stress change in both compression and extension.

5.6.1 Skempton's A Parameter

Skempton (1954) developed what is known as the A parameter by considering stress changes on a saturated (i.e., the B value = 1) soil which has a skeleton that behaves as a perfectly elastic and isotropic material. In this case, pore pressure changes can be related to changes in total stress in the undrained condition with the following equation:

$$\Delta u = \frac{1}{3}(\Delta\sigma_1 + \Delta\sigma_2 + \Delta\sigma_3) \tag{5-9}$$

For the case of triaxial compression $\Delta\sigma_2 = \Delta\sigma_3$ and thus equation 5-9 reduces to:

$$\Delta u = \Delta\sigma_3 + \frac{1}{3}(\Delta\sigma_1 - \Delta\sigma_3) \tag{5-10}$$

And similarly, for triaxial extension where $\Delta\sigma_2 = \Delta\sigma_1$:

$$\Delta u = \Delta\sigma_3 + \frac{2}{3}(\Delta\sigma_1 - \Delta\sigma_3) \tag{5-11}$$

Skempton replaced the constants in front of the $\Delta\sigma_1 - \Delta\sigma_3$ term by the so called 'A' parameter to account for plastic behaviour:

$$\Delta u = \Delta\sigma_3 + A(\Delta\sigma_1 - \Delta\sigma_3) \tag{5-12}$$

By inspecting equations 5-10 and 5-11, it is clear that in the elastic case during undrained shear, pore pressures generated during extension should be twice that of compression. It is also worth noting that for the case of isotropic loading, the difference in principal stress increments $\Delta\sigma_1 - \Delta\sigma_3$ must equal zero, and hence the A parameter becomes zero. The A parameter is therefore able to provide information on the direction of the effective stress path, as well as to what extent changes in the deviator stress contribute to changes in pore pressure.

The A parameter is influenced by a range of factors such as the mode of loading, stress level and degree of anisotropy within a given soil. Peak values of A_f (A parameter at failure) have been shown to occur at 30-60° inclination, where inclination is the angle between the consolidation and major principal stress directions (Kurukulasuriya et al. 1999). Overconsolidated clays, which tend to dilate upon shearing, present negative values of the A parameter. Normally consolidated clays, in contrast, tend toward a value of +1 upon shearing.

Typical values of the A parameter at failure can be seen in Table 5-2.

Table 5-2 - A parameter values at failure for different soil type (Das 2019).

Value of the A parameter at failure	
Soil type	**A_f**
Clay with high sensitivity	0.75 - 1.5
Normally consolidated clay	0.5 - 1
Overconsolidated clay	-0.5 - 0
Compacted sandy clay	0.5 - 0.75

5.7 Disassembly

After the triaxial test has completed, the specimen must be removed from the triaxial cell and post-shear measurements of the specimen taken. First the cell pressure and axial stress are reduced in tandem, so as to not place an excessive shear on the sample. Once at atmospheric conditions are reached, silicone oil is drained from the cell. The cell is then disconnected from its transducers and removed from the load frame.

If an O-ring has been used in the top cap, the vacuum in the suction cap is first released and then a positive pressure is applied. This positive pressure aids the release of the top cap from the suction cap. If necessary, a positive pressure can also be applied to the vacuum line and the piston manually moved to dynamically break the seal with the O-ring. After the specimen has been removed, the PVC membrane is carefully removed using a retractable blade knife. The specimen mass is then measured, photographed, and placed into an oven for drying. Often it is sufficient for test specimens to be oven dried for just 24 hours at 105 °C, however for RGoM-EI this process can take several days as it is an extremely fine-grained material. Specimens were dried in the oven for 1 week, before measuring the mass. They were subsequently placed back into the oven for another week and their 1 week and 2 week masses compared to ensure they were sufficiently dry.

The final step of a triaxial test involved removing salt water from the drainage lines. Pressurised air was used to expel salt water from the network of pipes and ensure there were no blockages in the system. Failure to do so could result in tubes blocking due to water evaporating and dissolved salts being left behind. The stainless-steel tubes are 1/8” diameter by design, so that the effects of apparatus compressibility can be minimised – this however necessitates increased levels of maintenance.

In addition, a Branson 1200 B1200R-4 ultrasonic cleaner was used in the laboratory to sonicate the porous stones. This removes clay particles from the stones, which build up in the pores over time and reduce their effectiveness.

6 Presentation of Experimental Results

6.1 Testing Summary

Of the 9 high pressure triaxial tests attempted, 3 were aborted due to equipment failures. This failure rate is broadly in line with the one other researcher to have used this equipment (Casey 2014), and is in part a reflection of the lack of well tested methods for this relatively new triaxial cell. Sources of failures during previous research were predominantly due to internal leaks. Switching from a system of double latex membranes sealed with O-rings to one with a single layer of heat shrink PVC tubing appears to have largely eliminated this issue. Failures during this body of work instead occurred primarily due to problems with O-rings. O-rings inside the drainage valves had degraded due to the corrosive saltwater environment, resulting in a lack of excess pore pressure generation during shearing. An O-ring also failed inside the axial PVA again leading to a test failure. An additional mechanical failure arose from a DC motor failure caused by commutator wear.

Table 6-1 - Summary of triaxial tests conducted in this research.

Research #	**TX #**	**RS #**	**Consolidation Stress (MPa)**	**Consolidation & Shear mode**
1	-	-	40	Test aborted
2	TX1453	650	40	K0
3	TX1457	657	40	Test aborted
4	TX1470	656	40	K_0 – Undrained shear compression
5	TX1472	660	40	Hydrostatic – Undrained shear compression
6	TX1476	659	40	Hydrostatic (K_0 attempted) – Undrained shear extension and compression
7	TX1482	669	40	Drained stress path to K = 0.9 - Undrained shear extension then compression
8	TX1493	668	80	K_0 - Undrained shear compression – Test aborted
9	TX1498	685	40	Drained stress path to K = 0.9 - Undrained shear compression then extension

Table 6-2 - Summary of triaxial shear results

	Initial		**End of cons.**		**At peak shear**	
TX #	ω (%)	e_0	$\sigma'_{v,max}$ (MPa)	B-value	ε_f (%)	S_u (MPa)
TX1470	18.0	0.498	39.23	0.54	14.47	3.60
TX1472	19.4	0.538	39.17	0.39	8.24	7.16
TX1476	19.2	0.532	39.57	0.54	-7.95	-6.90
TX1482	18.3	0.508	39.10	0.52	-10.58	-5.88
TX1493	18.8	0.520	76.72	-	-	-
TX1498	19.2	0.533	38.92	0.32	5.24	7.31

6.2 Consolidation Data

Figure 6-1 presents the compression data of some of the tests performed in this research. Results are presented on a void ratio vs log vertical effective stress plot. Included within this plot is the consolidation data from some earlier tests undertaken in the research, TX1470 and TX1472. TX1472 shows some unloading occurring during the consolidation process. This appears to have been caused by the axial DC motor not actuating at low voltage due to commutator wear. As the specimen unloaded, the voltage being supplied to the motor would have gradually increased due to the increasing error, until eventually the axial motor began to turn again. TX1470 was consolidated at a rate of 0.08 %/hr for the entire duration of the test, whereas the subsequent protocol became to reduce the rate of consolidation to 0.02 %/hr from a vertical effective stress of approximately 20 MPa. The reasoning behind this change has been explained in detail in section 5.4.1. The impact of changing the consolidation strain rate from 0.08 %/hr to 0.02 %/hr can be seen more clearly in Figure 6-2.

Measurements of lateral stress ratio are taken continuously during consolidation, enabling trends in this value to be seen with stress level. Lateral stress ratio data from this work is presented in Figure 6-3 against the vertical effective stress. Early tests encountered issues with volume control during testing due to leaks within the triaxial system. These leaks led to inaccurate values for the lateral stress ratio gathered during consolidation and as such these data have been excluded from the graph. TX1482 and TX1498 were consolidated along drained stress paths, with the control algorithm fixed to reach a lateral stress ratio of 0.9 at 40 MPa vertical effective stress. TX1470 and TX1493 were consolidated using K_0 control. The data from TX1493 appears very promising initially, with a reduction in stress ratio from isotropic conditions (the stress state of the specimen is approximately isotropic prior to consolidating inside the triaxial cell). The value of the stress ratio then begins to climb with increasing stress level, in line with findings from Casey (2014). Unfortunately, at approximately 40 MPa, the axial DC motor stopped turning. This led to relaxation within the specimen, until it began actuating again at too high a rate. This effectively sheared the sample and led to an aborted test.

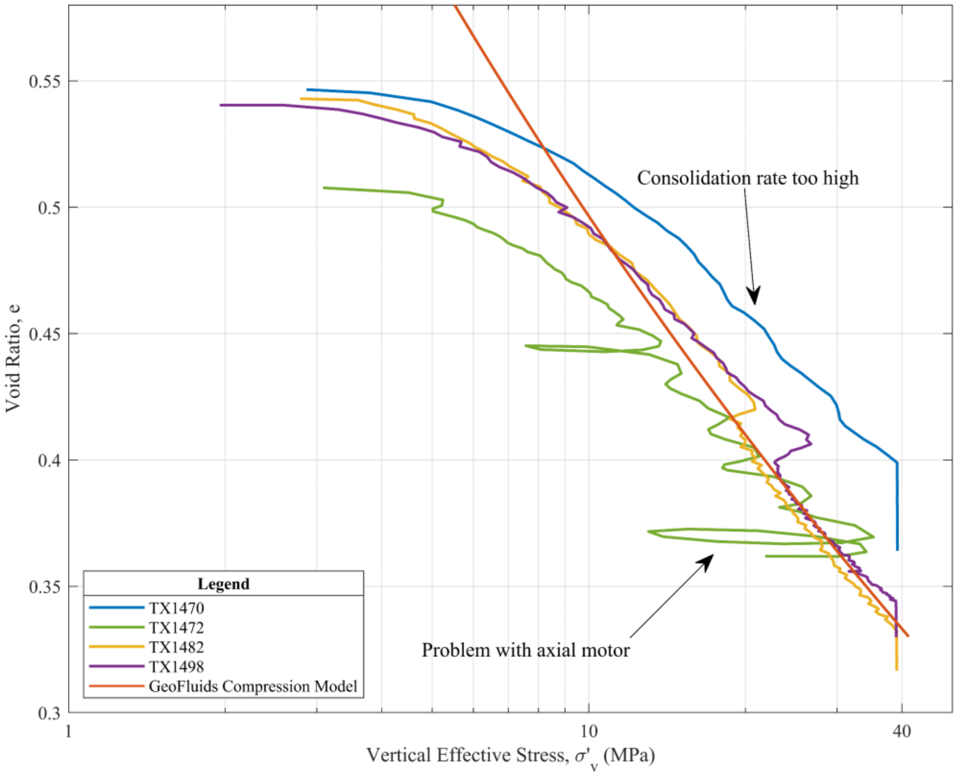

Figure 6-1 – Comparison of virgin compression curves from tests on RGoM-EI

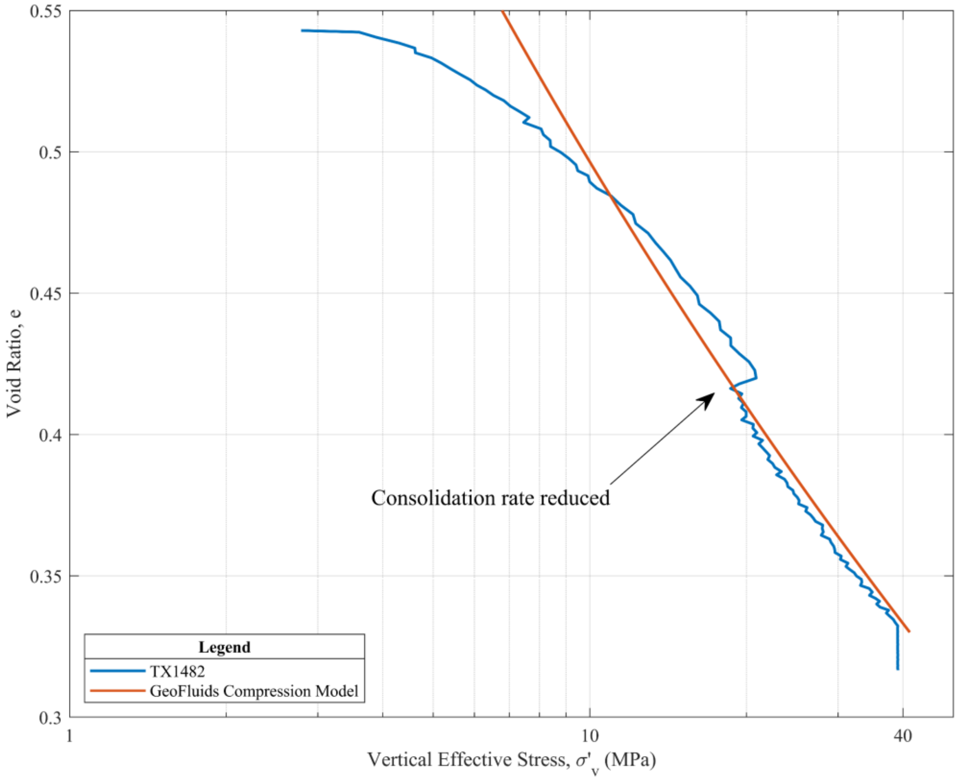

Figure 6-2 - Consolidation data for TX1482. Consolidation rate was reduced from 0.08 %/hr to 0.02 %/hr at approximately 20 MPa.

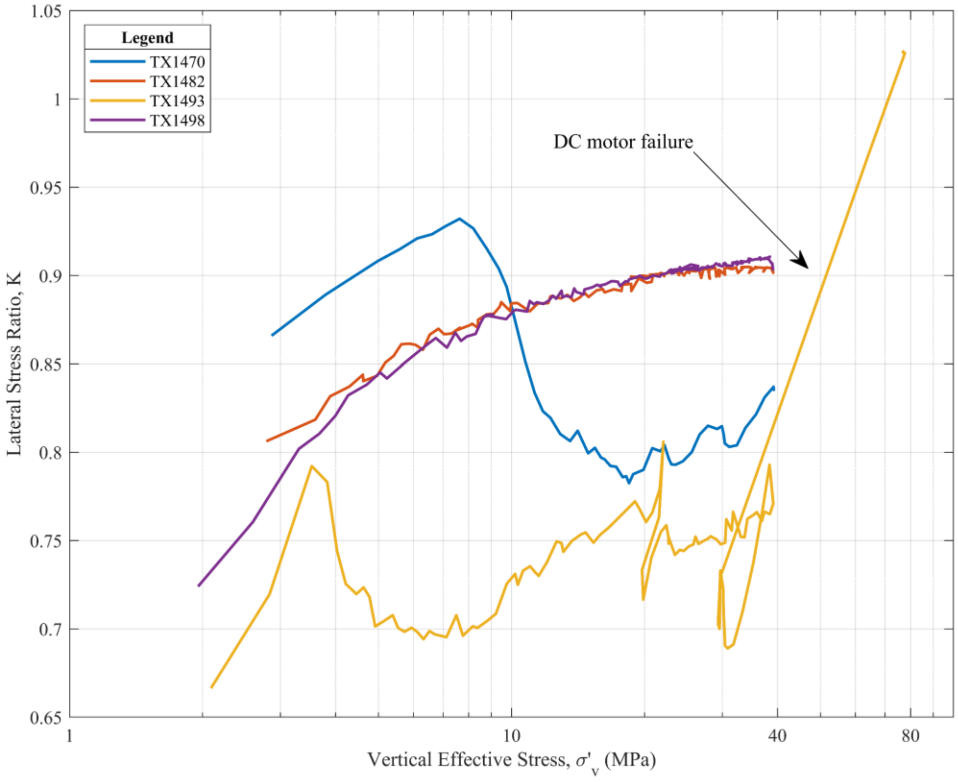

Figure 6-3 - Lateral stress ratio vs vertical effective stress measured during consolidation within the high pressure triaxial cell.

6.3 Undrained Shear

This section presents the undrained shear results. Shearing was undertaken until $\varepsilon_a > 10\ \%$ to ensure that critical state conditions had been reached within the sample.

Figure 6-4 presents a plot of normalised shear stress vs axial strain for four tests. Two of the tests, TX1482 and TX1498 were consolidated to a lateral stress ratio of 0.9, with TX1472 and TX1476 being isotropically consolidated. The shear stress has been normalised against the maximum vertical effective stress, which was approximately 40 MPa for all four of these tests.

In Figure 6-5 a plot of normalised shear induced pore pressure vs axial strain can be seen for the same four tests. In this figure, shear reversal, where the direction of undrained shearing was reversed, can clearly be seen in TX1476, TX1482 and TX1498.

Figure 6-8 shows the effective stress paths of these tests in MIT p-q space with axes normalised to the maximum consolidation stress.

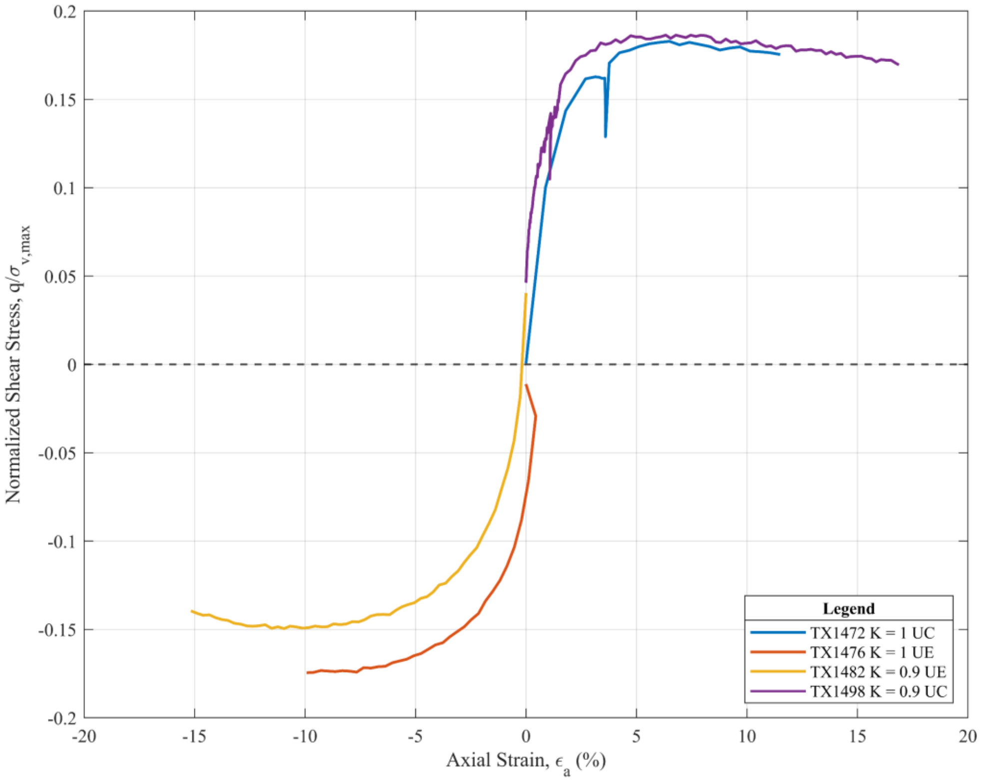

Figure 6-4 - Normalised shear stress vs axial strain for four triaxial tests consolidated to 40 MPa with either hydrostatic or drained stress path consolidation histories.

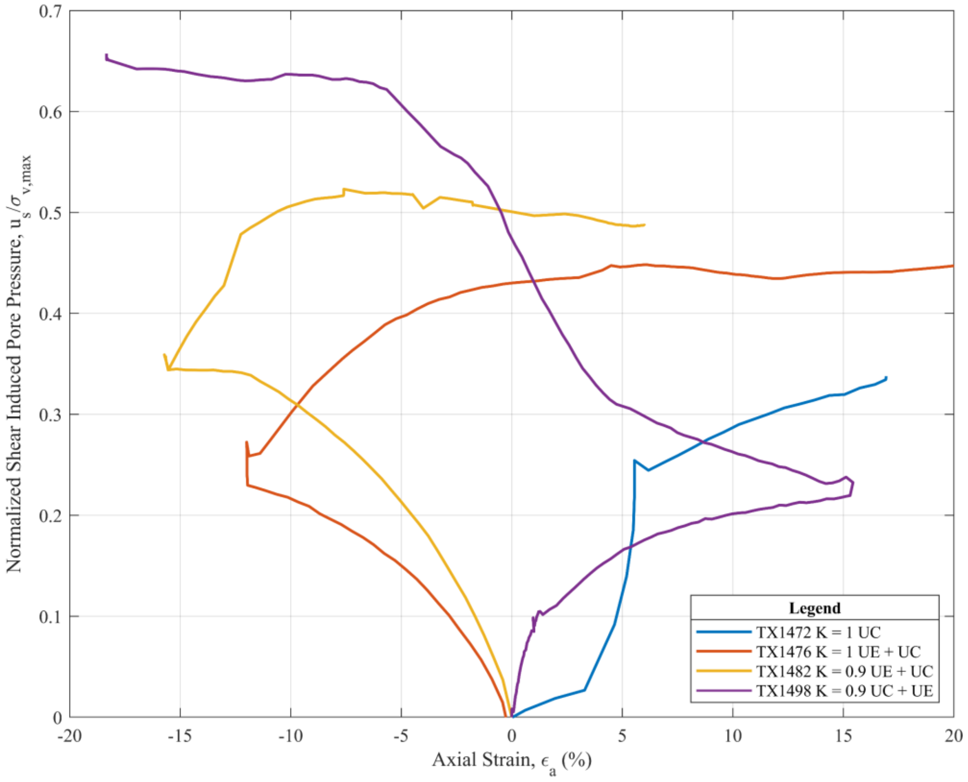

Figure 6-5 - Graph showing normalised shear induced pore pressure vs axial strain for four RGoM-EI undrained shear tests consolidated to 40 MPa.

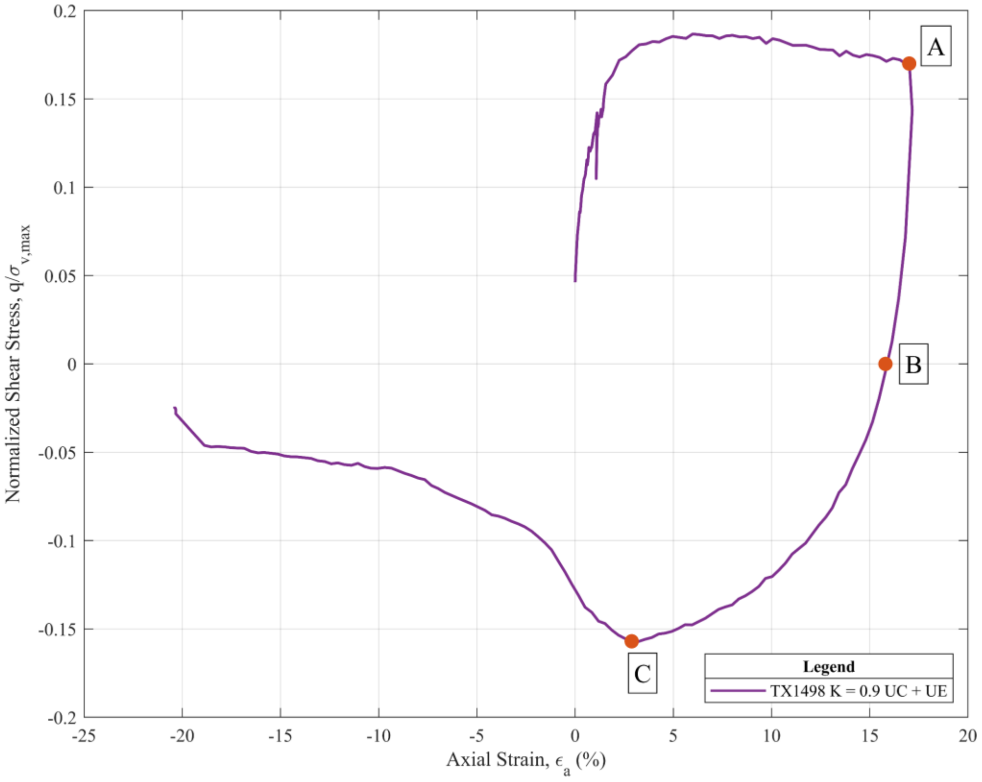

Figure 6-6 - Normalised shear stress vs axial strain from TX1498. Point A is at the beginning of triaxial extension, point B represents when there is zero shear stress during extension and point C is at the point of maximum shear stress in extension.

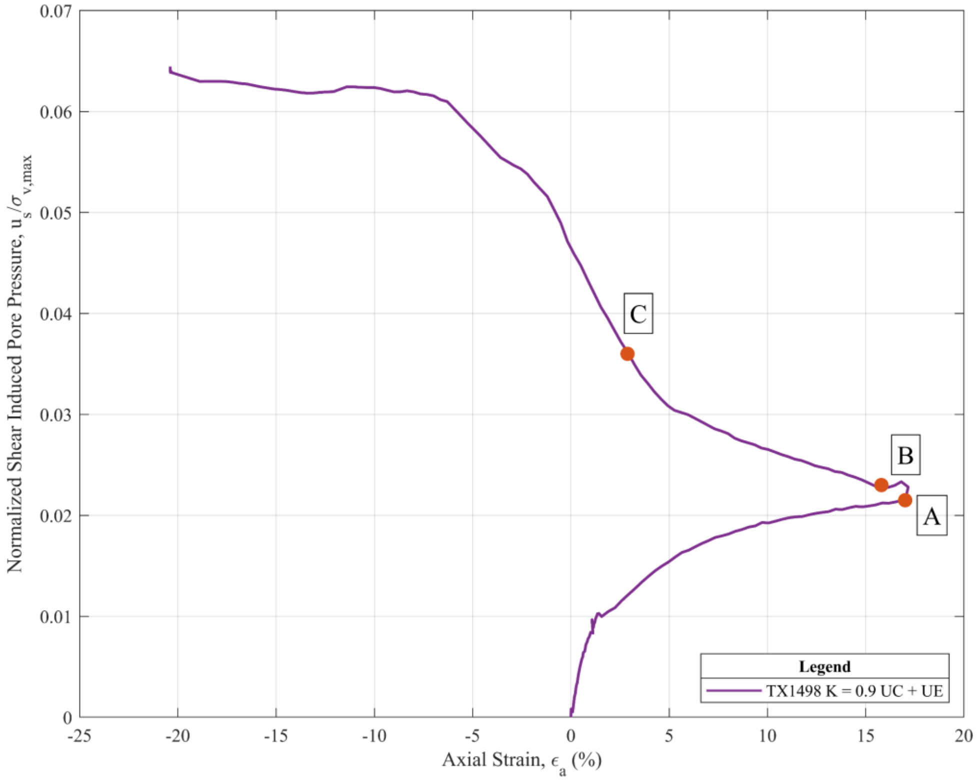

Figure 6-7 - Normalised shear induced pore pressure vs axial strain from TX1498. Points A, B and C are as described in Figure 6-6.

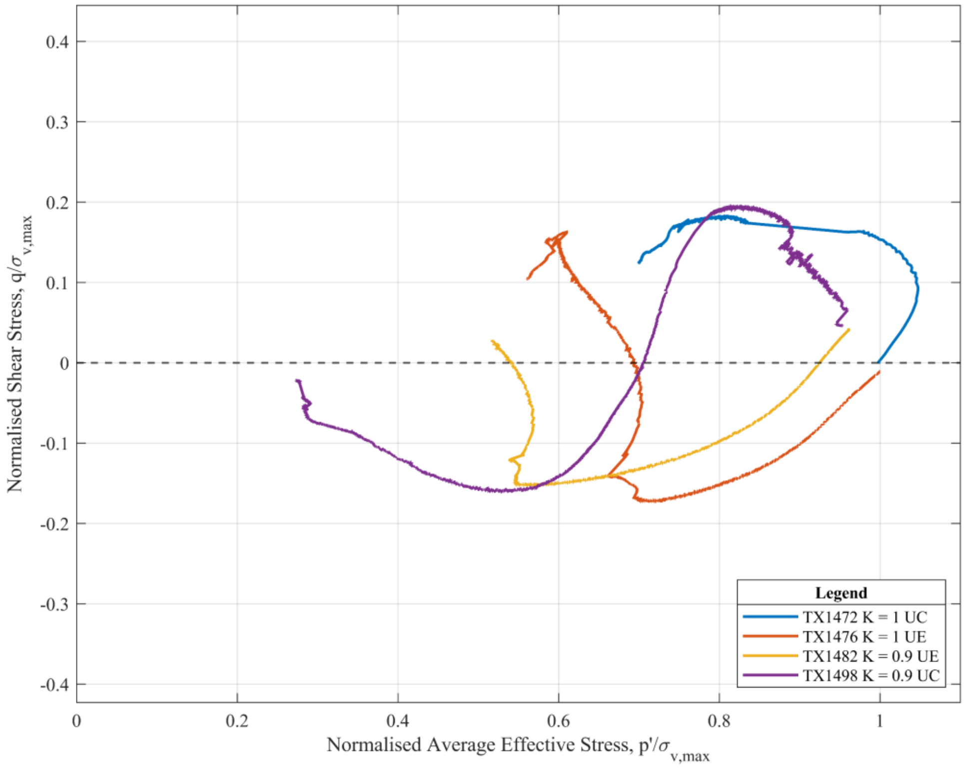

Figure 6-8 - Undrained shear stress paths shown in normalised p-q space for RGoM-EI samples consolidated to 40 MPa. Two of the specimens were isotropically consolidated, with two consolidated to a lateral stress ratio of 0.9.

6.4 Comparisons and Interpretations

6.4.1 Consolidation Behaviour

RGoM-EI, being a high plasticity soil, experiences a very high degree of compressibility as the specimen consolidates. This behaviour can be seen in Figure 3-4 which shows a plot of the one-dimensional consolidation behaviour for this material.

In Figure 6-9 the variation of $\mathrm{K}_{0\mathrm{NC}}$ with vertical effective stress is shown for three different resedimented materials. It can be seen that for low liquid limit, silty materials such as RPC, there is relative insensitivity to stress level. For materials such as RGoM-EI, with a much higher liquid limit and smectite rich mineralogy, K_{0NC} increases sharply with increasing stress level. These data, from Casey et al. (2016), reflect consolidation data gathered in this research which shows K_0 initially reducing (due to initially hydrostatic conditions in the triaxial cell) before increasing as the vertical effective stress is increased.

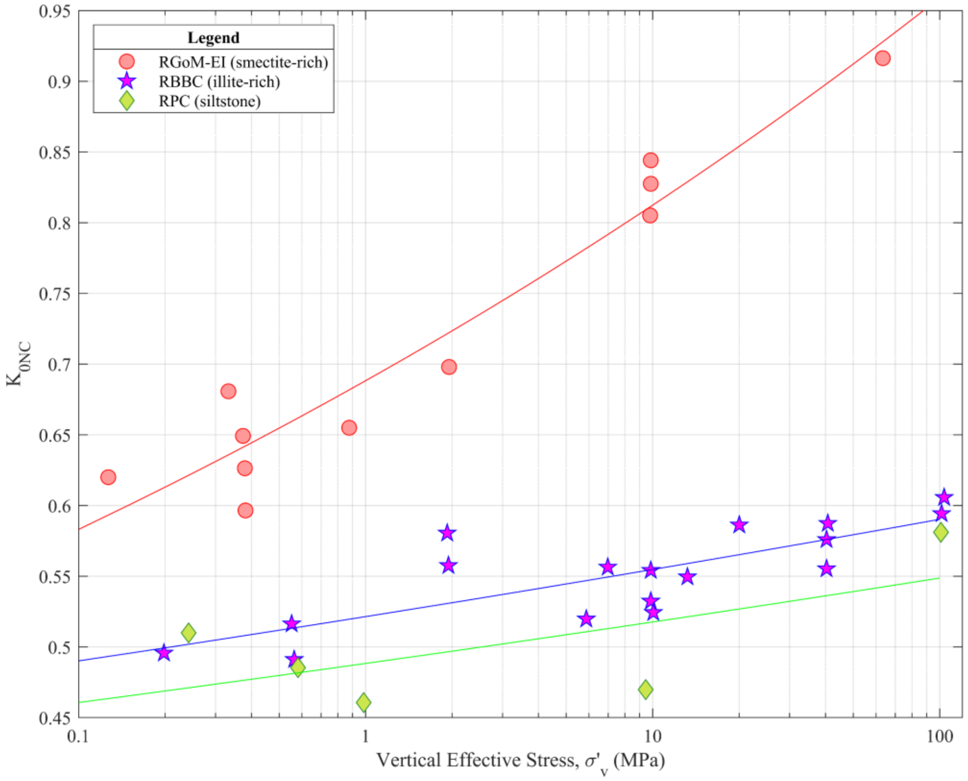

Figure 6-9 - Graph showing variation in K_{0NC} *vs vertical effective stress for three resedimented clays. Power trendlines have been fitted through the data points. Figure has been reproduced using data from* Casey et al. (2016).

As discussed in the previous section, none of the tests in this program were successful at Ko consolidation. Two tests were performed using a drained stress path to a prescribed K value of 0.9 at the target stress of 40 MPa. The effectiveness of this assumption can be evaluated by plotting axial strain vs volumetric strain during consolidation. If K_0 conditions are observed, axial strain should match the volumetric strain. Therefore, deviations from this represent a departure from K_0 conditions and indicate that some lateral straining has occurred. In Figure 6-10 the axial vs volumetric strain is plotted for the two tests consolidated along drained stress paths to a lateral stress ratio of 0.9. For both tests, the volumetric strain is ~15 % at the end of the consolidation vs ~10 % axial strain. This tells us that the true K_0 value is either above or below .

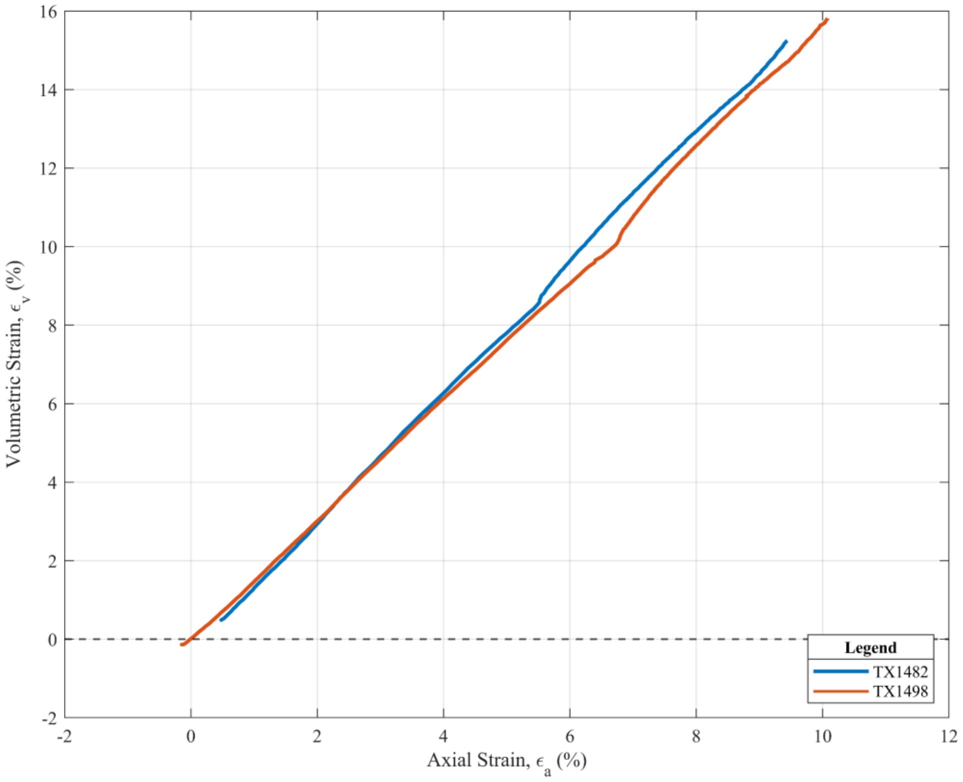

Figure 6-10 - Variation of volumetric strain with axial strain during consolidation for two tests consolidated along drained stress paths to K = 0.9.

6.4.2 Stress Strain

For the two triaxial compression results, they can be seen to both follow similar paths with a similar magnitude in peak shear stress, before a strain localization forms in the sample and shear stress reduces. In triaxial extension, the hydrostatically consolidated specimen sustains 16 % more shear stress than the sample that was consolidated along a drained stress path. Additionally, a more ductile response can be seen in the material during extension, with peak stress being reached after 10 % axial strain. This is in contrast with the compression data, which both show peaks after approximately 5 % strain.

6.4.3 Undrained Shear

The pore pressure response during undrained shear is comprised of two components, a component due to shear stress, u_s, and a component due to the octahedral stress, u_{oct}. Changes in octahedral stress on a saturated specimen with a B-value equal to 1 would theoretically lead to an equal change in pore pressure, Δu, and hence no change in effective stress. Therefore, shear induced pore pressures are typically of most interest when analysing triaxial data. Table 6-2 shows that B-values measured within this work were around 0.5, and so changes in octahedral stress would lead to a lower amount of pore pressure increase. Shear induced pore pressures can be calculated with the following equation:

$$\Delta u_s = \Delta u - \Delta\sigma_{oct} \tag{6-1}$$

Shear failure occurs when the shear strength of the material is less than the applied load.

At the end of consolidation, the mudrock is on the tip of the yield surface. Secondary compression then acts to move the yield surface away from the pre-shear stress state. This effectively begins to overconsolidate the material, but not through unloading of the soil. This effect is expected to be small for RGoM-EI however, as pore pressures generated at the end of consolidation are unlikely to be dissipated.

A photo of the specimen from TX1470 can be seen in Figure 6-11. Here a cone of material has sheared away from the main body of the specimen. This is due to the formation of a ‘dead zone’ in the specimen which can form due to the presence of radial restraint at the specimen ends from the rough, porous stones; in Figure 6-14 an idealization of the aforementioned ‘dead zones’ can also be seen. This end restraint causes strain non-uniformities to occur through the soil specimen and complicates the stress state, as it then varies with distance from the ends. The radial restraint increases the radial stress at the ends during compression, as the tendency for the specimen to expand laterally due to the Poisson’s effect is prevented. The centre of the specimen, free to expand laterally, is largely unaffected from effects due to the type of restraint applied at the ends of the specimen. This issue of specimen non-uniformity has been studied extensively (Sheahan 1991) with a range of solutions proposed that aim to reduce the friction between the porous stone and the specimen. Other solutions also include end caps that deform radially in response to increasing axial stress on the specimen. All of these solutions do inevitably increase the complexity of the testing equipment, however.

The TX1470 specimen was also consolidated at a relatively high consolidation rate of 0.08 %/hr, which may have led to larger excess pore pressures at the centre of the specimen which had not had sufficient time to dissipate during consolidation. The impact of strain rate on the generation of excess pore pressures can be dramatic for such a fine-grained material as RGoM-EI, something which is quantified in section 5.4.1.

The bulging seen on the side of Figure 6-11 is characteristic of mudrocks consolidated to stresses above 30 MPa. It is worth noting however that diagenetic effects, such as cementation and recrystallization would cause a more brittle in situ behaviour when compared to resedimented laboratory specimens (Nygård et al. 2006).

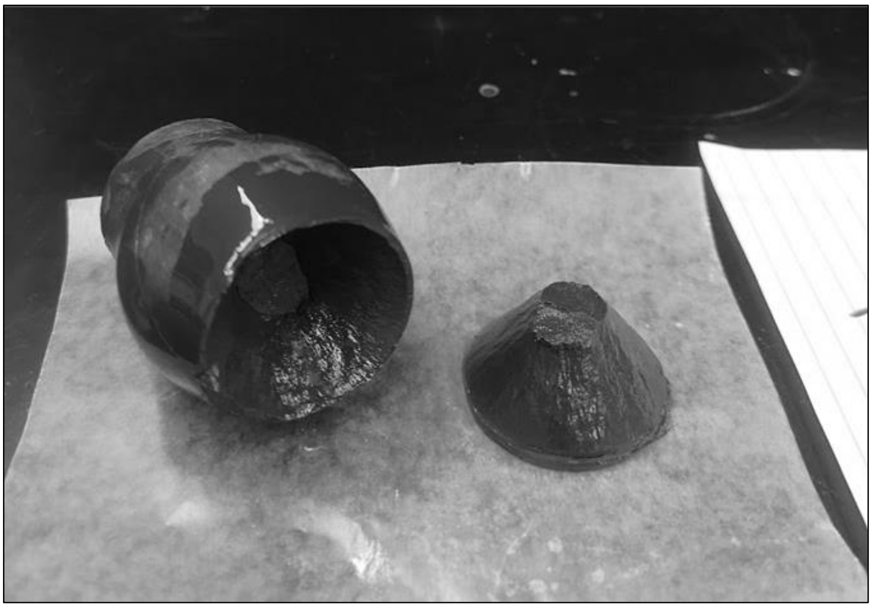

Figure 6-11 - Image showing specimen from triaxial test TX1470. The specimen has bulged significantly at the centre and a cone of material has sheared away.

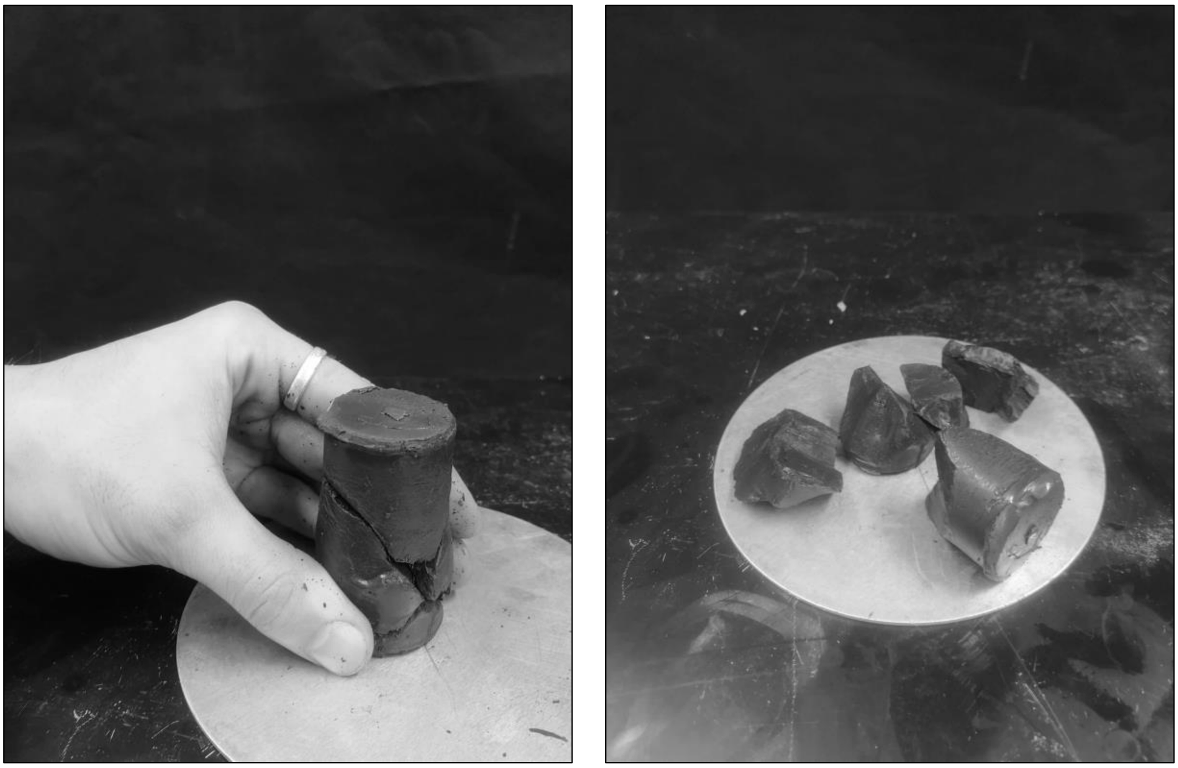

Figure 6-12 – Two images showing specimen from triaxial test TX1476. The specimen was run first in triaxial extension, and then in triaxial compression.

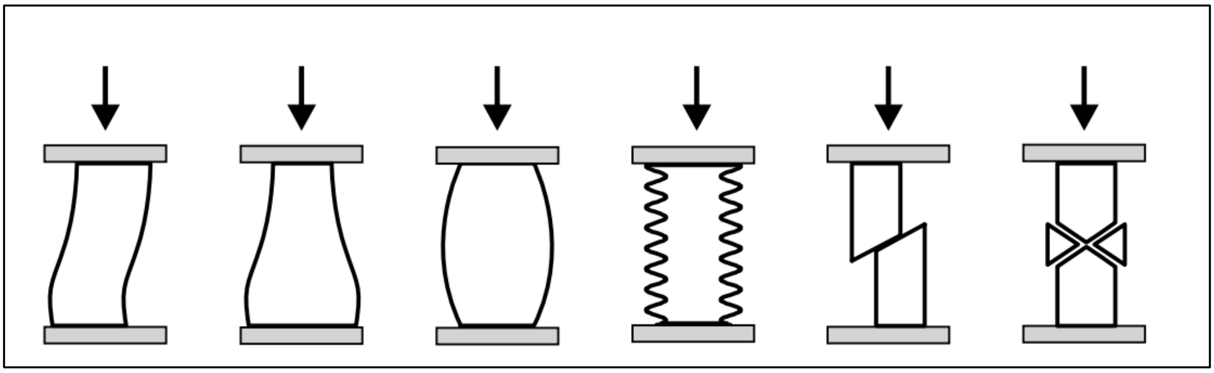

Figure 6-13 - Figure taken from (Bigoni 2012) *showing different general failure modes during compression. From left to right these are Euler mode, bulging, barrelling, surface instability, asymmetric shear banding, symmetric shear banding.*

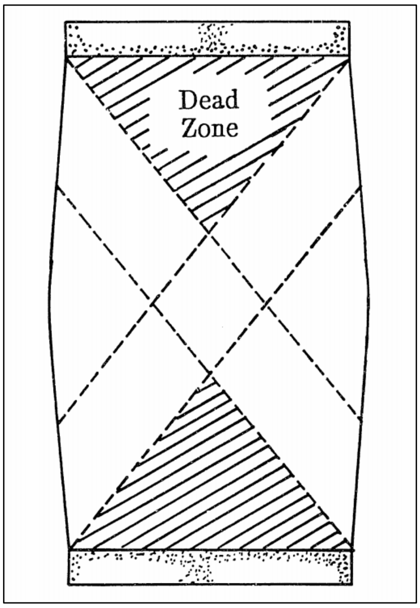

Figure 6-14 - Image showing location of conic 'dead zones' inside a typical triaxial specimen. Image taken from (Sheahan 1991).

6.4.4 Triaxial Compression

Triaxial compression is the most common of the two triaxial undrained shear tests within the geotechnical practice. In these tests, the major principal stress is the vertical effective stress. This is increased at a constant rate whilst the minor principal stress remains constant.

6.4.5 Triaxial Extension

Triaxial extension, where the lateral horizontal effective stress is also the major principal stress, occurs frequently in geotechnical settings. It is of interest to geomechanical engineers, who study the effects of geologic phenomena on pore pressures developed inside mudrocks. In accretionary prisms for example, material that was initially deposited in K_0 conditions can see the horizontal effective stress become larger than the vertical effective stress.

(Abdulhadi 2009) has suggested that even common research materials, such as Boston Blue Clay, have a distinct lack of undrained extension test data. This gap in the availability of data in this mode of shearing hampers the ability to fully understand and decipher trends in soil behaviour.

The material is clearly able to withstand a lower shear stress in triaxial extension when compared to triaxial compression (Figure 6-4). Mechanisms behind this may be due to the fact the sample was uniaxially consolidated to 10 MPa, and this causes an orientation of the clay particles which develops an inherent anisotropy within the fabric of the clay. The Hydrostatic compression after this does not erase this anisotropy as it is only ~10 % strain. Another mechanism may be the role of the intermediate principal stress. In extension, the relative intermediate principal stress changes from a value of 0 to 1. The relative intermediate principal stress is defined by the ratio:

$$b = \frac{\sigma_2 - \sigma_3}{\sigma_1 - \sigma_3} \qquad (6\text{-}2)$$

The impact of b for different shearing devices can be seen below in Figure 6-15, where δ represents the angle between the consolidation direction and the principal stress direction.

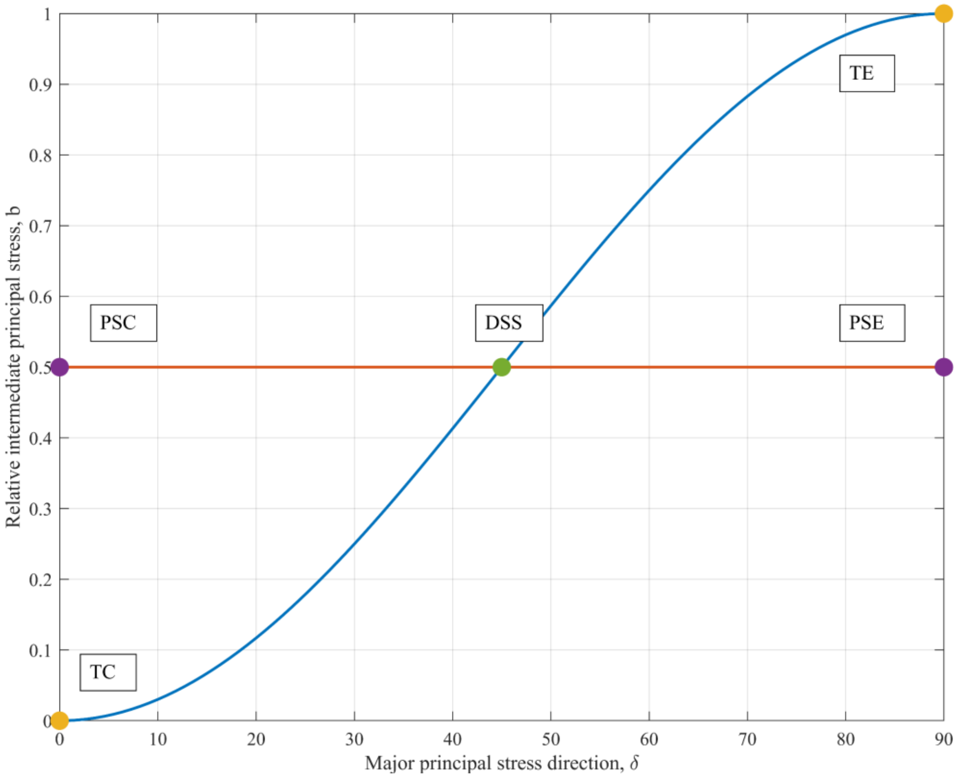

Figure 6-15- Graph showing the influence of the intermediate principal stress in different shear devices (from Germaine (1982)).

6.4.6 Shear Reversal

Tests were conducted that saw one mode of shearing initially, before the major principal stress direction was reversed and the opposite shearing mode ran. Plots of normalised shear induced pore pressure generation vs axial strain (Figure 6-5) show the shear induced pore pressure generation that occurs during these different loading situations. It can be clearly seen that as the loading direction is reversed, shear induced pore pressure continues to be generated. This change from either compression to extension or extension to compression must also correspond with movement inside the yield surface. As discussed in section 2.6, the undrained stress path of a normally consolidated specimen traces out the shape of the yield surface. Therefore by switching shearing mode, the stress path in p'-q space will traverse the yield surface until it again reaches a state of yielding. In traditional elasto-plastic constitutive models, movement within the yield surface would generate no excess pore pressure with all strains recoverable. The results seen in Figure 6-5 show a significant deviation from this theory and suggest significant plastic deformation occurs whilst inside the yield surface for RGoM-EI.

When looking at the shear induced pore pressures, it is important to consider them in the context of stresses applied. Figure 6-6 shows the stress-strain results of one triaxial test that was run initially in compression then subsequently extension. The point A represents the end of triaxial compression and the beginning of extension in the sample. At point B there is zero shear stress acting on the specimen and point C represents the peak shear stress in extension. These same three points can be found on Figure 6-7 which shows normalised shear induced pore pressure vs axial strain. From this figure it is clearly shown that between A and B, virtually no shear induced pore pressure is generated. This portion of the extension test therefore represents an almost elastic unloading of the specimen. At point B there is a jump rotation in the major principal stress direction, which then acts laterally on the specimen. Between B and C there is initially a steady increase in the amount of pore pressure generated before a jump in the rate of generation shortly before peak shear stress is reached. After C the shear stress on the sample reduces but pore pressure continues to be generated as the failure envelope begins to be traced. Eventually pore pressure generation levels off as critical state conditions are reached within the specimen.

6.4.7 Strength Data

The strength of the material is assessed by calculating the undrained strength ratio and critical state friction angle. The critical state friction angle, φ'_{CS}, is the friction angle when the material is straining without changes in pore pressure or shear stress – something which can be typically be interpreted after $\varepsilon_a > 10\ \%$ is seen in undrained shear (Pestana and Whittle 1999). In Figure 6-17, the critical state friction angles for all the triaxial tests conducted in this study can be seen. Also shown are results from Fahy (2014) who performed triaxial tests on RGoM-EI at effective stresses ranging from 0.12 – 10 MPa, with one test consolidated to 63 MPa. Results from this work show critical state friction angles clustered between 13 – 16 degrees when consolidated to 40 MPa, with similar angles in both modes of undrained shear. These values are slightly higher than would be implied from the results of previous tests on RGoM-EI, and implies the critical state friction angle reduces slightly less rapidly in log space than was previously suggested. This high plasticity material still shows a very large reduction in friction angle, halving from ~28 to 14 degrees between 1 – 40 MPa. This reduction is a result of the material yield surface evolving very rapidly with stress level, becoming increasingly elongated about the effective stress axis (Casey 2014). For stresses above 40 MPa, one would expect this trend to continue. Looking at Figure 6-8, the yield surface at above 40 MPa would be expected to be inside the 40 MPa yield surface on a normalised plot.

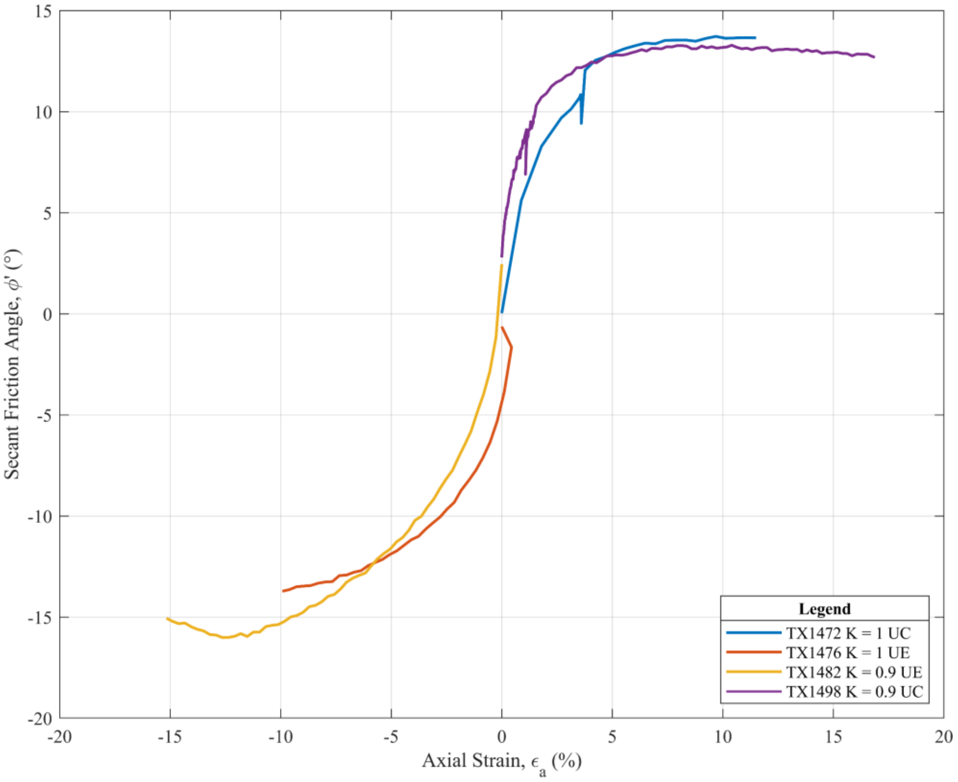

Figure 6-16 – Secant friction angle vs axial strain for four triaxial tests consolidated to 40 MPa with either hydrostatic or drained stress path consolidation histories.

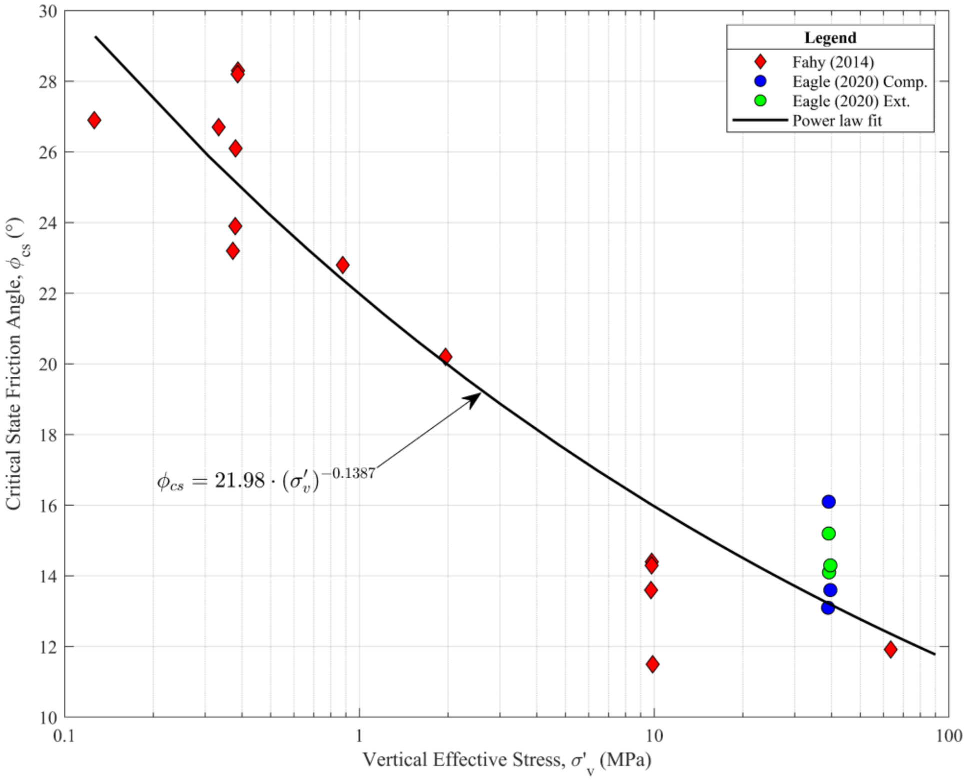

Figure 6-17 - Comparison of critical state friction angles from this study with other test data on RGoM-EI.

6.4.8 Yield Surfaces

As discussed in section 2.6, the effective stress paths for triaxial compression and extension combined with the Mohr-Coulomb failure envelopes allows one to locate the yield surface of a soil in p'-q stress space. In Figure 6-18 can be seen a portion of the undrained stress path for TX1472 which has been previously presented. The early direction of the stress path, where both the mean effective and shear stresses increase is unexpected behaviour for a normally consolidated clay. The slope of this line implies some of this behaviour is occurring elastically, and that the stress state of the material at the beginning of shear did not in fact fall on the yield envelope. It appears that secondary compression that would have occurred after the specimen had finished consolidating has caused the yield envelope to increase significantly in size. Another possible explanation could be due to a slow rotation of the yield surface occurring after the resedimentation stage, when the specimen was K_0 consolidated to 10 MPa.

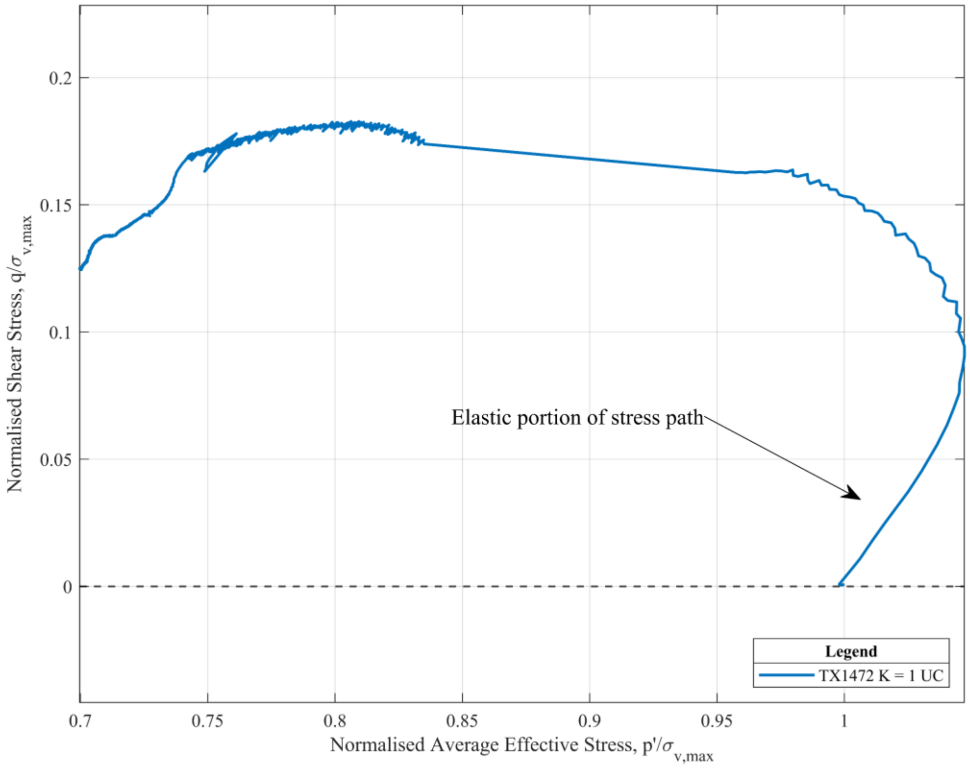

Figure 6-18 - Portion of undrained stress path for TX1472 triaxial compression test.

7 Constitutive Modelling

7.1 Introduction

Constitutive soil models are mathematical representations of real soil behaviour. They can be used for a variety of engineering applications and provide a response to specific loading conditions. These models can then be incorporated into finite element programmes enabling extremely complex situations to be modelled or where traditional testing methods are impractical or too costly. These models are able to have near-surface applications for assessing soil structure interactions as well as the ability to model geologic and drilling processes.

Soil, being a three-phase non-linear material, presents enormous challenges for those wishing to model their behaviour. Additionally, the vast range in size of particles in soils present additional challenges in modelling, especially those hoping to capture behaviour of both clays and sands. The basis of today's soil constitutive models began with work in the field of plasticity theory. Tresca in 1864 studied the behaviour of crystalline metals, eventually leading to the development of his eponymous yield criterion. Research continued in the field with many advancements in mathematical formulations used to describe yield criterions and plastic flow rules. Work in the 1940s and 50s saw the creation of classical plasticity theory with the introduction of the flow rule, consistency condition and hardening rule (Hill 1948; Prager 1949) as well as its application to soil mechanics (Drucker and Prager 1952).

Metals are much simpler to model than soils as their yielding is purely a function of the shear stresses imposed on them – that is they are pressure independent materials. Yielding in soils however is a function of both the shear and mean effective stresses. Mathematical formulations developed originally for metals and alloys have therefore had to be adapted to account for this.

When modelling sands, it is widely accepted that formulations for their yield surface must be functions of their stress level and density (Lade and Duncan (1975), Nishi and Esashí (1978)). However, for formulations of yield surfaces in cohesive materials, such as in MCC and MIT-E3, yield surfaces are assumed to be unique and are not functions of stress level or density. This is the basis of normalised behaviour in clays. Both MCC and MIT-E3 are single yield surface models. Figure 7-1 shows these two yield surfaces on a single normalised plot in p'-q stress space. MCC has an isotropic yield surface with symmetry about the hydrostatic axis whereas the yield surface for MIT-E3 is able to rotate and align with the direction of loading.

In addition to directly running constitutive soil models in this work, they were also applied within FEA simulations of a standard laboratory triaxial specimen. This was done in order to evaluate the impacts of boundary conditions on the stress field and distribution of pore pressure within a specimen. Results from these simulations can be seen in section 7.5.

For further background on the modelling used within this thesis, please refer to Appendix B for a detailed description of how loads and boundary conditions on a triaxial specimen were simulated, along with a description of how the models were validated.

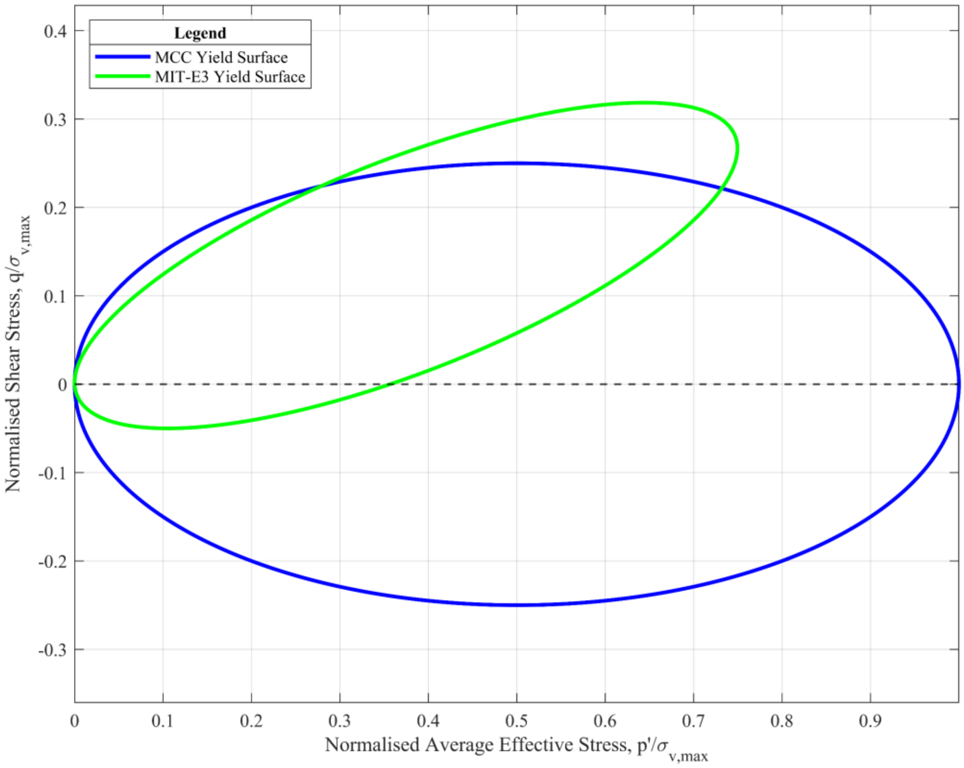

Figure 7-1 - Comparison of MCC and MIT-E3 yield surfaces in normalised p-q space. Figure is adapted from (Pestana and Whittle 1999).

7.2 Modified Cam-Clay (MCC)

MCC is an elastoplastic critical state soil model that was developed by (Roscoe and Burland 1968). It provided the foundation for later more advanced soil model formulations. Despite being formulated over half a century ago, it is still an extremely popular constitutive model for describing the behaviour clays and poorly lithified mudrocks due its relatively few input parameters and acceptable representation of the essential mechanical characteristics (Heidari et al. 2020).

One important limitation of MCC is that it has an isotropic yield surface. This means that for consolidation histories that are not isotropic, the model cannot capture various forms of anisotropy that may then be present in the material. This means it is unable to predict different critical states for triaxial compression vs triaxial extension.

Values for the MCC model were taken from (Heidari et al. 2020), whose models were based on test data from the same RGoM-EI material. One oedometer test and one normally consolidated undrained triaxial test is sufficient to obtain all the input parameters for the model.

The yield surface for MCC is represented by the following equation:

$$\mathrm{f} = \frac{q^2}{M^2} + p(p - p_c) = 0 \tag{7-1}$$

Here p and q are the mean and shear stresses, respectively. Parameter p_c sets the size of the yield surface and is the preconsolidation mean stress. M represents the slope of the critical state line or can be seen as the slope of the line from the origin to the crest of the yield surface in q-p space. This strength parameter is related to the internal friction angle of the soil through the following equation:

$$M = \frac{6 \sin \varphi'}{3 - \sin \varphi'} \tag{7-2}$$

Table 7-1 - MCC input parameters for RGoM-EI.

MCC Input Parameters	
Parameter description	**Value**
Secant slope of failure envelope ($\boldsymbol{M}$)	0.772
Poisson's Ratio ($\boldsymbol{\nu}$)	0.25
Intercept of isotropic normal compression line ($\boldsymbol{N}$)	0.9
Slope of isotropic normal compression line ($\boldsymbol{\lambda}$)	0.161
Slope of recompression line ($\boldsymbol{\kappa}$)	0.054

7.3 MIT-E3 Constitutive Model

MIT-E3 is a soil constitutive model that was developed at MIT in the 1980s to predict the behaviour of friction piles in soft clays under cyclic loading (Whittle 1987). The model assumes normalised soil properties, a concept that was originally proposed the decade prior and is encapsulated in the SHANSEP design procedure (Ladd and Foott 1974). The MIT-E3 model builds on work developing the MCC model and adds complexity so that it can capture a much richer amount of soil behaviour. MIT-E3 contains 15 input parameters compared to just 5 to define MCC. MIT-E3 contains a non-associated flow rule, something which has been shown to be necessary in obtaining K_0 conditions within the model (Kavvadas 1982). This is in contrast to the associated flow rule for MCC, where the direction of plastic strain increments are normal to the yield surface. An associated flow rule also implies that the yield surface has the same mathematical representation as the plastic potential.

It is also worth noting that the MIT-E3 model yield surface can be reduced back to that of the MCC model by setting a second order tensor describing the orientation of the yield surface equal to zero.

In this research MIT-E3 has been used to make comparisons with real triaxial data and assess its performance at high stress levels. Development of more advanced constitutive soil models has continued since the development of MIT-E3, with models such as MIT-S1 that are capable of describing the behaviour of sands as well as overconsolidated clays and silts within one unified framework (Pestana and Whittle 1999).

Work from Casey (2014) has suggested that assuming normalised behaviour of clay is only true over a limited stress range and that real data shows significant stress dependence of clays over large stress ranges.

6 of the 15 input parameters to the MIT-E3 soil model can be obtained from standard laboratory tests, with the other parameters estimated from parametric studies. In this manner, the MIT-E3 model can be adjusted to mimic a broad range of real clay behaviour. Some of the important input parameters for modelling undrained shear behaviour are described in the following sections.

Table 7-2 - MIT-E3 input parameters for RGoM-EI.

Symbol	Parameter Description	**Value**
$\boldsymbol{e_0}$	Void Ratio at reference stress	1.492
$\boldsymbol{\lambda}$	Compressibility of virgin normally consolidated clay	0.282
$\boldsymbol{C}$	Non-linear volumetric swelling behaviour	6.25
$\boldsymbol{n}$	Non-linear volumetric swelling behaviour	1.53
$\boldsymbol{h}$	Irrecoverable plastic strain	0.3
$\boldsymbol{K_{0NC}}$	K_0 for virgin normally consolidated clay	0.9
$\boldsymbol{\frac{2G}{K}}$	Ratio of elastic shear to bulk modulus	0.923
$\boldsymbol{\phi_{TC}}$	Critical state friction angle compression	25.6°
$\boldsymbol{\phi_{TE}}$	Critical state friction angle extension	27.8°
$\boldsymbol{c}$	Undrained shear strength	0.73
$\boldsymbol{s_t}$	Amount of post peak strain softening in undrained triaxial compression	1.0

$\boldsymbol{\omega}$	Non-linearity at small strain in undrained shear	0.39
$\boldsymbol{\gamma}$	Shear induced pore pressure for OC clay	0.5
$\boldsymbol{\kappa_0}$	Small strain compressibility at load reversal	0.0065
$\boldsymbol{\psi_0}$	Rate of evolution of anisotropy (rotation of bounding surface)	100

7.3.1 Model parameter $\mathbf{K_{0NC}}$

The coefficient of lateral earth pressure at rest for normally consolidated clay was able to be obtained from K_0 triaxial tests. A value of 0.9 for material consolidated to 40 MPa was selected after assessing previous data on RGoM-EI.

7.3.2 Model parameter λ, $\mathbf{e_0}$

The compressibility of RGoM-EI is captured in the MIT-E3 model through two parameters, λ, e_0 which define the virgin consolidation line (VCL). The results of two oedometer tests on RGoM-EI undertaken by Uyeturk (2021) are shown below in Figure 7-2. From this a value for e_0 of 1.45 and λ of 0.174. The slope of the VCL is given by the following equation:

$$\lambda = \frac{\Delta e}{\Delta \ln(\sigma'_v)} \tag{7-3}$$

Since the slope of the VCL for this material is not linear in void ratio vs log stress space, the slope of the VCL was biased towards the readings closer to 40 MPa consolidation stress.

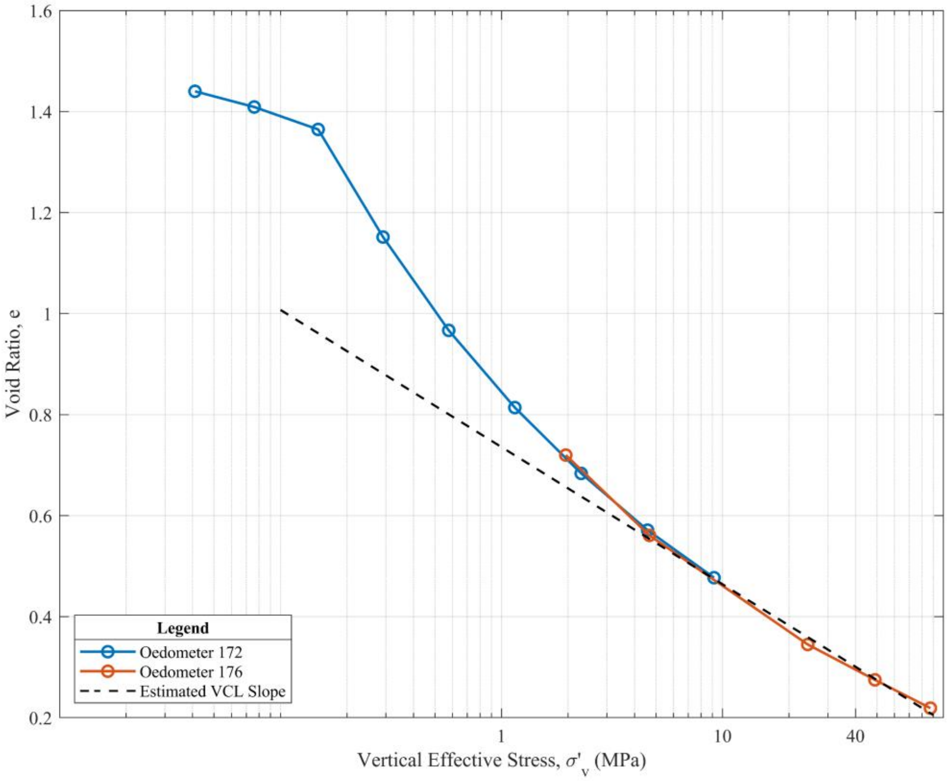

Figure 7-2 - RGoM-EI compression data. Results of two oedometer tests are shown along with an interpreted VCL.

7.3.3 Model parameter S_t

The parameter S_t in the MIT-E3 formulation is derived from the undrained shear behaviour of K_0 normally consolidated clay. Varying this parameter influences the strain softening of the clay, whilst largely unaffecting the undrained strength of the material (Whittle and Kavvadas 1994). For this work, a value of 2.5 was selected.

7.3.4 Parameter c

Parameter c is used for controlling the shear strength both in triaxial compression and triaxial extension. Increasing c leads to an increase in compressional strength, and an even greater increase in extensional undrained strength. This parameter can be used within MIT-E3 to better match the experimental data.

7.3.5 Parameter γ

The amount of shear-induced pore pressure in overconsolidated clays is controlled by γ within the formulation.

7.3.6 Ratio of Elastic Shear to Bulk Modulus

Another input into the MIT-E3 model is the ratio of the shear to bulk modulus of the material. This can be estimated from the Poisson's ratio with the following equation (Wroth 1984):

$$\frac{2G}{K} = 3\frac{(1 - 2\nu')}{(1 + \nu')} \tag{1}$$

Here ν' represents the elastic Poisson's ratio at load reversal. For the RGoM material a Poisson's ratio of 0.3 was used leading to a modulus ratio of 0.923.

7.3.7 Friction angles

The friction angles set the bounds of the failure surface in the MIT-E3 model at critical state conditions. ϕ'_{TC} sets a limiting condition for triaxial compression whilst ϕ'_{TE} sets a limit for triaxial extension. The introduction of these parameters is a departure from MCC, where the failure surface is isotropic.

Both parameters are found by undrained shearing specimens to $\varepsilon_a \approx 10\ \%$ in their respective mode.

7.3.8 Rate of change of anisotropy

The rate of change of anisotropy is controlled by the parameter ψ_0 within the model. Larger values of this parameter means that the yield surface in the model rotates more quickly for a given imposed strain.

Figure 7-3 shows the effects of altering the parameter within the MIT-E3 model. It can be seen that for values of ψ_0 between 75 – 200 the effects of anisotropy appear to erode after the stress level has increased by around 3 times. Parametric studies have shown that this parameter has little influence on model predictions, and so a recommended default value of 100 was used in within the model (Whittle and Sutabutr 2005).

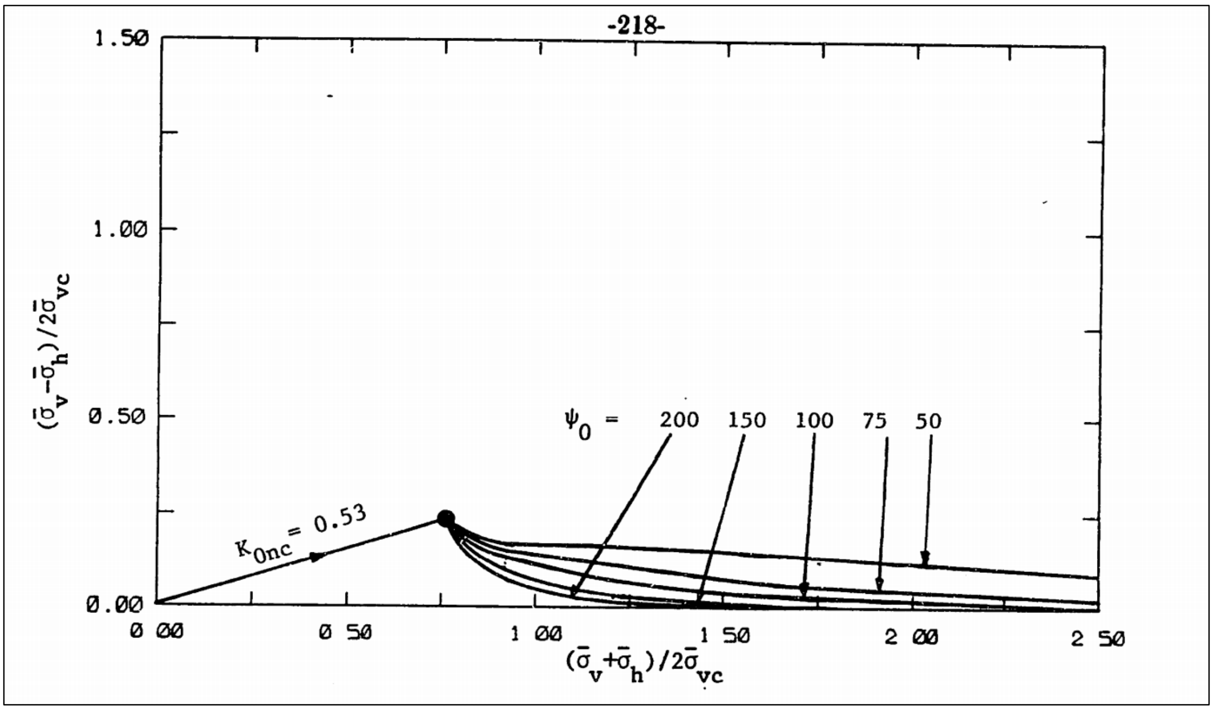

Figure 7-3 - Effect of parameter ψ_0 as model initially K_0 consolidates and then hydrostatically consolidates.

7.4 MIT-E3 Simulation Results

Presented below are some results from simulations using the MIT-E3 constitutive soil model. In Figure 7-4 can be seen a comparison of the effective stress paths for RGoM-EI against an MIT-E3 simulation. In Figure 7-5 The simulation can be seen to replicate the behaviour well initially, though struggles to capture the strain softening behaviour fully, especially in triaxial extension.

Figure 7-6 shows the effective stress path for the simulation of shear reversal. The model is run initially in extension for 15 % axial strain, before being run in compression for 30 % axial strain. Again, the model is able to be tuned to capture the real behaviour, shown also in the figure, to a reasonably good accuracy. The model also captures the initial elastic behaviour at shear reversal, where the stress path travels along a 3 in 1 slope, before developing excess pore pressures and deviating to the left.

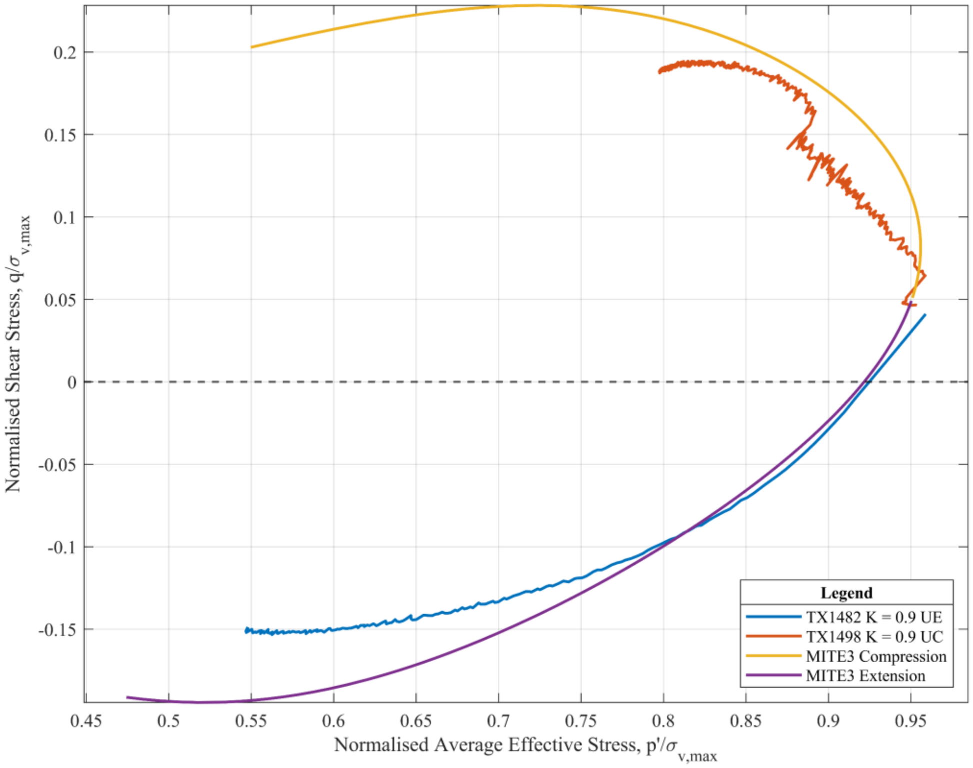

Figure 7-4 - Comparison of the undrained shear effective stress paths in extension and compression for RGoM-EI with the MIT-E3 model ($\sigma_{v,max} = 40\ MPa$, K = 0.9).

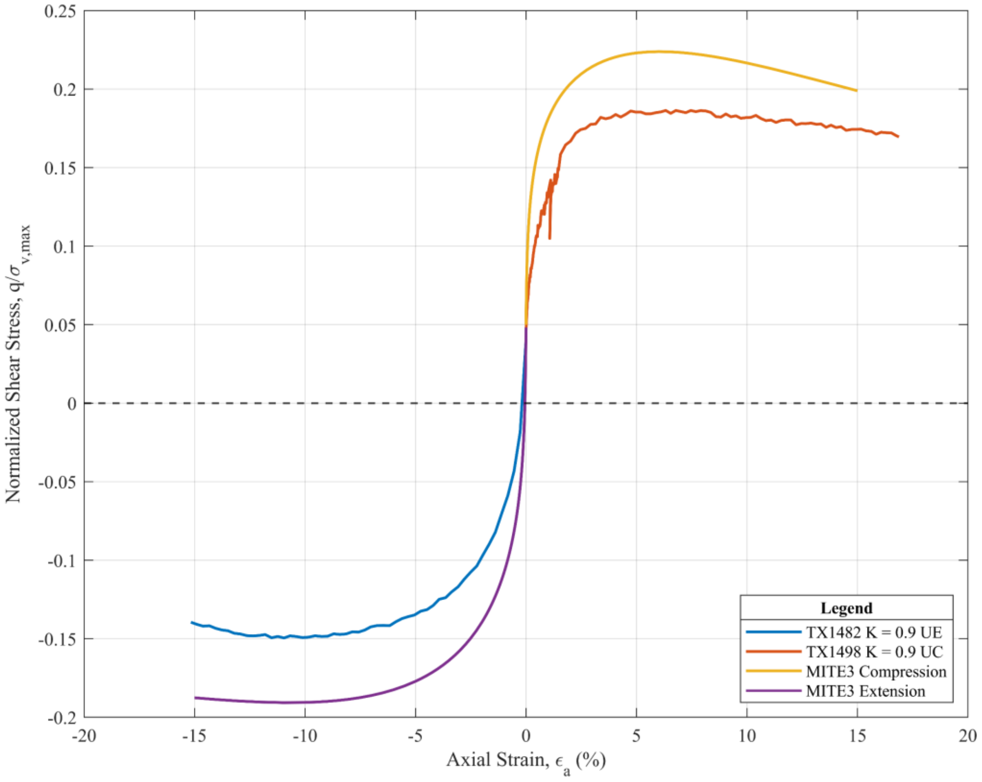

Figure 7-5 - Comparison of stress strain data against MIT-E3 model predictions.

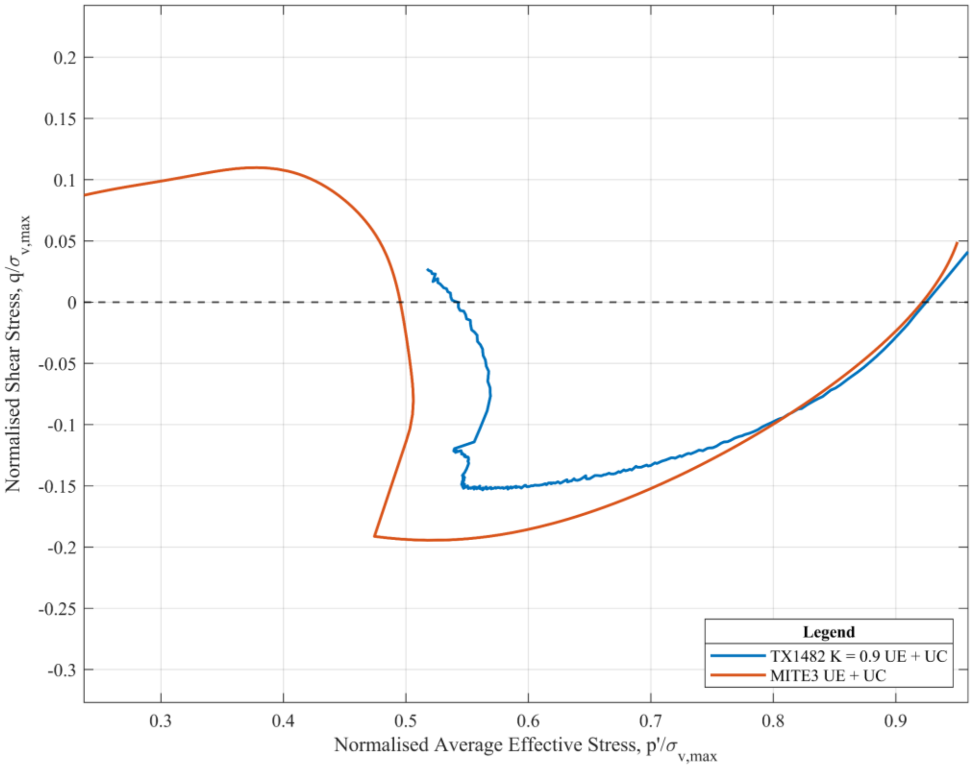

Figure 7-6 - Simulation of shear reversal using MIT-E3 simulation.

7.5 MCC Simulation Results

For an MCC soil model running in triaxial compression, measured excess pore pressures in the sample varied from approximately 20 MPa at the centre to 8 MPa at the top. This distribution of excess pore pressure can be seen in Figure 7-7. The impact of a zero lateral restraint boundary can be seen clearly in the FEA results, with an increase to 50 MPa locally in the element to the top right of the figure.

Interestingly, Figure 7-8 shows an unexpected distribution of pore pressure within a standard triaxial specimen during undrained shearing in extension. Excess pore pressure can be seen to vary from negative values at the specimen centre, to positive values and then back to negative towards the top of the sample. This appears to be related to the short duration for shearing coupled with the very low permeability applied within the model. Indeed, by increasing the permeability of the model by three orders of magnitude, pore pressure is able to redistribute, and this effect is not seen.

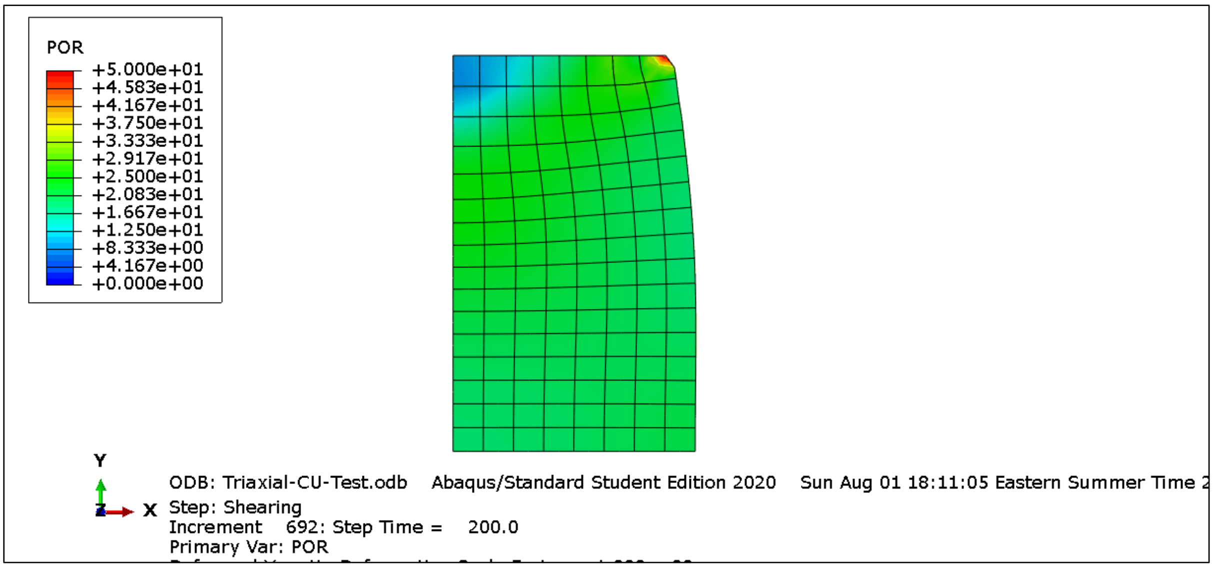

Figure 7-7 - Distribution of excess pore pressure in TX compression with an MCC soil model. Units are in MPa.

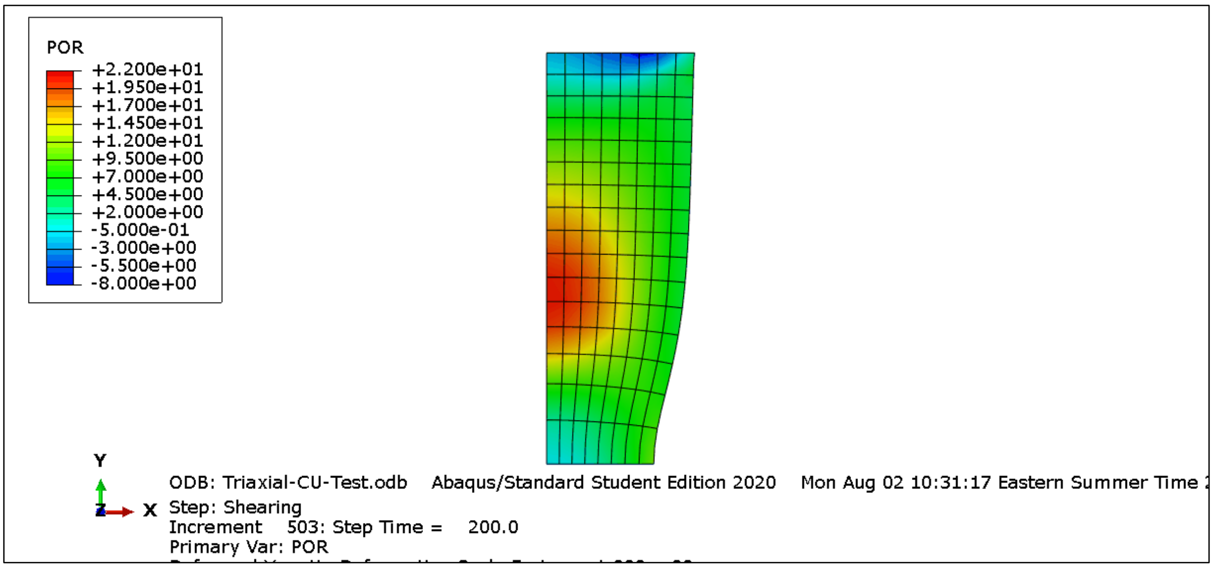

Figure 7-8 - Distribution of excess pore pressure in TX extension with an MCC soil model. Note the legend has a different scaling to Figure 7-7. Units are in MPa.

8 Conclusions and Recommendations

8.1 Introduction

Results from reversing the direction of shear, causing the stress path to move across the yield surface of the material, show significant shear induced pore pressure generation after reversal. This proves that the material does not behave close to elastically inside its yield surface.

Stress strain data shows that in an extensional mode of shear, the material reaches a similar peak shear stress, but after a greater amount of axial strain. This suggests the response of the material in triaxial extension is more ductile than in compression.

Comparisons of friction angle with the existing database for RGoM-EI indicates slightly higher critical state friction angles at higher stresses than have previously been estimated by extrapolating from low stress data. Results do however support previous studies which show friction angle reducing with increasing stress level.

Issues pertaining to volume control led to a low degree of confidence in K_0 measurements that were made continuously during consolidation. Data did show however the sensitivity of RGoM-EI to consolidation strain rate and highlighted the importance of choosing suitably low strain rates for low permeability materials at high consolidation stress. Comparisons of the yield surface between $K = 0.9$ and $K=1$ also shows the yield surface has rotated in the direction of consolidation in p-q space.

Results of simulations of a triaxial specimen using an MCC constitutive model suggest that triaxial extension appears to show a more complex distribution of pore pressure than in triaxial compression.

8.2 Recommendations

8.2.1 Drainage Height

Due to various equipment failures and time constraints, no triaxial testing was conducted at stress > 40 MPa. The high pressure triaxial system however is capable of consolidation stresses of up to 100 MPa. There would be significant value in testing at even higher consolidation stresses and evaluating the mechanical results against the current database for RGoM-EI. As discussed in chapter 5, Wissa's linear equations predict very large excess pore pressure generation at the centre of the RGoM-EI soil specimens when consolidated above 20 MPa if strain rates are too large. Consolidating to stresses approaching 100 MPa necessitates consolidation strain rates that are < 0.02 %/hr, something which makes testing extremely challenging as equipment is occupied for ever increasing time periods. Further work could reduce the aspect ratio of the specimen closer to a value of one from the aspect ratio of approximately 2.3 used in this research. Another approach could be to increase the consolidation stress applied to the specimen during consolidation, thus reducing the time a specimen spends inside the triaxial cell.

8.2.2 Intermediate Principal Stress

Triaxial testing is the most common form of testing procedure employed by geotechnical researchers where soil specimens, cylindrical in shape, are loaded under axisymmetric conditions. This does not represent true loading conditions experienced in real world geotechnical settings however, with most situations better represented by plane strain conditions. Indeed work by numerous researchers has shown that some soils possess higher strength in plane strain conditions than in the axisymmetric case (Henkel and Wade 1966). Failure modes seen in triaxial compression often develop more complex deformation patterns than in plain strain testing. This would influence the undrained stress path and therefore the interpreted yield surface location. Undrained testing using a plane strain apparatus could be used to determine how great an impact there is from the intermediate principal stress and whether it is consistent with varying stress level. Gaining data from plane strain tests would also provide additional data points on the yield surface, allowing it to be defined in three-dimensional stress space. This would clearly be beneficial for those wishing to model the material.

8.2.3 Cementation Issues

As vertical effective stresses reach closer to 100 MPa inside the triaxial cell, conditions replicate the stresses seen at several kilometres depth in the Gulf of Mexico. These stresses would have evolved over significant geologic time, something that cannot be replicated in the laboratory. Processes such as recrystallization or cementation may occur over this time leading to lithification of the sediment. Samples produced in the laboratory are uncemented with no recrystallization, and therefore would see a less brittle response than a lithified material. Furthermore, RGoM-EI may be predisposed to these diagenetic processes due its mineralogy. Illite-smectite interstratified clay minerals, dominant in RGoM-EI, have been linked to processes such as rock cementation (Stixrude and Peacor 2002). This would exacerbate the problems associated with not being able to simulate geologic time in the laboratory.

Additionally, in situ temperatures at depths where the GoM-EI material was extracted are higher than the 20° Celsius selected as the temperature for experiments. It is well understood that increasing temperature can increase the rate of processes that effect the microfabric of the clay – such as through smectite diagenesis.

9 References

Abdulhadi, N. O. (2009). “An experimental investigation into the stress-dependent mechanical behavior of cohesive soil with application to wellbore instability.” Massachusetts Institute of Technology.

Alexander, L. L., and Flemings, P. B. (1995). “Geologic Evolution of a Pliocene–Pleistocene Salt-Withdrawal Minibasin: Eugene Island Block 330, Offshore Louisiana 1.” *AAPG Bulletin*, 79(12), 1737–1756.

Anderson, R. N., He, W., Hobart, M. A., Wilkinson, C. R., and Nelson, H. R. (1991). “Active fluid flow in the Eugene Island area, offshore Louisiana.” *The Leading Edge*, Society of Exploration Geophysicists, 10(4), 12–17.

ASTM International. (2006). “D2487-17e1 Standard Practice for Classification of Soils for Engineering Purposes (Unified Soil Classification System.” *Annual Book of ASTM Standards*, 4, 249–260.

ASTM International. (2014). “ASTM D854-14 Standard Test Methods for Specific Gravity of Soil Solids by Water Pycnometer.” *Annual Book of ASTM Standards*.

ASTM International. (2015). “D2850-15 Standard Test Method for Unconsolidated-Undrained Triaxial Compression Test on Cohesive Soils.” *Annual Book of ASTM Standards*.

ASTM International. (2017). “D4318-17e1 Standard Test Methods for Liquid Limit, Plastic Limit, and Plasticity Index of Soils.” *Annual Book of ASTM Standards*.

ASTM International. (2020). “D4186-20e1 Standard Test Method for One-Dimensional Consolidation Properties of Saturated Cohesive Soils Using Controlled-Strain Loading.” *Annual Book of ASTM Standards*, D4186/D418.

Betts, W. S. (2014). “Compressibility and permeability of Gulf of Mexico mudrocks, resedimented and in-situ.” The University of Texas at Austin.

Bigoni, D. (2012). *Nonlinear solid mechanics: bifurcation theory and material instability*. Cambridge University Press.

Bishop, A. W. (1973). “The influence of an undrained change in stress on the pore pressure in porous media of low compressibility.” *Geotechnique*, Thomas Telford Ltd, 23(3), 435–442.

Bishop, A. W., and Wesley, L. D. (1975). “A hydraulic triaxial apparatus for controlled stress path testing.” *Geotechnique*, Thomas Telford Ltd, 25(4), 657–670.

Cai, Y., Hao, B., Gu, C., Wang, J., and Pan, L. (2018). “Effect of anisotropic consolidation stress paths on the undrained shear behavior of reconstituted Wenzhou clay.” *Engineering Geology*, Elsevier B.V., 242, 23–33.

Casey, B. (2014). “The consolidation and strength behavior of mechanically compressed fine-grained sediments.” Massachusetts Institute of Technology.

Casey, B., and Germaine, J. T. (2014). “An evaluation of three triaxial systems with results from 0.1 to 100 MPa.” *Geotechnical Testing Journal*, ASTM International, 37(6), 1068–1074.

Casey, B., Germaine, J. T., Flemings, P. B., and Fahy, B. P. (2016). “In situ stress state and strength in mudrocks.” *Journal of Geophysical Research: Solid Earth*, Wiley Online Library, 121(8), 5611–5623.

Casey, B., Germaine, J. T., Flemings, P. B., Reece, J. S., Gao, B., and Betts, W. (2013). “Liquid limit as a predictor of mudrock permeability.” *Marine and Petroleum Geology*, Elsevier, 44, 256–263.

Das, B. M. (2019). *Advanced soil mechanics*. CRC press.

Drucker, D. C., and Prager, W. (1952). “Soil mechanics and plastic analysis or limit design.” *Quarterly of applied mathematics*, 10(2), 157–165.

Fahy, B. P. (2014). “The influence of salinity on the mechanical behavior of high plasticity soils.” Massachusetts Institute of Technology.

Germaine, J. T. (1982). “Development of the directional shear cell for measuring cross-anisotropic clay properties.” *ScD Thesis, Massachusetts Inst. of Tech.*

Germaine, J. T., and Germaine, A. V. (2009). *Geotechnical laboratory measurements for engineers*. John Wiley & Sons.

Germaine, J. T., and Ladd, C. C. (1988). “State-of-the-art paper: Triaxial testing of saturated cohesive soils.” *Advanced triaxial testing of soil and rock,* ASTM International.

Graham, J., Crooks, J. H. A., and Bell, A. L. (1983). “Time effects on the stress-strain behaviour of natural soft clays.” *Géotechnique,* Thomas Telford Ltd, 33(3), 327–340.

Gue, C. S., Lunne, T., and Perkins, S. (2015). “Temperature effects on laboratory measured strength on deep water soft clays.” *Frontiers in Offshore Geotechnics III: Proceedings of the 3rd International Symposium on Frontiers in Offshore Geotechnics (ISFOG 2015),* Taylor & Francis Books Ltd, 1055–1060.

Guerin, G. (2000). “Acoustic and thermal characterization of oil migration, gas hydrates formation and silica diagenesis.” Columbia University.

Hanley, A. J. (2017). “The Characterization of the Yield Surface for Fine-Grained Sediments.” Tufts University.

Heidari, M., Nikolinakou, M. A., and Flemings, P. B. (2020). “Modified Cam-Clay Model for Large Stress Ranges and Its Predictions for Geological and Drilling Processes.” *Journal of Geophysical Research: Solid Earth,* Wiley Online Library, 125(12), e2020JB019500.

Henkel, D. J., and Wade, N. H. (1966). “Plane Strain Tests on A Saturated Remoded Clay.” *Journal of the Soil Mechanics and Foundations Division,* American Society of Civil Engineers, 92(6), 67–80.

Hill, R. (1948). “A theory of the yielding and plastic flow of anisotropic metals.” *Proceedings of the Royal Society of London. Series A. Mathematical and Physical Sciences,* The Royal Society London, 193(1033), 281–297.

Hillier, S. (2000). “Accurate quantitative analysis of clay and other minerals in sandstones by XRD: comparison of a Rietveld and a reference intensity ratio (RIR) method and the importance of sample preparation.” *Clay minerals,* Mineralogical Society of Great Britain and Ireland, 35(1), 291–302.

Kavvadas, M. (1982). “Non-linear consolidation around driven piles in clays.” Massachusetts Institute of Technology.

Kester, W. (2004). *Analog-Digital Conversion*. Analog Devices.

Kurukulasuriya, L. C., Oda, M., and KAzAMA, Hidehi. (1999). “Anisotropy of undrained shear strength of an over-consolidated soil by triaxial and plane strain tests.” *Soils and foundations,* Elsevier, 39(1), 21–29.

Ladd, C. C. (1964). “Stress-strain modulus of clay in undrained shear.” *Journal of the Soil Mechanics and Foundations Division,* American Society of Civil Engineers, 90(5), 103–132.

Ladd, C. C., and Foott, R. (1974). “New design procedure for stability of soft clays.” *Journal of the geotechnical engineering division,* American Society of Civil Engineers, 100(7), 763–786.

Lade, P. V, and Duncan, J. M. (1975). “Elastoplastic stress-strain theory for cohesionless soil.” *Journal of the geotechnical engineering division,* American Society of Civil Engineers, 101(10), 1037–1053.

Leroueil, S., Tavenas, F., La Rochelle, P., and Tremblay, M. (1988). “Influence of filter paper and leakage on triaxial testing.” *Advanced triaxial testing of soil and rock,* ASTM International.

Losh, S., and Wood, J. (1995). “Brine Chemistry, Blocks 330 and 316, Results of the Pathfinder drilling program into a major growth fault (CD-ROM): Palisades, NY.” LDEO Press. Lamont Doherty Earth Observatory.

Moore, W. M. (1966). “Effect of Variations in Poissons Ratio on Soil Triaxial Testing.” *Highway Research Record,* (108).

Murawski, S. A., Hollander, D. J., Gilbert, S., and Gracia, A. (2020). “Deepwater Oil and Gas Production in the Gulf of Mexico and Related Global Trends.” *Scenarios and Responses to Future Deep Oil Spills,* Springer International Publishing, 16–32.

Nikolinakou, M. A., Flemings, P. B., and Hudec, M. R. (2014). “Modeling stress evolution around a rising salt diapir.” *Marine and Petroleum Geology,* Elsevier, 51, 230–238.

Nishi, K., and Esashí, Y. (1978). “Stress-strain relationships of sand based on elasto-plasticity theory.” *Proceedings of the Japan Society of Civil Engineers*, Japan Society of Civil Engineers, 111–122.

Nygård, R., Gutierrez, M., Bratli, R. K., and Høeg, K. (2006). “Brittle-ductile transition, shear failure and leakage in shales and mudrocks.” *Marine and Petroleum Geology*, Elsevier, 23(2), 201–212.

Ono, T. (2002). “Lateral deformation of freezing clay under triaxial stress condition using laser-measuring device.” *Cold Regions Science and Technology*, Elsevier, 35(1), 45–54.

Pestana, J. M., and Whittle, A. J. (1999). “Formulation of a Unified Constitutive Model for Clays and Sands.” *International Journal for Numerical and Analytical Methods in Geomechanics*, Wiley Online Library, 23(12), 1215–1243.

Petley, D. N. (1999). “Failure envelopes of mudrocks at high confining pressures.” *Geological Society, London, Special Publications*, 158(1), 61 LP – 71.

Prager, W. (1949). “Recent developments in the mathematical theory of plasticity.” *Journal of applied physics*, American Institute of Physics, 20(3), 235–241.

Roscoe, K., and Burland, J. B. (1968). “On the Generalized Stress-Strain Behaviour of Wet Clay.”

Santagata, M. C., and Germaine, J. T. (2002). “Sampling disturbance effects in normally consolidated clays.” *Journal of Geotechnical and Geoenvironmental Engineering*, American Society of Civil Engineers, 128(12), 997–1006.

Schmertmann, J. H. (1955). “The Undisturbed Consolidation Behavior of Clay.” *Transactions of the American Society of Civil Engineers*, American Society of Civil Engineers, 120(1), 1201–1227.

Sheahan, T. C. (Thomas C. (1991). “An experimental study of the time-dependent undrained shear behavior of resedimented clay using automated stress path triaxial equipment.” Massachusetts Institute of Technology.

Sheeran, D. E., and Krizek, R. J. . (1971). “Preparation of homogeneous soil samples by slurry consolidation.” *J Mater*, American Society for Testing and Materials, 6(2), 356–373.

Skempton, A. W. (1954). “The Pore-Pressure Coefficients A and B.” *Géotechnique*, ICE Publishing, 4(4), 143–147.

Stixrude, L., and Peacor, D. R. (2002). “First-principles study of illite–smectite and implications for clay mineral systems.” *Nature*, 420(6912), 165–168.

Tanaka, N., Graham, J., and Crilly, T. (1997). “Stress-strain behaviour of reconstituted illitic clay at different temperatures.” *Engineering Geology*, Elsevier, 47(4), 339–350.

Tavenas, F. (1977). “Effects of stresses and time on the yielding of clay.” *Proceedings of the 9th ICSMFE*, 319–326.

US Energy Information Administration. (2018). “Gulf of Mexico fact sheet - real time storm information.” *Report on Gulf of Mexico*, <https://www.eia.gov/special/gulf_of_mexico/> (Jan. 25, 2021).

“UT GeoFluids.” (n.d.). <http://www-udc.ig.utexas.edu/geofluids/> (Apr. 28, 2021).

Uyeturk, E. (Tufts U. (2021). *RGoM-EI Oedometer Testing*.

Whittle, A. J. (1987). “A constitutive model for overconsolidated clays with application to the cyclic loading of friction piles.” Massachusetts Institute of Technology.

Whittle, A. J., and Kavvadas, M. J. (1994). “Formulation of MIT-E3 Constitutive Model for Overconsolidated Clays.” *Journal of Geotechnical Engineering*, 120(1), 173–198.

Whittle, A. J., and Sutabutr, T. (2005). “Parameters for average Gulf Clay and Prediction of Pile Set-up in the Gulf of Mexico.” *Soil Constitutive Models: Evaluation, Selection, and Calibration*, 440–458.

Wissa, A. E. Z., Christian, J. T., Davis, E. H., and Heiberg, S. (1971). “Consolidation at Constant Rate of Strain.” *Journal of the Soil Mechanics and Foundations Division*, American Society of Civil Engineers, 97(10), 1393–1413.

Wroth, C. P. (1984). “The interpretation of in situ soil tests.” *Geotechnique*, Thomas Telford Ltd, 34(4), 449–489.

Appendix A Membrane Corrections

A.1 Introduction

Ensuring a seal that holds throughout the duration of a test is one of the primary challenges faced when performing triaxial experiments. The membrane seals the specimen from the silicon oil within the triaxial chamber from the pore fluid within the specimen. Without a seal, results are uninterpretable and meaningful insights into soil behaviour cannot be drawn. The presence of a membrane does however cause an error in the deviator stress measured, as with increasing membrane stiffness, increasing amounts of load are transmitted through it instead of the sample. In order to quantify the impact of the membrane on the triaxial data, the elastic properties of the membrane had to be estimated through material testing. A segment of the membrane was cut into a dog bone shape and placed into an Instron® 8501 servo hydraulic testing machine. In Figure 9-1 the Young's Modulus was estimated to be 93.7 MPa from the stress strain data. An extensometer was placed on the membrane whilst axial tension was applied in order to measure the lateral strain. The Poisson's ratio was subsequently found to be 0.36, typical for Polyvinylchloride.

The membrane corrections are performed assuming the membrane is an isotropic elastic material. Further assumptions are that the membrane acts as a thin-walled cylinder and that the strains are small.

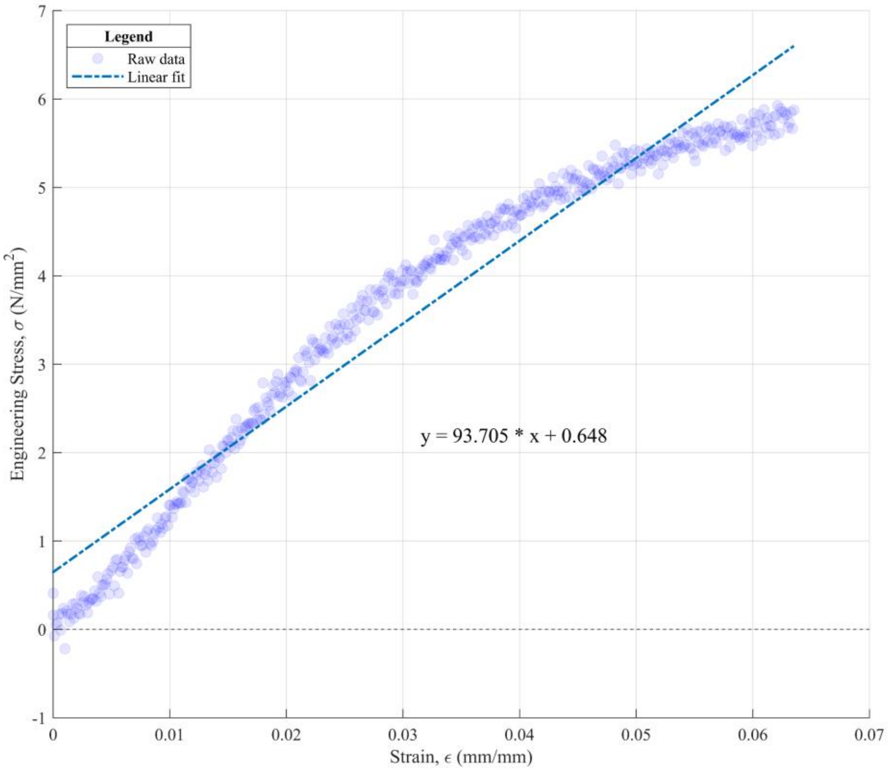

Figure 9-1 - Figure showing calculation of PVC membrane elastic modulus from raw testing data

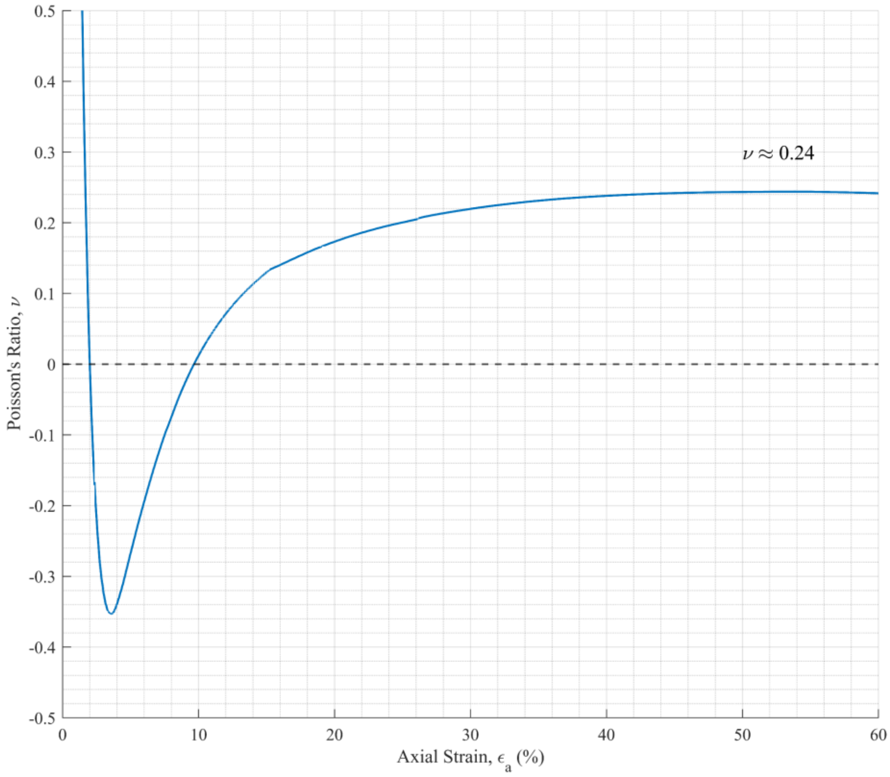

Figure 9-2 - Calculation of Poisson's ratio for the PVC membrane as a function of its axial strain in tension.

A.2 Membrane Correction Derivations

The following assumptions are made during the membrane correction derivations:

- The membrane is isotropic.
- The membrane behaves as a thin-walled cylinder.
- Small strain assumptions apply.

These assumptions significantly simplify the behaviour of the membrane during shear, however the actual behaviour is difficult to determine with more complex solutions lacking consensus as to their validity (ASTM International 2015). As such the following method was used to calculate the stresses in the membrane and perform a post-test correction to the stresses on the sample.

First the axial stress is calculated inside the membrane using force equilibrium. Subscript ‘a’ refers to the axial direction whilst ‘r’ refers to the radial direction.

$$2rLP_r = 2tL\sigma_\theta \tag{9-1}$$

Rearranging for the hoop stress:

$$\sigma_\theta = \frac{rP_r}{t} \tag{9-2}$$

Looking at the forces axially:

$$\pi r^2 P_a = 2\pi r t \sigma_a \tag{9-3}$$

Rearranging for the longitudinal stress:

$$\sigma_a = \frac{rP_a}{2t} \tag{9-4}$$

1- Strain inside the membrane is calculated:

$$\varepsilon = \frac{\sigma}{E} \;\&\; \nu = \frac{-\varepsilon_\perp}{\varepsilon_{||}} \tag{9-5}$$

Combining with expressions for stress in Equations 9-1 and 9-2:

$$\varepsilon_\theta = \frac{\sigma_\theta}{\mathrm{E}} - \mu\frac{\sigma_\mathrm{a}}{\mathrm{E}} \quad \& \quad \varepsilon_a = \frac{\sigma_a}{\mathrm{E}} - \mu\frac{\sigma_\theta}{\mathrm{E}} \tag{9-6}$$

$$\varepsilon_\theta = \frac{rP_r}{\mathrm{Et}} - \mu\frac{rP_\mathrm{a}}{2\mathrm{Et}} \quad \& \quad \varepsilon_a = \frac{rP_a}{2\mathrm{Et}} - \mu\frac{rP_\mathrm{r}}{\mathrm{Et}} \tag{9-7}$$

Let $\beta = \frac{r}{Et}$:

$$\varepsilon_\theta = \beta P_r - \frac{\mu\beta}{2}P_a \quad \& \quad \varepsilon_a = \frac{\beta}{2}P_a - \mu\beta P_r \tag{9-8}$$

Solve for P_r and P_a:

$$\varepsilon_\theta = \beta P_r - \mu(\varepsilon_a + \mu\beta P_r) \quad \& \quad \varepsilon_a = \frac{\beta}{2}P_a - \mu(\varepsilon_\theta + \frac{\mu\beta}{2}P_a) \tag{9-9}$$

$$P_r = \frac{\varepsilon_\theta + \mu\varepsilon_a}{\beta(1-\mu^2)} \quad \& \quad P_a = \frac{2(\varepsilon_a + \mu\varepsilon_\theta)}{\beta(1-\mu^2)} \tag{9-10}$$

Convert ε_θ into a measured value:

$$\varepsilon_\theta = \varepsilon_r = \frac{\varepsilon_{vol} - \varepsilon_a}{2} \tag{9-11}$$

$$P_r = \sigma_r \quad \& \quad P_a = \sigma_a \tag{9-12}$$

$$\sigma_r = \frac{\frac{\varepsilon_{vol}}{2} + \varepsilon_a(\mu - \frac{1}{2})}{\beta(1-\mu^2)} \quad \& \quad \sigma_a = \frac{\mu\varepsilon_{vol} + \varepsilon_a(2-\mu)}{\beta(1-\mu^2)} \tag{9-13}$$

Appendix B FEA

B.1 Introduction

Abaqus FEA (Finite Element Analysis) and Plaxis were used to run a MCC soil model on a 2D representation of a standard laboratory triaxial specimen. By implementing a soil model within an FEA programme, we are able to explore how a clay might behave and how different boundary conditions imposed on specimens impact the stress state and distribution of pore pressure within a triaxial specimen.

Plaxis is a specialised geotechnical computer programme capable of running finite element analyses[2]. It is used extensively in industry with applications in foundations, excavations, tunnelling and mining. The programme comes equipped with commonly used material models including MCC, and the ability to enter user defined material models such as MIT-E3.

Abaqus is a more generalised finite element software, that is also capable of running basic soil models and handling porous mediums with an effective stress analysis.

B.2 Boundary Conditions

The axisymmetric nature of the standard triaxial specimen allowed for a simple 2D rectangular mesh to be used, simplifying the modelling, and reducing the computational demand. This simplification is demonstrated in Figure 9-3 where two axes of symmetry can be seen. The coordinate system has been selected so that the origin represents the centre of the soil specimen.

Typically, as a cylinder is compressed by an axial force, there is a corresponding lateral displacement as it shortens. In the case of a triaxial test, this lateral expansion is inhibited at

---

[2] Plaxis 2D-2020™ version was used for this work.

the top and bottom due to frictional forces between specimen and the porous stones. This effectively places a radial displacement restraint at the top and bottom of the specimen. This is represented in the 2D model by application of a zero horizontal displacement boundary condition along the top boundary of the model. This line maintains all other degrees of freedom.

A summary of all the applied displacement and hydraulic boundary conditions are given below in Table 9-1.

The bottom line represents the centreline of the sample. Due to symmetry, this line does not displace vertically but is free to displace horizontally.

With regards to hydraulic boundaries, seepage is permitted across the top boundary during consolidation with all other boundaries closed due to symmetry. During undrained shear, all boundaries are hydraulically closed.

Before commencing the analysis, a geostatic predefined stress field is applied to the model. This allows the FEA software to calculate stresses which are in equilibrium with gravity and the boundary conditions applied to the model, thus enabling the simulation to converge.

Table 9-1 - Summary of boundary conditions applied in FEA model.

Displacement Boundary Condition	**Consolidation**	**Undrained Shear**
Top Boundary	fixed X, free Y	fixed X, free Y
Bottom Boundary	fixed X, fixed Y	free X, fixed Y
Left Boundary	fixed X, free Y	fixed X, free Y
Right Boundary	fixed X, free Y	free X, free Y
Hydraulic Boundary Condition		
Top Boundary	seepage	closed
Bottom Boundary	closed	closed
Left Boundary	closed	closed
Right Boundary	closed	closed

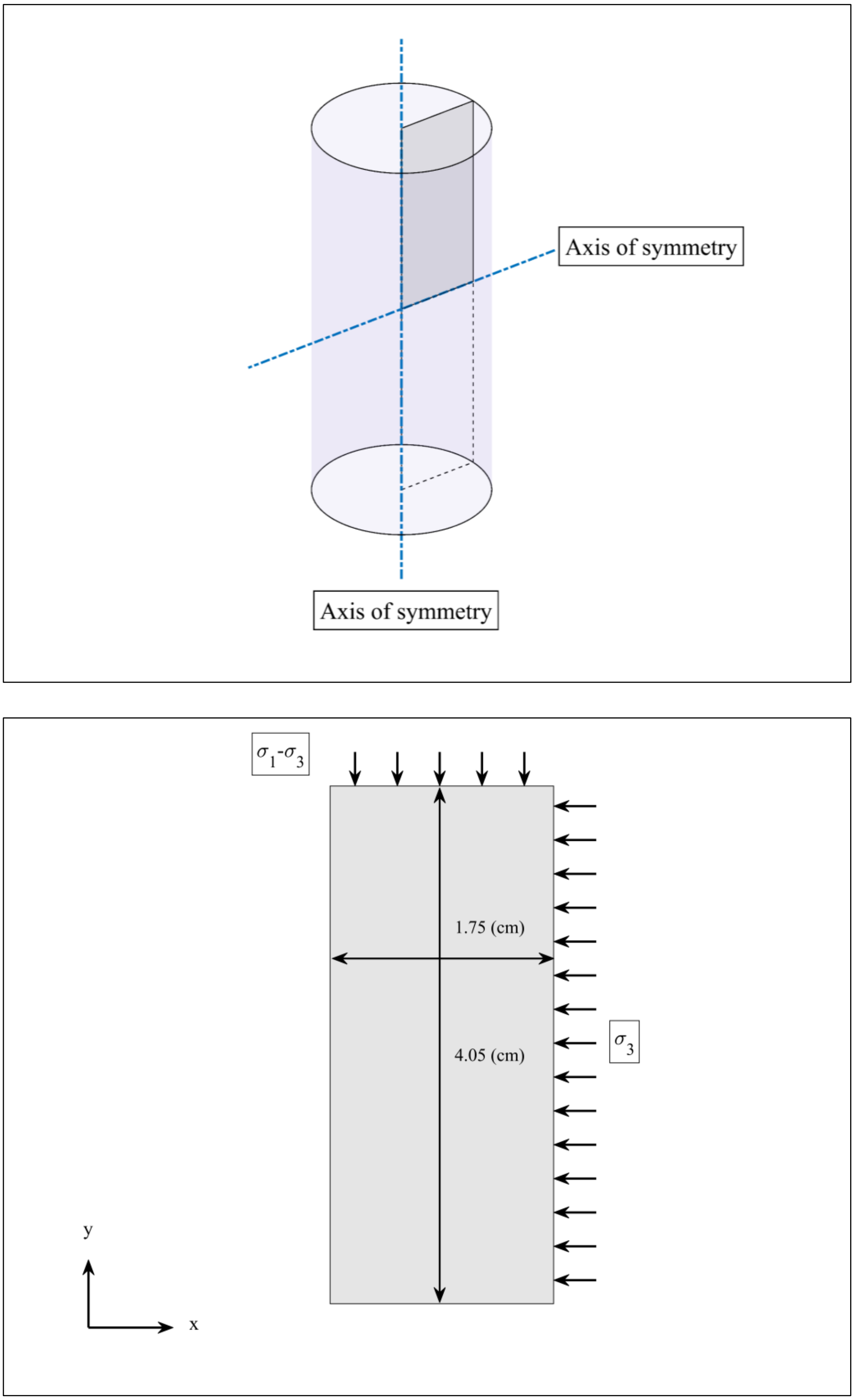

Figure 9-3 - Graphic showing how symmetry was used to create a 2D model of the triaxial test specimen. The standard lab specimen is 8.1 cm tall with a diameter of 3.5 cm.

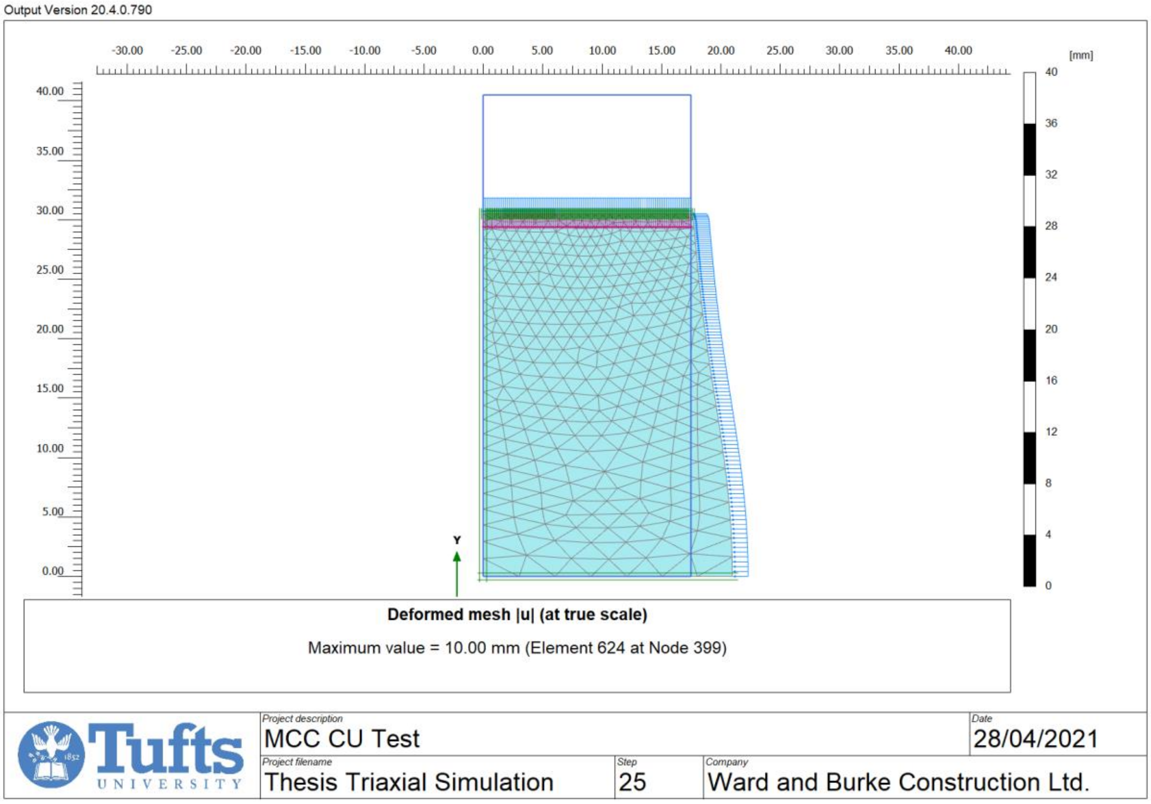

Deformed mesh |u| (at true scale)

Maximum value = 10.00 mm (Element 624 at Node 399)

Project description: MCC CU Test

Date: 28/04/2021

Project filename: Thesis Triaxial Simulation

Step: 25

Company: Ward and Burke Construction Ltd.

Figure 9-4 - Image of deformed mesh after triaxial compression simulation with a MCC soil model has been run.

B.3 Model Validation

To validate the FEA finite element models and boundary conditions selected, the results from an unconfined compression test with an elastic material were compared to an analytical elastic solution. The analytical solution assumes plane ends on the cylinder and no radial displacements at these ends. The exact solution is given in a paper by Moore (1966) and shown in Appendix C. Here solutions are presented in tabular form for cylinders in compression with no confining pressure and for the case of confining pressure with no axial compression. Superposition can then be used to evaluate stresses and displacements for any combination of principal stresses on the cylinder.

In 0 a table of stresses and displacements for $H/D = 2$ and $\nu = 0.25$ are given. Displacements are normalised by the total displacement at the cylinder ends, Δ, and stresses by the confining principal stress, σ_1. When evaluating the stresses in the model, a thin stiff layer was inserted above the specimen. This enabled a unit of stress to be applied to the top of the specimen and its large stiffness relative to the soil ensured the load was applied perpendicular to the top plane. When evaluating the displacements this was not needed as a displacement boundary condition could be applied which only permitted deformations in the y axis.

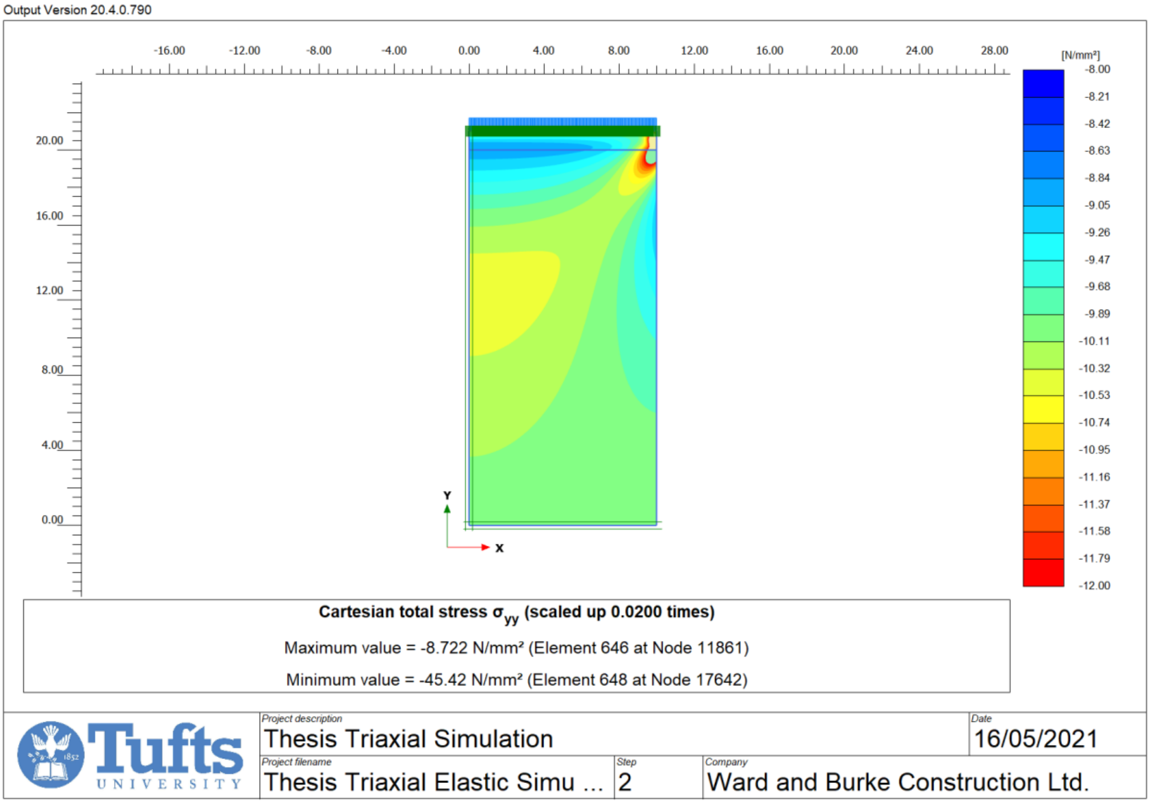

Cartesian total stress σ_{yy} (scaled up 0.0200 times)

Maximum value = -8.722 N/mm² (Element 646 at Node 11861)

Minimum value = -45.42 N/mm² (Element 648 at Node 17642)

Project description: Thesis Triaxial Simulation

Date: 16/05/2021

Project filename: Thesis Triaxial Elastic Simu ...

Step: 2

Company: Ward and Burke Construction Ltd.

Figure 9-5 - Plaxis simulation running an elastic material model in order to validate the boundary conditions. The vertical total stress is shown in this image.

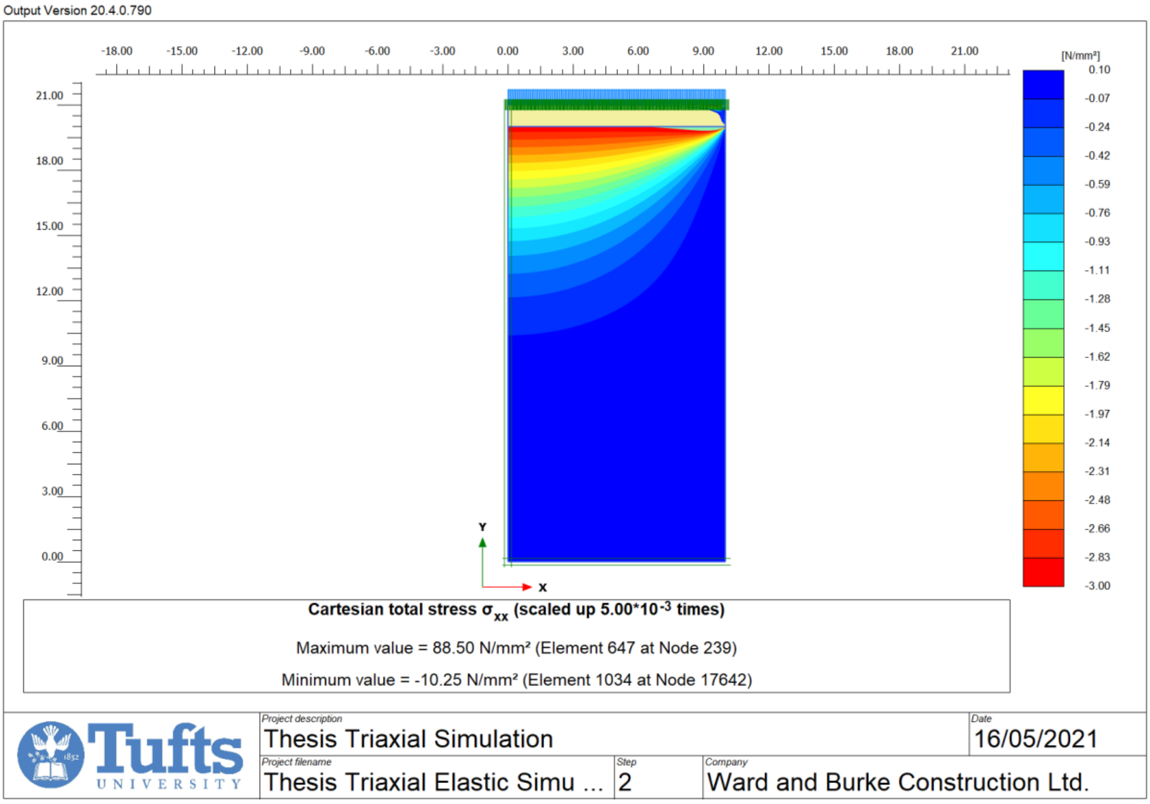

Output Version 20.4.0.790

Cartesian total stress σ_{xx} (scaled up $5.00*10^{-3}$ times)

Maximum value = 88.50 N/mm² (Element 647 at Node 239)

Minimum value = -10.25 N/mm² (Element 1034 at Node 17642)

Project description: Thesis Triaxial Simulation

Date: 16/05/2021

Project filename: Thesis Triaxial Elastic Simu ...

Step: 2

Company: Ward and Burke Construction Ltd.

Figure 9-6 - Plaxis simulation running an elastic material model in order to validate the boundary conditions. The horizontal total stress is shown in this image.

B.4 **ABAQUS Inputs**

In this section, some of the key inputs into the Abaqus FEA simulation are given.

First a part a rectangular part was created in Abaqus which would simulate the triaxial specimen. This part was then meshed using 8-node axisymmetric quadrilateral element.

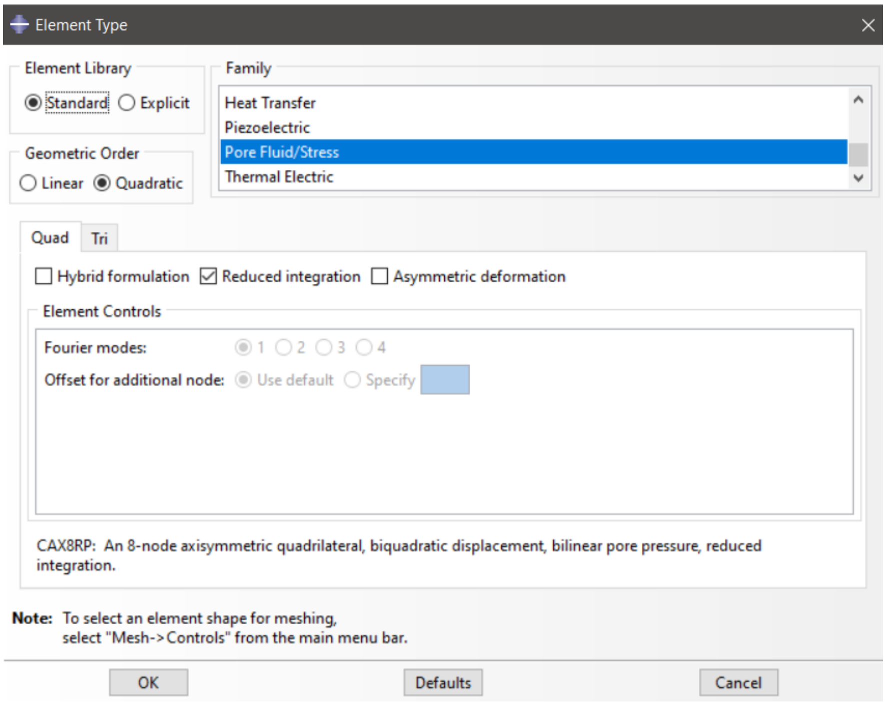

Element Library: ● Standard ○ Explicit

Geometric Order: ○ Linear ● Quadratic

☐ Hybrid formulation ☑ Reduced integration ☐ Asymmetric deformation

Fourier modes: ● 1 ○ 2 ○ 3 ○ 4

Offset for additional node: ● Use default ○ Specify

CAX8RP: An 8-node axisymmetric quadrilateral, biquadratic displacement, bilinear pore pressure, reduced integration.

Note: To select an element shape for meshing, select "Mesh->Controls" from the main menu bar.

Figure 9-7 - Element type selected within Abaqus.

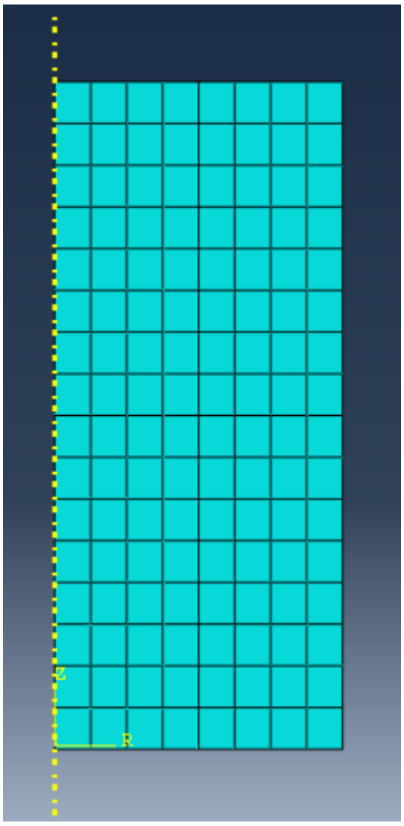

Figure 9-8 - Image of meshed part.

A symmetry boundary condition was applied was applied along the vertical axis of the model. Cell pressure was simulated with a pressure load uniformly distributed along the top and right-hand boundaries. Deviator load was then introduced through a displacement boundary condition along the top boundary.

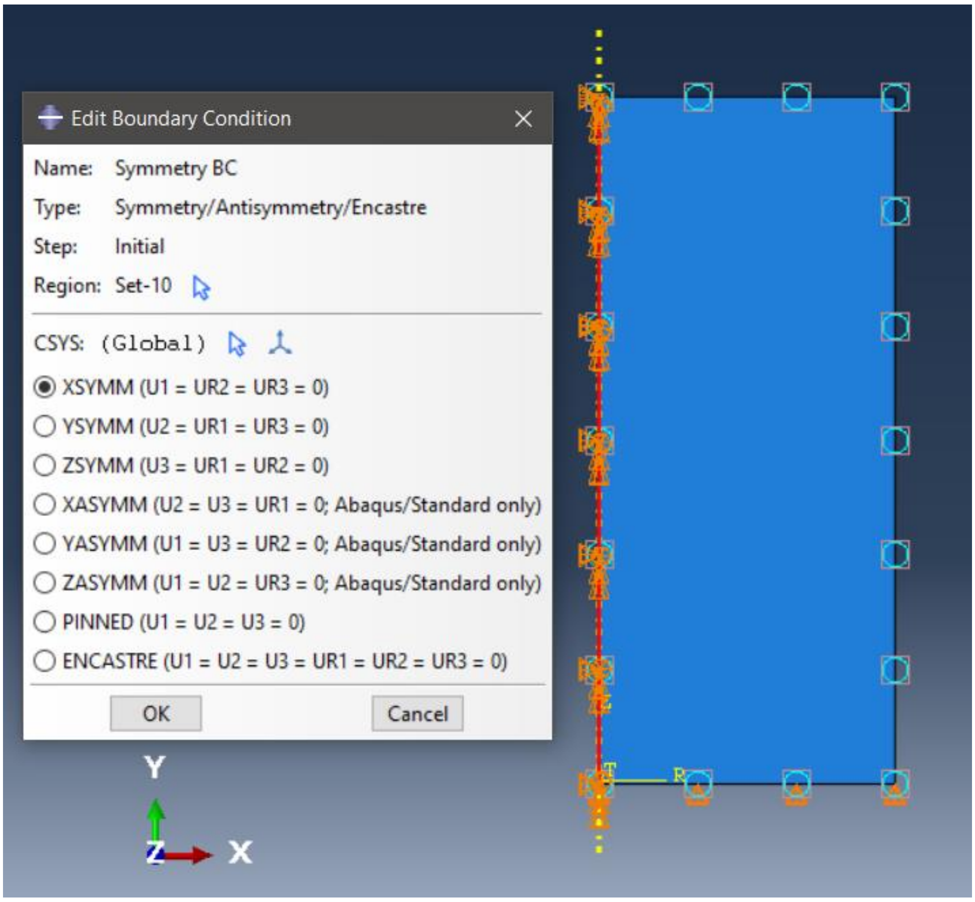

Edit Boundary Condition

Name: Symmetry BC
Type: Symmetry/Antisymmetry/Encastre
Step: Initial
Region: Set-10

CSYS: (Global)

● XSYMM (U1 = UR2 = UR3 = 0)
○ YSYMM (U2 = UR1 = UR3 = 0)
○ ZSYMM (U3 = UR1 = UR2 = 0)
○ XASYMM (U2 = U3 = UR1 = 0; Abaqus/Standard only)
○ YASYMM (U1 = U3 = UR2 = 0; Abaqus/Standard only)
○ ZASYMM (U1 = U2 = UR3 = 0; Abaqus/Standard only)
○ PINNED (U1 = U2 = U3 = 0)
○ ENCASTRE (U1 = U2 = U3 = UR1 = UR2 = UR3 = 0)

Figure 9-9 - Boundary conditions applied to part.

Two predefined fields are created within the model, the first describes the initial stress state of the specimen.

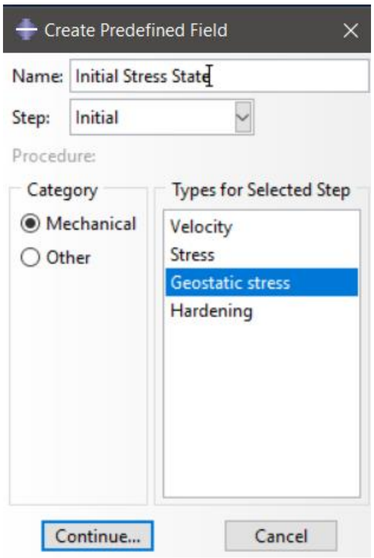

Create Predefined Field

Name: Initial Stress State

Step: Initial

Procedure:

Category

● Mechanical

○ Other

Types for Selected Step

- Velocity
- Stress
- Geostatic stress
- Hardening

Figure 9-10 Predefined field, initial stress state.

An initial geostatic stress state of 40 MPa was applied throughout the model. Initially a stress ratio of 1 was specified as an isotropically consolidated sample was considered.

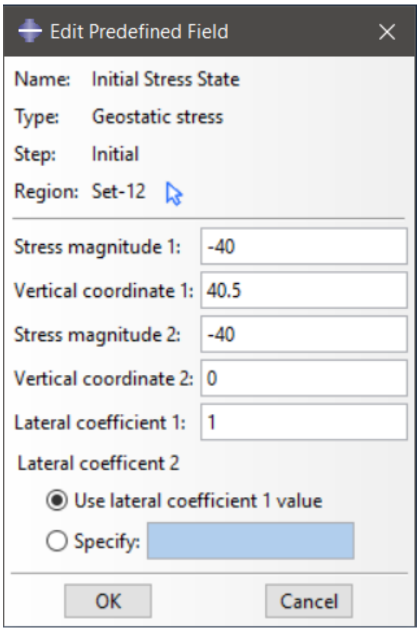

Edit Predefined Field

Name: Initial Stress State

Type: Geostatic stress

Step: Initial

Region: Set-12

Stress magnitude 1: -40

Vertical coordinate 1: 40.5

Stress magnitude 2: -40

Vertical coordinate 2: 0

Lateral coefficient 1: 1

Lateral coefficent 2

● Use lateral coefficient 1 value

○ Specify:

Figure 9-11 - Initial stress state.

The second predefined field defines an initial void ratio.

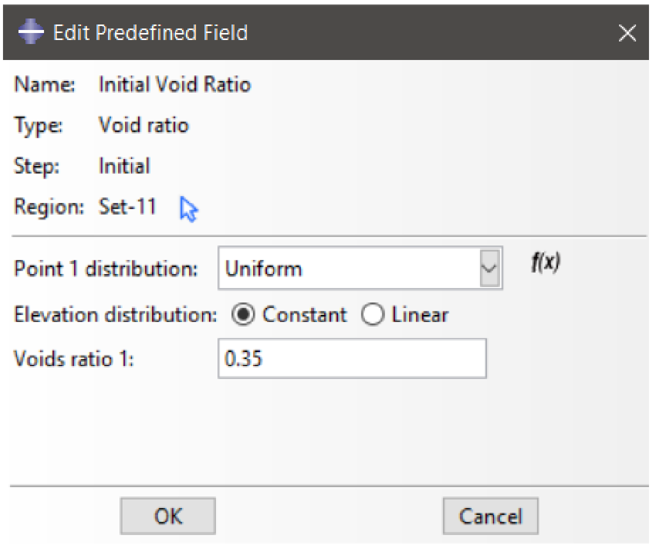

Name: Initial Void Ratio
Type: Void ratio
Step: Initial
Region: Set-11
Point 1 distribution: Uniform
Elevation distribution: ● Constant ○ Linear
Voids ratio 1: 0.35

Figure 9-12 - Predefined field, void ratio.

The top surface of the model has a permeable boundary condition applied to allow for drainage across this boundary,

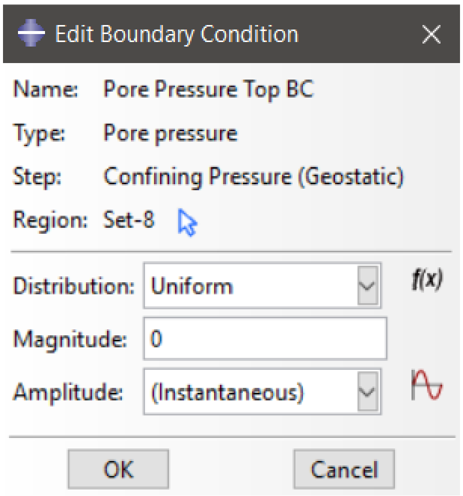

Name: Pore Pressure Top BC
Type: Pore pressure
Step: Confining Pressure (Geostatic)
Region: Set-8
Distribution: Uniform
Magnitude: 0
Amplitude: (Instantaneous)

Figure 9-13 - Pore pressure boundary condition.

In the boundary condition manager, the pore pressure boundary condition along the top of the model is deactivated for the shearing step. This ensures that undrained conditions are maintained within the model during this step.

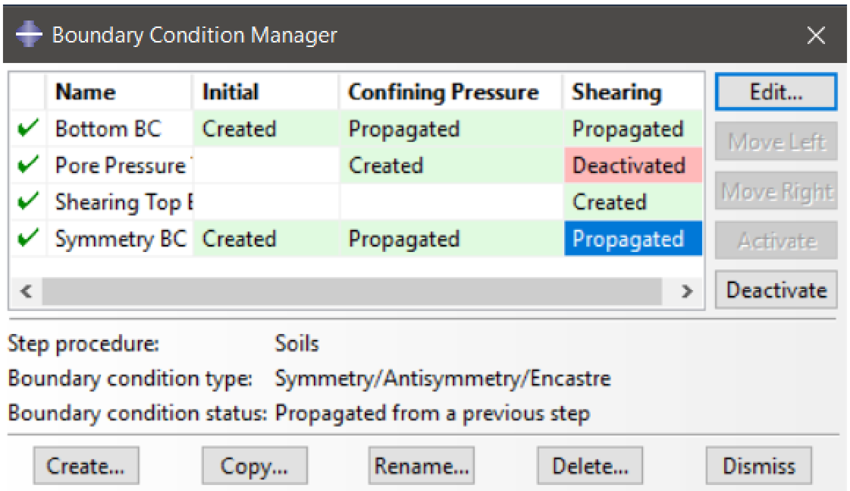

	Name	Initial	Confining Pressure	Shearing
✓	Bottom BC	Created	Propagated	Propagated
✓	Pore Pressure		Created	Deactivated
✓	Shearing Top			Created
✓	Symmetry BC	Created	Propagated	Propagated

Step procedure: Soils
Boundary condition type: Symmetry/Antisymmetry/Encastre
Boundary condition status: Propagated from a previous step

Figure 9-14 - Boundary condition manager.

The following parameters were applied to the shearing time step to ensure the solution converged.

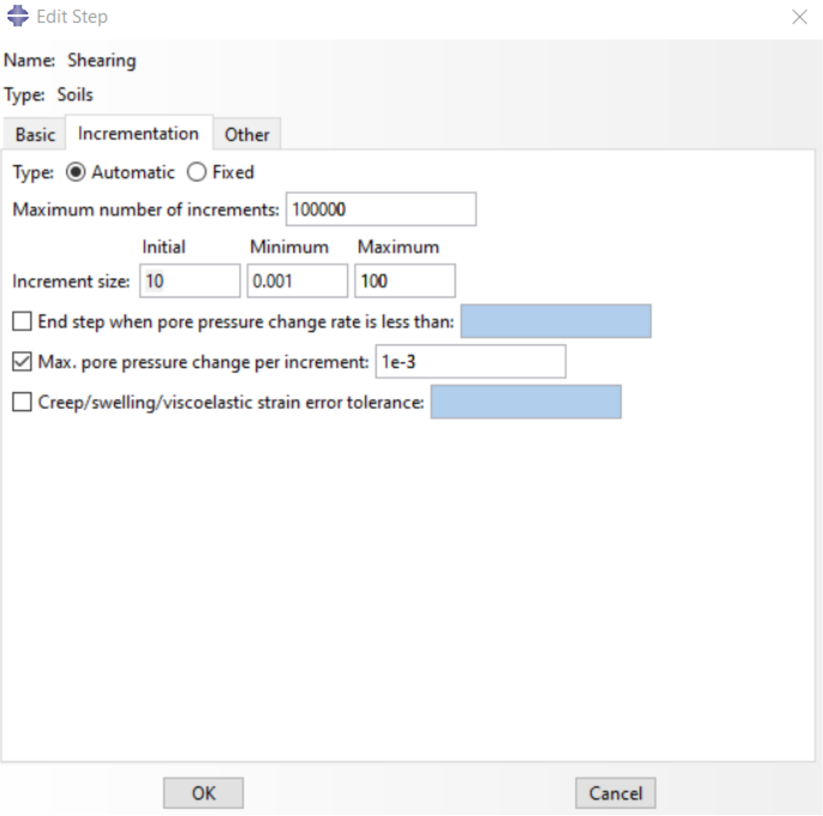

Name: Shearing
Type: Soils

Type: ● Automatic ○ Fixed
Maximum number of increments: 100000

	Initial	Minimum	Maximum
Increment size:	10	0.001	100

☐ End step when pore pressure change rate is less than:
☑ Max. pore pressure change per increment: 1e-3
☐ Creep/swelling/viscoelastic strain error tolerance:

Figure 9-15 - Shearing step parameters.

The simulation was run for 200 seconds in shearing, and non-linear geometry was activated within the model to permit large deformations to occur.

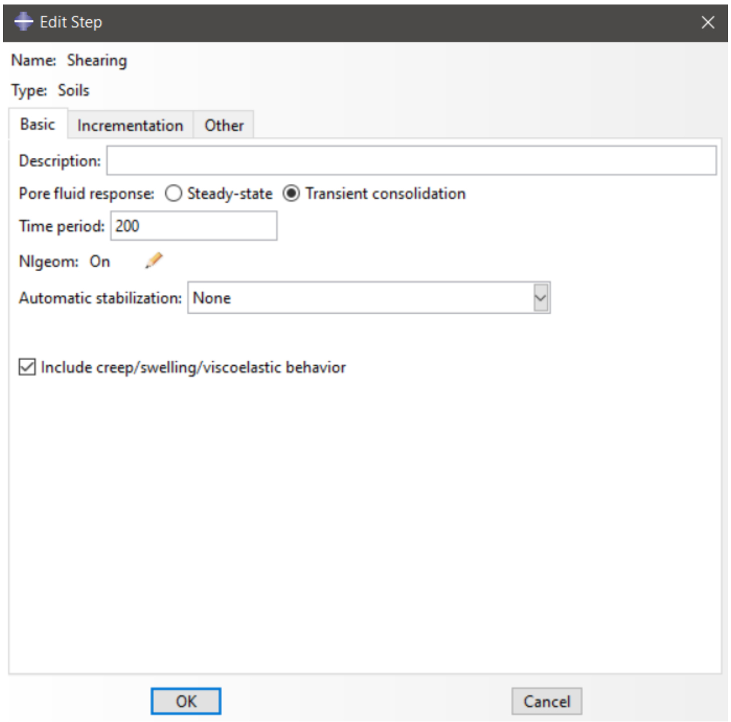

Name: Shearing
Type: Soils
Description:
Pore fluid response: ○ Steady-state ● Transient consolidation
Time period: 200
Nlgeom: On
Automatic stabilization: None
☑ Include creep/swelling/viscoelastic behavior

Figure 9-16 - Shearing step parameters.

The MCC material parameters were included in the material definition.

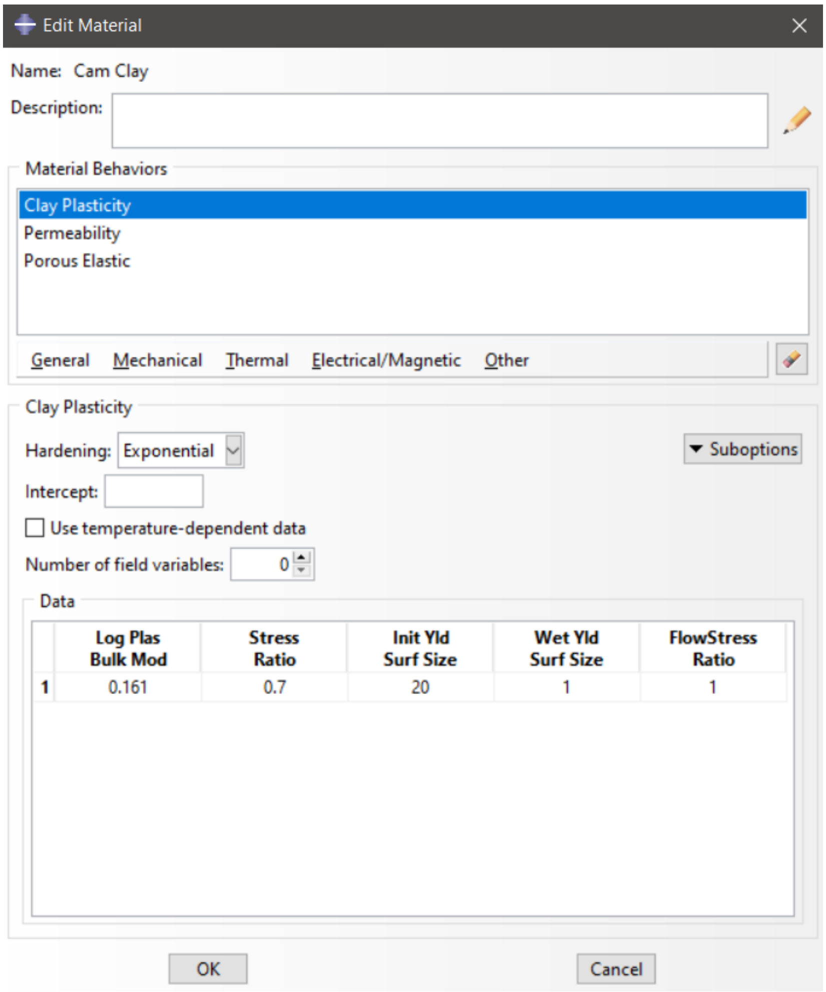

Name: Cam Clay

Description:

Material Behaviors

Clay Plasticity
Permeability
Porous Elastic

Clay Plasticity

Hardening: Exponential

Intercept:

☐ Use temperature-dependent data

Number of field variables: 0

Data

	Log Plas Bulk Mod	Stress Ratio	Init Yld Surf Size	Wet Yld Surf Size	FlowStress Ratio
1	0.161	0.7	20	1	1

Figure 9-17 - MCC parameters for RGoM-EI.

A permeability attribute was applied to the MCC material model. Abaqus only allowed for one permeability value to be entered, so a value for RGoM-EI at the end of consolidation to 40 MPa was entered.

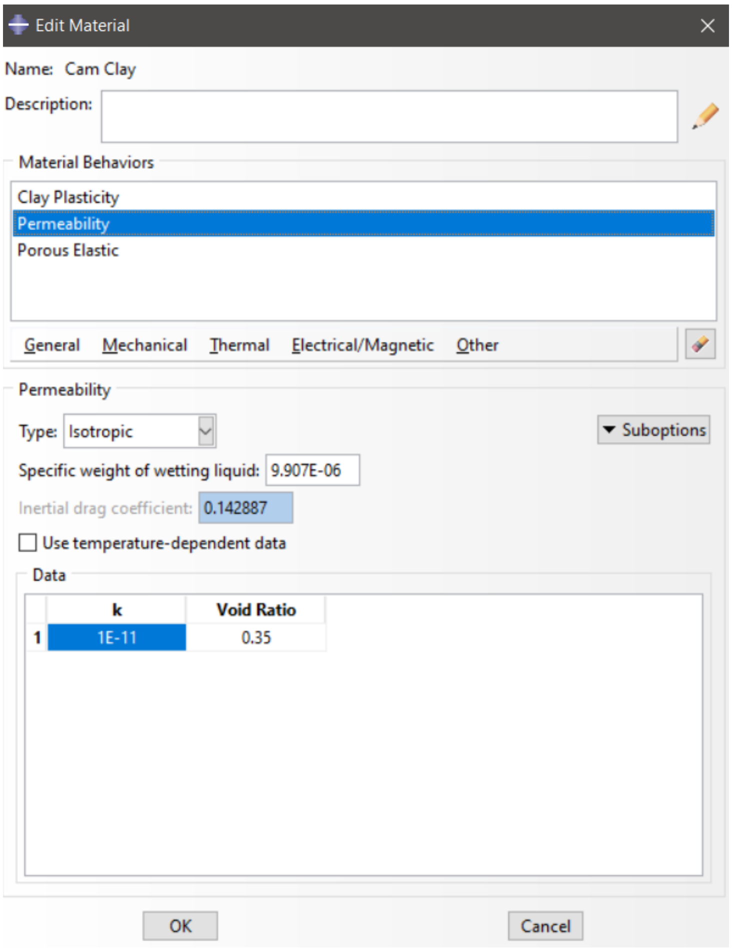

Name: Cam Clay

Description:

Material Behaviors

- Clay Plasticity
- Permeability
- Porous Elastic

Permeability

Type: Isotropic

Specific weight of wetting liquid: 9.907E-06

Inertial drag coefficient: 0.142887

☐ Use temperature-dependent data

Data

	k	Void Ratio
1	1E-11	0.35

Figure 9-18 - Permeability material attribute.

A porous elastic attribute was also applied.

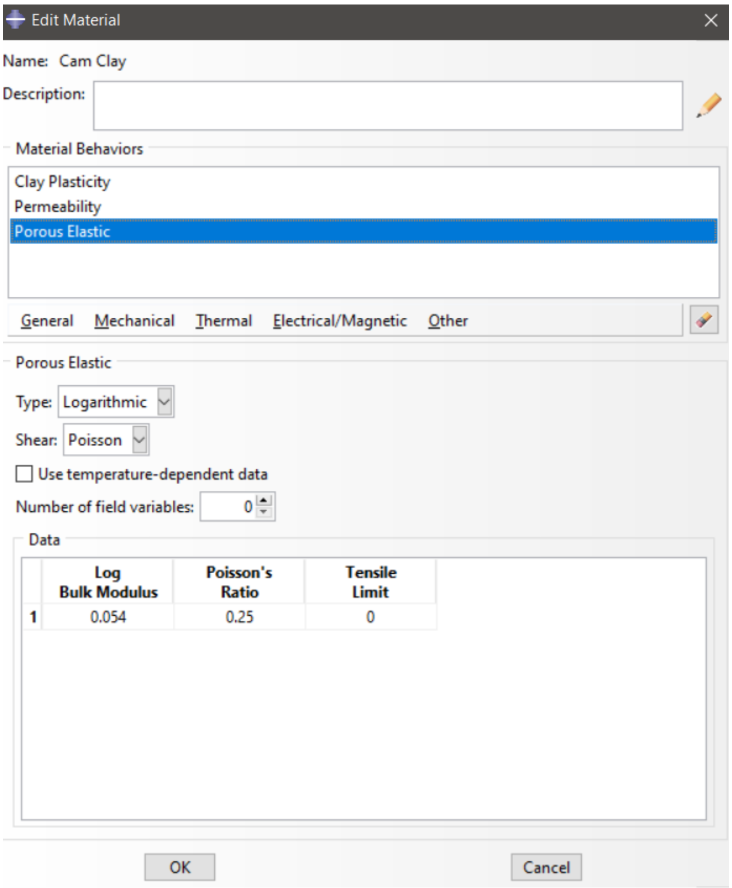

Name: Cam Clay

Description:

Material Behaviors

- Clay Plasticity
- Permeability
- Porous Elastic

Porous Elastic

Type: Logarithmic

Shear: Poisson

☐ Use temperature-dependent data

Number of field variables: 0

Data

	Log Bulk Modulus	Poisson's Ratio	Tensile Limit
1	0.054	0.25	0

Figure 9-19 - Porous elastic attribute.

Appendix C Elastic Cylinder Solution

C.1 **Introduction**

Below are tabulated solutions for the stresses and displacements inside an elastic cylinder for the case of unconfined compression. The table is taken from a paper by Moore (1966). The analytical equations describing the displacement and stress fields were solved iteratively using a finite difference method. The analytical equations must be solved numerically due to the deformation field for a cylinder with fixed ends being inhomogeneous.

C.2 **Tabulated Solution**

*Table 9-2 - Stresses and displacements for unconfined comp*ression with H/D = 2 (Moore 1966)

$2z/H$	$2r/D$					$2r/D$				
	0	0.25	0.50	0.75	1	0	0.25	0.50	0.75	1
	u/Δ					w/Δ				
1	0	0	0	0	0	-0.500	-0.500	-0.500	-0.500	-0.500
0.875	0	0.007	0,015	0.026	0.042	-0.448	-0.448	-0.447	-0.443	-0.430
0.750	0	0.012	0.025	0.035	0.056	-0.389	-0.388	-0.386	-0.381	-0.372
0.625	0	0.015	0,030	0.044	0.062	-0.325	-0.324	-0.322	-0.318	-0.313
0. 500	0	0.016	0,032	0.047	0.064	-0.260	-0.259	-0.257	-0.254	-0.252
0.375	0	0.016	0.033	0.048	0.064	-0.194	-0.194	-0.192	-0.191	-0.190
0.250	0	0.016	0.033	0.049	0.064	-0.129	-0.129	-0.128	-0.127	-0.127
0. 125	0	0.016	0.032	0.048	0.064	-0,064	-0.064	-0.064	-0.064	-0.064
0	0	0.016	0.033	0.048	0.064	0	0	0	0	0
	τ_{rz}/σ_1					σ_z/σ_1				
1	0	0.046	0.098	0.170	0.683	0.886	0.887	0.895	0.932	3.118
0.875	0	0.037	0.072	0.089	0	0.969	0.973	0.989	1.021	0.926
0.750	0	0.016	0.024	0.013	0	1.022	1.024	1.026	1.007	0.915
0.625	0	0.001	-0.002	-0.008	0	1.039	1.037	1.026	0.997	0.943
0.500	0	-0.005	-0.010	-0.011	0	1.035	1.031	1.018	0.995	0.967
0.375	0	-0.005	-0.009	-0.008	0	1.025	1.022	1.011	0.996	0.984
0.250	0	-0.004	-0.006	-0.005	0	1.016	1.014	1.007	0.999	0.993
0.125	0	-0.002	-0.003	-0.002	0	1.011	1.009	1.005	1.000	0.998
0	0	0	0	0	0	1.009	1.008	1,004	1.000	0.999
	σ_r/σ_1					σ_θ/σ_1				
1	0.295	0.296	0.298	0.311	1.039	0.295	0.296	0.298	0.311	1.039
0.875	0.179	0.172	0.147	0.082	0	0.179	0.176	0.165	0,140	0.068
0.750	0.087	0.079	0.054	0.018	0	0.087	0.083	0.070	0.045	0.010
0.625	0.033	0.028	0.016	0.005	0	0.033	0.030	0.021	0,008	-0.006
0.500	0.007	0,006	0.003	0.001	0	0.007	0.006	0.002	-0.003	-0.008
0.375	-0.002	-0.002	-0.002	0.000	0	-0.002	-0.003	-0.004	-0.006	-0.007
0.250	-0.005	-0.004	-0.003	-0.001	0	-0.005	-0.005	-0.005	-0.005	-0.004
0.125	-0.005	-0.004	-0.003	-0.001	0	-0.005	-0.005	-0.005	-0.004	-0.003
0	-0.005	-0.004	-0.002	-0,001	0	-0.005	-0.005	-0.004	-0.004	-0.003